Two-Dimensional Colloidal Nanocrystals

Michel Nasilowski, Benoit Mahler, Emmanuel Lhuillier, Sandrine Ithurria, Benoit Dubertret

2D Colloidal Nanocrystals

Michel Nasilowski[1], Benoit Mahler[2], Emmanuel Lhuillier[3], Sandrine Ithurria[1], Benoit Dubertret[1*]

[1] Laboratoire de Physique et d'Étude des Matériaux, PSL Research University, CNRS UMR 8213, Sorbonne Universités UPMC Univ Paris 06, ESPCI ParisTech, 10 rue Vauquelin, 75005 Paris, France

[2] Institut Lumière-Matière, CNRS UMR5306, Université Lyon 1, Université de Lyon, 69622 Villeurbanne CEDEX, France,

[3] Institut des Nanosciences de Paris, UPMC-UMR 7588 CNRS, 4 place Jussieu, boîte courrier 840, 75252 Paris cedex 05, France

*to whom correspondence should be sent: benoit.dubertret@espci.fr

Abstract: In this paper, we review recent progresses on colloidal growth of 2D nanocrystals. We identify four main sources of anisotropy which lead to the formation of plate- and sheet-like colloidal nanomaterials. Defect induced anisotropy is a growth method which relies on the presence of topological defects at the nanoscale to induce 2D shapes objects. Such a method is particularly important in the growth of metallic nanoobjects. Another way to induce anisotropy is based on ligand engineering. The availability of some nanocrystal facets can be tuned by selectively covering the surface with ligands of tunable thickness. Cadmium chalcogenides nanoplatelets (NPLs) strongly rely on this method which offers atomic control in the thinner direction, down to a few monolayers. 2D objects can also be obtained by post or *in situ* self-assembly of nanocrystals. This growth method differs from the previous ones in the sense that the elementary objects are not molecular precursors, and is a common method for lead chalcogenide compounds. Finally, anisotropy may simply rely on the lattice anisotropy itself as it is common for rod-like nanocrystals. Colloidally grown Transition Metal DiChalcogenides (TMDC) in particular result from such process. We also present hybrid syntheses which combine several of the previously described methods and other paths, such as cation exchange, which expand the range of available materials. Finally, we discuss in which sense 2D-objects differ from 0D nanocrystals and review some of their applications in optoelectronics, including lasing and photodetection, and biology.

Keywords: 2D, beyond graphene, nanoplates, colloidal growth, anisotropy,

TOC:

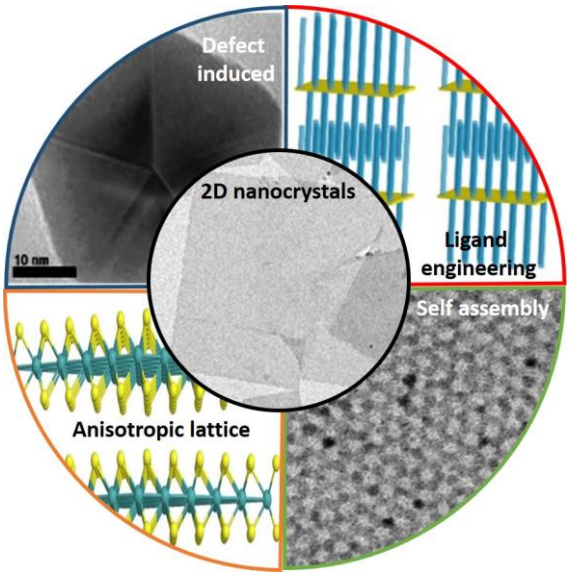

Table of contents

1. Introduction

Nanocrystals are particles with at least one dimension comprised between 1 and 100 nm. For the last decades, they have been of growing interest as they exhibit unique properties due to their small size. They are often described as artificial atoms, as their sparse density states can be modified tuning their shape, size and composition.[1] Indeed, electron confinement in those nanostructures provides the nanocrystals with properties that are much different from their bulk counterparts and can be used to enhance electric, optical or magnetic properties.[2] A typical example of the influence of size on the crystal properties are Quantum Dots (QDs) which are nanocrystals made of semiconducting materials. The band-edge energy between

the conduction and the valence band depends directly on their size, which gives their fluorescence wavelength a strong size-dependence. The shape is another parameter of key importance to control the properties of such nanoparticles as the motion of electrons (and therefore holes and plasmons) can be confined in given directions. For example, not only the catalytic activity of metals is enhanced when their size is reduced,[3,4] but the selectivity of the catalyzed reactions is also strongly dependent on the exposed facets, and therefore on the shape of the nanocrystals (NCs).[5,6] Besides, the surface plasmon resonance (SPR) in Au NCs is mostly dependent on their shape:[7] changing the geometry of the nanocrystal changes the energy of the plasmon peak more than the mere increase of the size of the spherical particles. Finally, the size, but also the shape of the nanoparticles (NPs) plays an important role in the cellular uptake.[8,9] The need to control the shape of the NPs is therefore strong and the growing interest in shape-controlled syntheses of NCs is confirmed by numerous contributions for different applications such as optics (photodetectors,[10,11] lasers,[12] fluorescence[13–15]), electronics,[16–18] catalysis,[19] biological sensing[20] and imaging.[21,22] The top-down (chemical or mechanical exfoliation[23–26] by ion intercalation, ion exchange, sonication[27] or by the "Scotch-tape" method[28]) as well as the bottom-up approaches have so far been explored to synthesize 2D nanostructures with different techniques used such as physical deposition methods (vapor deposition[29], molecular beam epitaxy (MBE)[30]), lithography,[31,32] or wet chemical methods. The latter present the advantage of being relatively cheap, easy to implement and scalable, but the precise control of the size and shape of the synthesized NPs is still challenging. However, in the last decades, numerous groups have improved the wet chemical growth techniques and have intensively studied the growth of anisotropic structures. This review will focus on the solvothermal syntheses protocols and mechanisms used to obtain colloidal metal and semiconductor nanocrystals with a two-dimensional geometry.

The synthesis of nanoparticles using wet chemical methods requires, in general, the same three components: precursors which provide the atoms for the growth of the NP (by thermal decomposition or conversion to more reactive species); ligands which ensure colloidal stability and which have a key role to precisely control the size and shape of the obtained nano-objects ; and the solvent which provides a homogeneous reaction medium in which the precursors are soluble and the final NCs are stable (it is to be noted that the solvent can also act as a source of precursors or ligands[33]). All these components, depending on their reactivity or their affinity to specific crystal facets provide good tools to control not only the size but also the shape of NCs. Before entering into the details of shape control, we will briefly remind the LaMer theory and introduce the two important steps for the bottom-up colloidal synthesis of NCs: nucleation and growth. After those steps, Ostwald ripening can occur;[34] it is generally avoided to preserve a good size monodispersity of the particles.

NCs are produced following a general synthesis scheme: precursors, which provide atoms to build the NCs, decompose or rearrange into monomers and form nuclei during the nucleation step. These nuclei can further grow to form bigger crystals either by continuous deposition of monomers on their surface, by attachment of several nuclei together or by Ostwald ripening. The nucleation-growth theory has been introduced by La Mer in the 50s, adapted from a theory developed by Becker and Döring in the 20s.[35,36]

Homogeneous nucleation occurs spontaneously and randomly, without the need for a nucleation site. It requires however a solution that is supersaturated in precursors. Heterogeneous nucleation, on the other hand, occurs at a nucleation site, which is a solid phase in contact with the liquid (or vapor) phase containing the precursors. In La Mer's theory, the so-called nucleation, which is the spontaneous formation of nuclei in the solution, is a homogeneous process, while the growth can be considered as a heterogeneous one, as precursors deposit on a nucleation site in the solution (the already formed nuclei).

The basic idea behind the theory is that a thermodynamic system tends to minimize its Gibbs free energy or increase its enthropy.[37] The Gibbs free energy of a spherical cluster can be expressed as follows:

$$\Delta G = -\frac{4}{3}\pi r^3 |\Delta G_V| + 4\pi^2 \gamma$$

Equation 1

where r is the radius, $|\Delta G_V|$ is the difference is the Gibbs free energy per unit volume, and γ is the surface energy per unit area, *i.e.* the energy needed to create a surface of unit area. The Gibbs free energy consists of two terms. The first one, negative, expresses a decrease of the Gibbs free energy, and thus a favorable event. In this case, it corresponds to the bonding of a monomer to the cluster. The second term, positive, expresses the unfavorable increase of the energy surface after the bonding of a monomer. The change in the Gibbs free energy due to the formation of a bond between a cluster and a monomer therefore corresponds to a competition between the decrease of the volume energy and the increase of the surface one. Below a certain critical size, corresponding to the critical radius $r_c = 2\gamma/|\Delta G_V|$ (calculated by canceling the derivative of *Equation 1*), the positive surface energy increase is higher, thus pushing the system towards the dissolution: the growth is unfavorable. Above r_c, the negative volume energy decrease is higher, thus growth is favored.

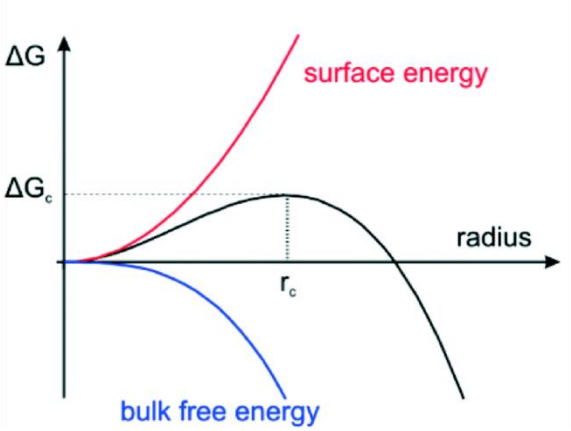

Figure 1: Evolution of the Gibbs free energy of a cluster versus its size (black curve). The evolution of the two terms in the Gibbs free energy equation is also shown; the volume (or bulk) energy (blue curve) and the surface energy (in red). The critical radius $\boldsymbol{r_c}$ *and the activation energy* $\Delta \boldsymbol{G_c}$ *are also presented on the figure. Adapted from ref.* 37 *- Published by The Royal Society of Chemistry.*

Figure 1 shows the evolution of the Gibbs free energy of a cluster. The energy barrier ΔG_c corresponds to ΔG at r_c. Once this energy barrier is overcome and the critical radius reached, stable clusters form in solution: the nuclei. These nuclei can further grow through heterogeneous nucleation.

Indeed, the surface energy necessary for nucleation is lower at phase boundaries, which become so-called nucleation sites. Therefore, once the nuclei are formed, subsequent nucleation occurs preferentially on the present nuclei. However, homogeneous nucleation is still possible, and can occur in the same time as heterogeneous nucleation. The concept of burst nucleation was introduced by Victor La Mer and relies on the separation of nucleation and growth of the nanoparticles. In order to achieve efficient separation, the idea is to produce all the nuclei at the same time, and let the growth happen only later. Figure 2 describes the evolution of the concentration of monomers versus time, showing the mechanism of the burst nucleation: in phase I, either because of a swift injection of precursors or because a critical temperature is reached, the precursors convert into monomers whose concentration increases. The supersaturation is reached at a concentration C_S, however the energy barrier to start nucleation has still to be overcome. In phase II, the saturation keeps increasing to reach a concentration C_{min} at which the activation energy is overcome: homogeneous nucleation can occur. This nucleation is very fast, hence the name “burst nucleation”. Due to the nucleation, the concentration of monomers drops, decreasing the saturation and therefore ending the nucleation step. In phase III, nucleation has stopped and the remaining monomers will only attach to the existing nuclei to grow the NPs.

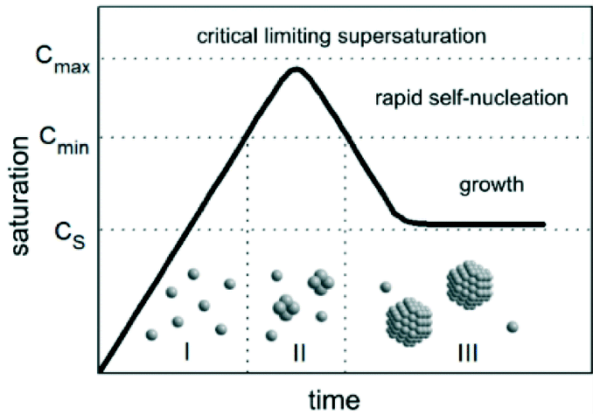

Figure 2: Evolution of the monomer concentration vs time according to La Mer's theory of burst nucleation. Adapted from ref. 37 *- Published by The Royal Society of Chemistry.*

The NP will grow in such a way to reduce its surface energy, which is the limiting parameter, already present in the nucleation step. Historically, in 1874,[38] Gibbs suggested that the shape of a crystal is dictated by the minimization of the total surface energy. Therefore, the shape of crystals (and nanocrystals, as it has been shown that the equilibrium shapes of the macroscopic crystals and nanocrystals are the same when they have the same chemical composition[39,40]) is therefore not dictated by the minimum total surface (which is a sphere), but depends strongly on crystalline facets. The final equilibrium shape will be dominated by the facets with the lowest surface energies. In 1901, Wulff[41] assumed that the surface free energy of a crystal depends on the facet's crystallographic orientation: the shape of the NP is then determined by the crystallographic nature of the expressed facets with low surface energy. In isotropic phases, this turns out to be a sphere, but for NPs which express different facets, the shape may be more complex than the mere spherical shape. An easy construction method that allows to determine the equilibrium shape of NCs has been developed by Wulff and is called the Wulff construction.[42] It requires knowing the energy needed to create a surface of unit area in the directions normal to the atomic planes (hkl) (which is the direction of the vector [hkl]) γ_{hkl}. This energy is roughly proportional to the number of broken bonds on a surface: due to smaller distances between atoms on facets with high coordination such as close-packed facets, those facets have less dangling bonds per area unit, lowering the surface energy compared to facets with more dangling bonds. When this energy is known, after choosing a set of axes, one can plot the plane normal to [hkl] at a distance $c \cdot \gamma_{hkl}$ (where c is a constant) of the origin of the axes. The same operation is repeated for all the (hkl) planes, and the geometrical shape lying inside all the plotted lines corresponds to the shape with the minimal total free energy.[40,43] Figure 3 presents an example of Wulff construction for an orthorhombic structure, with $\gamma_{100} = \gamma_{110} = 1/2\gamma_{010}$, knowing that all other (hkl) planes have much higher surface energies. The equilibrium shape in this conditions is a rod-like prism, that

is indeed found experimentally for some orthorhombic structures such as aragonite $CaCO_3$.[44,45]

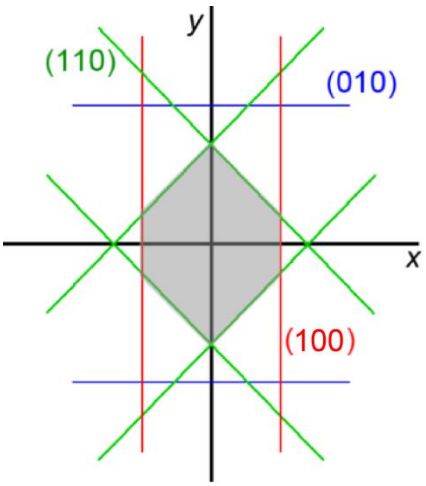

Figure 3: Example of Wulff construction for an orthorhombic structure. The equilibrium shape is shown in grey and is comprised in the lines corresponding to the low energy facets. Adapted from ref. 40 *– Belstein J. Nanotechnol.*

For a face-centered cubic (fcc) structure, the surface energies can be estimated as follows: $\gamma_{100} = 4(\varepsilon/a^2)$, $\gamma_{110} = 4.24(\varepsilon/a^2)$ and $\gamma_{111} = 3.36(\varepsilon/a^2)$ where ε is the bond strength and a is the lattice constant.[2] Thus, the surface energies can be ordered $\gamma_{111} < \gamma_{100} < \gamma_{110}$, showing that the NC should adopt a shape to favor (111) facets. However, not only the surface energy is important, the surface area also needs to be taken into account, and the NC will tend to minimize it too, resulting in truncated octahedrons enclosed by (111) and (100) facets.[46–49]

These first examples show that the equilibrium shape of a NC cannot be determined only by the minimization of the surface area as it would always yield spherical-shaped NCs. Due to symmetry reasons and to asymmetric bond strength, some materials prefer growing in one or two dimensions. Their equilibrium shape is therefore nanorods or nanoplates. Table 1 gives examples of preferred thermodynamic shapes for some chalcogenide NCs.

	M (metal)	**Thermodynamic preference (level)**	**Crystal structure**	**Reason**	**Materials**
Q (=S, Se, Te)		1-D (strong)	Trigonal	Chain-like structure	Se, Te
M_2Q	IB	1-D (medium)	Hexagonal	High surface energy in the (0001) plane	Cu_2Q

MQ	IB	0-D (strong)	Cubic	Isotropic surface energy	$Cu_{2-x}Q$
	IIB, IVA	0-D (strong)	Cubic	Isotropic surface energy	ZnQ, CdQ, PbQ
	IIB	1-D (strong)	Hexagonal	High surface energy in the (0001) plane	CdQ, ZnQ
MQ_2	IVA, VIIIB	2-D (strong)	Orthorhombic	Layered-structure	GeS, GeSe, SnS, SnSe, FeSe, FeTe
	IB, IIB, VIIIB	3-D (medium)	Cubic	Isotropic surface energy	FeS_2, CoS_2, NiS_2, CuS_2, ZnS_2
	IVB, VB, VIB	2-D (strong)	Hexagonal	Layered-structure	TiQ_2,ZrQ_2,NbQ_2, TaQ_2, MoQ_2, WQ_2
MQ_3	IVB	1-D (medium)	Monoclinic	Chain-like structure	TiS_3, ZrS_3, $ZrSe_3$, $ZrTe_3$, HfQ_3
M_2Q_3	VA	2-D (strong)	Hexagonal	Layered-structure	Bi_2Se_3, Bi_2Te_3, Sb_2Te_3
	VA	1-D (strong)	Orthorhombic	Chain-like structure	Bi_2S_3, Sb_2S_3, Sb_2Se_3

Table 1 : Thermodynamic preferences of chalcogenide nanocrystals. Reproduced from Ref. 50 *with permission from The Royal Society of Chemistry.*

There are however in the literature numerous examples of nanocrystals whose shape is not their thermodynamic equilibrium shape. For example, FeS_2 tend to grow in three dimensions, but two-dimensional FeS_2 nanoplates have been reported.[51,52] Thus, certain synthesis parameters force the NCs to grow in a non-energetically favored shape and yield two-dimensional structures. What drives this anisotropic growth?

The syntheses of NPs seldom happen in conditions close to the equilibrium. They rather deviate from these conditions and follow driving-forces that favor one shape over the other. Several mechanisms can explain the anisotropic growth of NCs.

During the nucleation of NCs, not all the nuclei are the same. Some of them might have a specific shape, others might present defects. The initial seed is therefore important in determining the final shape of the NCs as different nuclei will grow differently. Defect induced anisotropy, such as twin plane in *fcc* metals, has been widely studied and is one of the major driving force for two-dimensional growth, and can yield metal nanoprisms or nanoplates (Figure 4).[53–56] This growth mechanism will be developed in part 2.

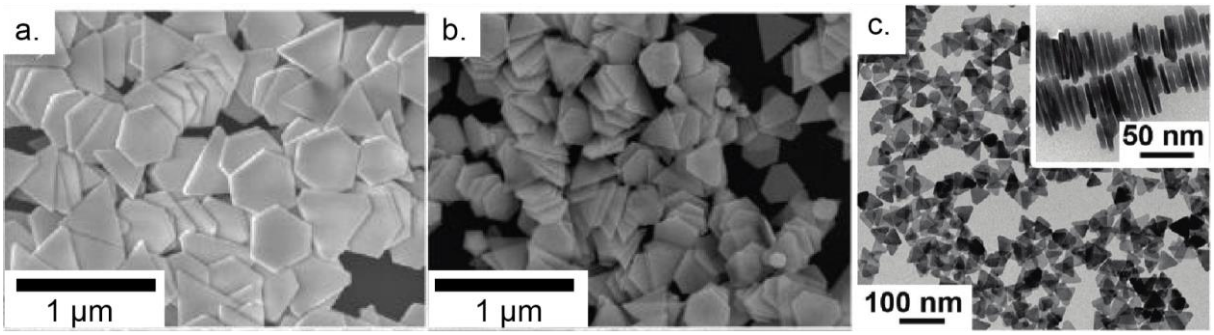

Figure 4: a. and b. Field Emission Scanning Electron Microscopy images of Au nanoplates with edge lengths of varying size. Adapted with permission from Ah et al. (2005) (ref. 57*). Copyright (2005) American Chemical Society. c. Transmission Electron Microscopy (TEM) images of Ag nanoplates, with, in the inset, stacked Ag nanoplates, standing vertically on their edges. Adapted with permission from ref* 48*. Copyright (2011) American Chemical Society.*

Because some nanoparticles have shapes that do not correspond to their thermodynamic equilibrium shapes, kinetic effects have to be taken into account. Indeed, depending on the growth rate of the nanoparticles, or on their ligands, the nanoparticles can be blocked in a local energy minimum. The nanoparticle nucleation takes place on time scales ranging from a fraction of a millisecond to a few milliseconds. The reorganization of atoms may occur on longer time ranges, not giving enough time for the structure to find the absolute energy minimum, thus being blocked in a metastable configuration that can give the NP its final shape.[58]

When the growth rate of nanoparticles is high, the fast addition of precursors does not favor any facets, exhibiting high-energy facets such as {221} facets in *fcc* metals.[59,60] On the other hand, when the growth rate is slowed down (lower temperature, slower reduction rate…), the growth is faster on high-energy planes, therefore more energetically-favored facets are expressed, such as low-indexes {111} planes in *fcc* metals (Figure 5).[60]

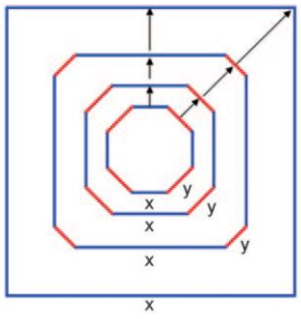

Figure 5: Shape evolution of a nanoparticle during growth. Rapid addition to high-energy facets y (relative to x-edges) results in the elongation of the x, low-energy edges. From ref. 2. Copyright 2009 by John Wiley & Sons, Inc. Reprinted by permission of John Wiley & Sons, Inc.

This growth sequence can be dramatically changed because of the influence of ligands. Indeed, they can cap specific facets, slowing the growth of the passivated facets compared to the other ones. Because the growth in some crystallographic directions is hindered, rod- or plate-like symmetries can be obtained. This effect is called chemical poisoning.

Many factors influence the chemical poisoning effect. First, because the passivation of some facets is the primary driving force for anisotropic growth, the ligands will play a crucial role in determining which facets will grow. Their affinity to the atomic species at the surface of the nanoparticle will help a better or worse passivation. For CdSe nanoparticles, for example, a strong ligand such as trioctylphosphine (TOP), or trioctylphosphine oxide (TOPO), shows such strong affinity to surface cadmium ions that it reduces the energy difference between the different facets, annihilating the chemical poisoning effect: the growth rate of all the facets becomes very similar, leading to isotropic, spherical CdSe NPs.[61] The nature of the ligand is of course very important: it can be inorganic[62] or organic,[61,63,64] and a small change in its nature can yield totally different results.[65] Controlling the chemical poisoning induced by ligands can lead to different shapes using the same material and crystal structure. For example, wurtzite CdS or CdSe/CdS nanocrystals can be synthetized with rod[66], tetrapod[67] or plate like shapes[68,69] depending on the synthesis conditions and the use of phosphonic acid ligands which hinder the nanocrystals growth perpendicular to the wurtzite c axis, leading to the formation of rod-shaped nanocrystals.Another important characteristic of ligands is their propensity to form close-packed layers: it is called the soft-templating effect, developed in part 3. While electrostatic forces bind the ligands to the surface of the NPs (eg. negatively charged acids with positively charged ions), the organic chains of the ligands, which ensure the colloidal stability, can form a stable assembly that decrease the energy of the facets and therefore hinder the growth in this direction, yielding nanoplatelets (see Figure 6), or increase the steric repulsion between NPs through their bulky and rigid chains, decreasing the probability of random attachment between several NPs (see part on Oriented Attachment).[63,64,70,71]

Another important factor in the ligand-mediated shape control is the temperature of the growth reaction. Not only can the temperature play a role in the kinetic control of the NP growth by lowering the differences in the energies of the facets, but it also acts on the formation of the ligand assemblies. Indeed, low temperature growth will enhance the subtle energy differences between the facets, and subsequently the corresponding growth speeds differences. Besides, the close-packed layers of surfactants can form under a certain temperature, above which they decompose and cannot play their role as a soft template anymore.[64,72,73]

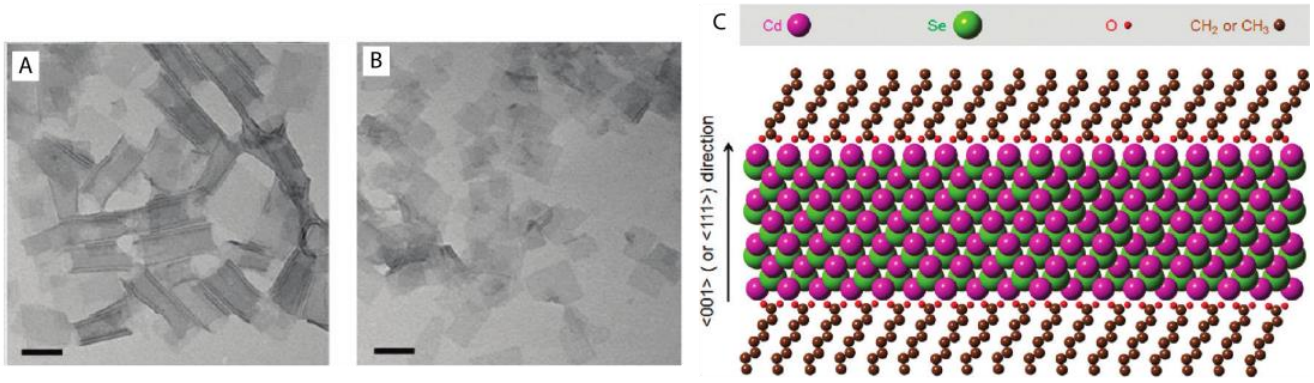

Figure 6: A and B. 2D CdSe nanoparticles of different lateral size. C. Scheme of the CdSe two-dimensional nanoparticle. The ligands are fatty acids that attach with their negatively charged acid function to the positively charged Cd ions at the surface of the NP. Their organic backbone form a fatty-acid layer that acts as a soft template hindering the growth in the direction of the passivated planes. Scale bar is 50 nm. Adapted with permission from ref. 64*. Copyright (2011) American Chemical Society.*

Once the nuclei are present in solution, they can grow through the addition of precursors or self-assemble in solution to form new, larger crystals. This mechanism is developed in part 4. In 1998, R. L. Penn and J. F. Banfield described on TiO_2 a mechanism for the anisotropic growth of NCs: oriented attachment (OA). In this mechanism, two adjacent NPs reorganize so that they share a common crystallographic orientation. The decrease of the surface energy (through the decrease of the number of unsatisfied surface bonds) is the driving force for the attachment of these NPs, to form a new crystal.[74] This mechanism requires the NPs to be free to move, as in solution, which explains while this mechanism is found to occur in wet chemical syntheses. However, oriented attachment can also occur between NPs of different crystalline structure, the only condition is for the two "daughter" NCs to have facets with similar sizes. During the OA mechanism, several steps are involved, presented in Figure 7. First, the NCs need to diffuse and be in close vicinity to each other. Then, because the diffusion can be assimilated to a random walk process driven by Brownian motion, the orientation of the NCs is not necessarily coherent and OA cannot happen. Thus, the rotation of the NPs is needed for the NC to align with its neighbor and decrease the grain-grain boundary energy. Finally, the desorption of ligands at the interface and the attachment of NCs yield a new crystal. Kinetic studies seem to show that the limiting step is the diffusion of NCs.[75] Figure 8 shows *in situ* transmission electron microscopy images of the OA mechanism for iron oxide nanoparticles. The attachment of NCs does not always occur with the exact same crystalline orientation: two NCs can attach with slightly different orientations, but that still decrease the overall energy. Such misorientations can lead to the incorporation of defects (such as twin defects, Figure 9) in the new crystal. This allows to combine different mechanisms for anisotropic growth.[74,76]

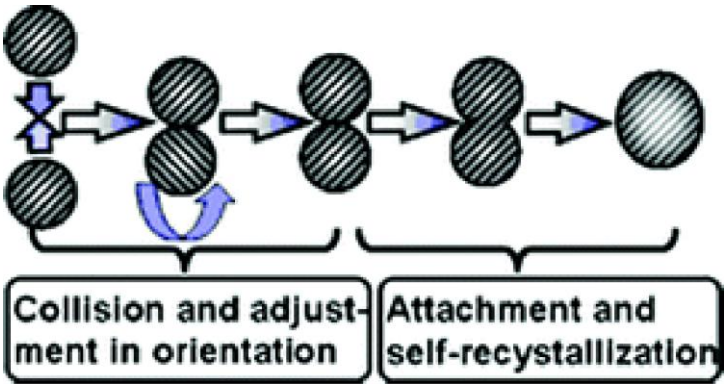

Figure 7: Scheme of oriented attachment mechanism. After the diffusion of NCs, the rotation of NCs is necessary for proper crystallographic orientation, and then attachment and self-recrystallization occur. Reproduced from Ref.77 with permission from The Royal Society of Chemistry.

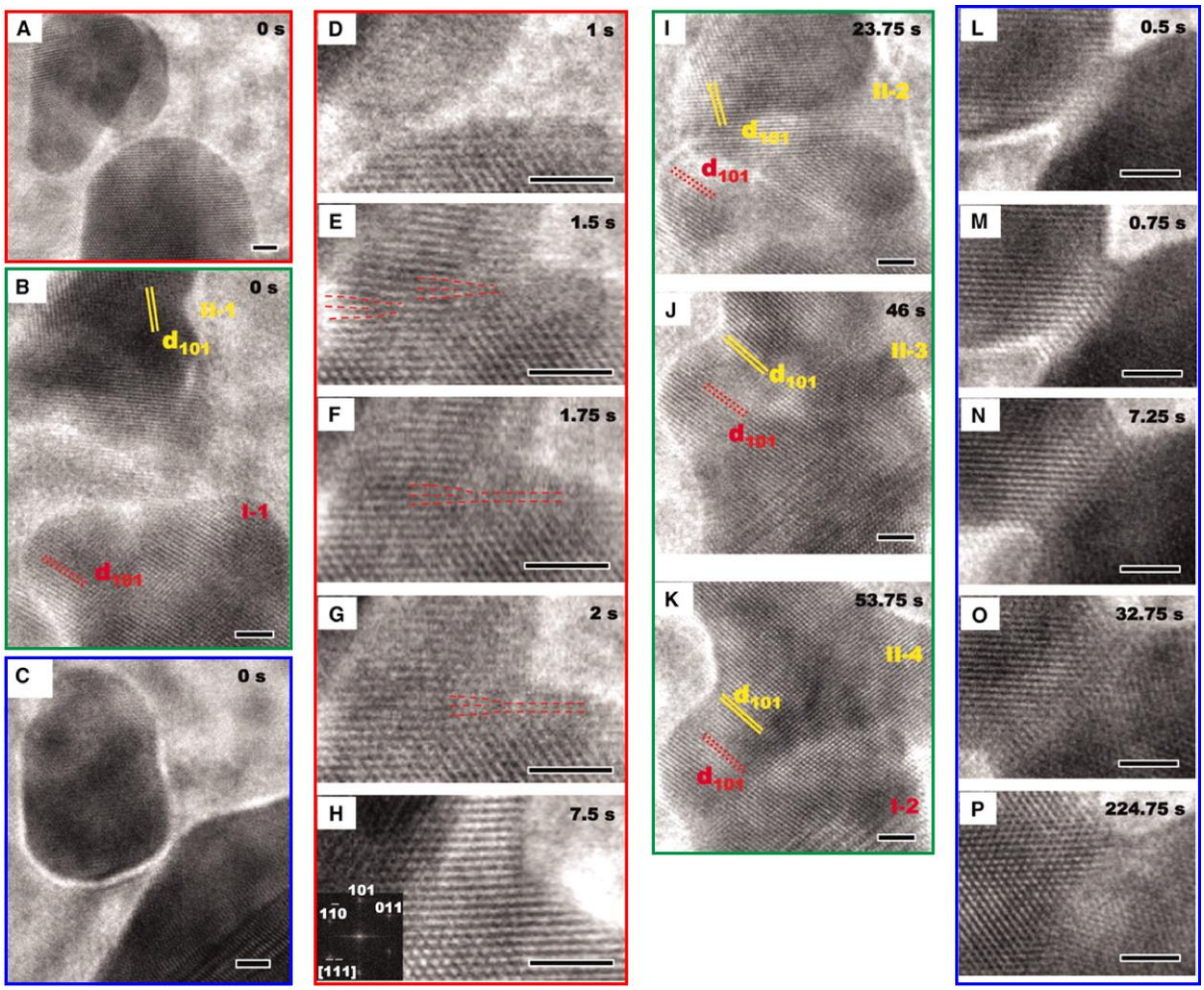

Figure 8: Sequence of in situ TEM images showing the details of the oriented attachment method for iron oxide nanoparticles. (A) and (D to H) Sequence showing attachment at a lattice-matched interface. (A) shows the arrangement of particles before attachment. The asymmetric particle in front of the smaller spherical particle is not involved in the attachment process. (D) to (G) show formation of the interface. Two edge dislocations denoted in (E) to (G) by red dashed lines translate to the right, leaving a defect-free structure in (H). (B) and (I to K)

*Sequence of images showing relative rotations of particles during the attachment process, leading to a lattice-matched interface. (C) and (L to P) Sequence showing how the interface expands laterally after attachment. All scale bars are 2 nm. From ref.*78*. Reprinted with permission from AAAS.*

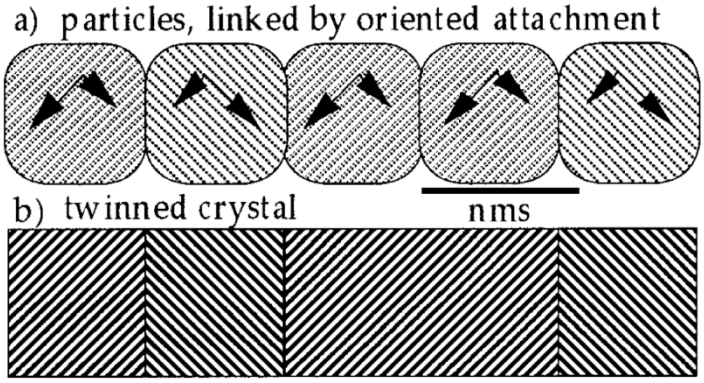

*Figure 9: Schemes of NCs during and after oriented attachment. a) primary particles during the oriented attachment mechanism that yields b) a new crystal that contains twin defects. Adapted with permission from ref.*76*. Copyright (1998) Mineralogical Society Of America.*

Another class of material consists of naturally layered materials such as graphene or transition metal dichalcogenide structures. Here, the atoms are convalently bond to each other within one layer. The layers, however, are maintained together through weak van der Waals interactions only (Figure 10). In this case, the shape is directly governed by the Wulff construction, the challenge is thus to control the thickness of the nanosheets down to the monolayer. These materials and their colloidal syntheses are developed in part 5.

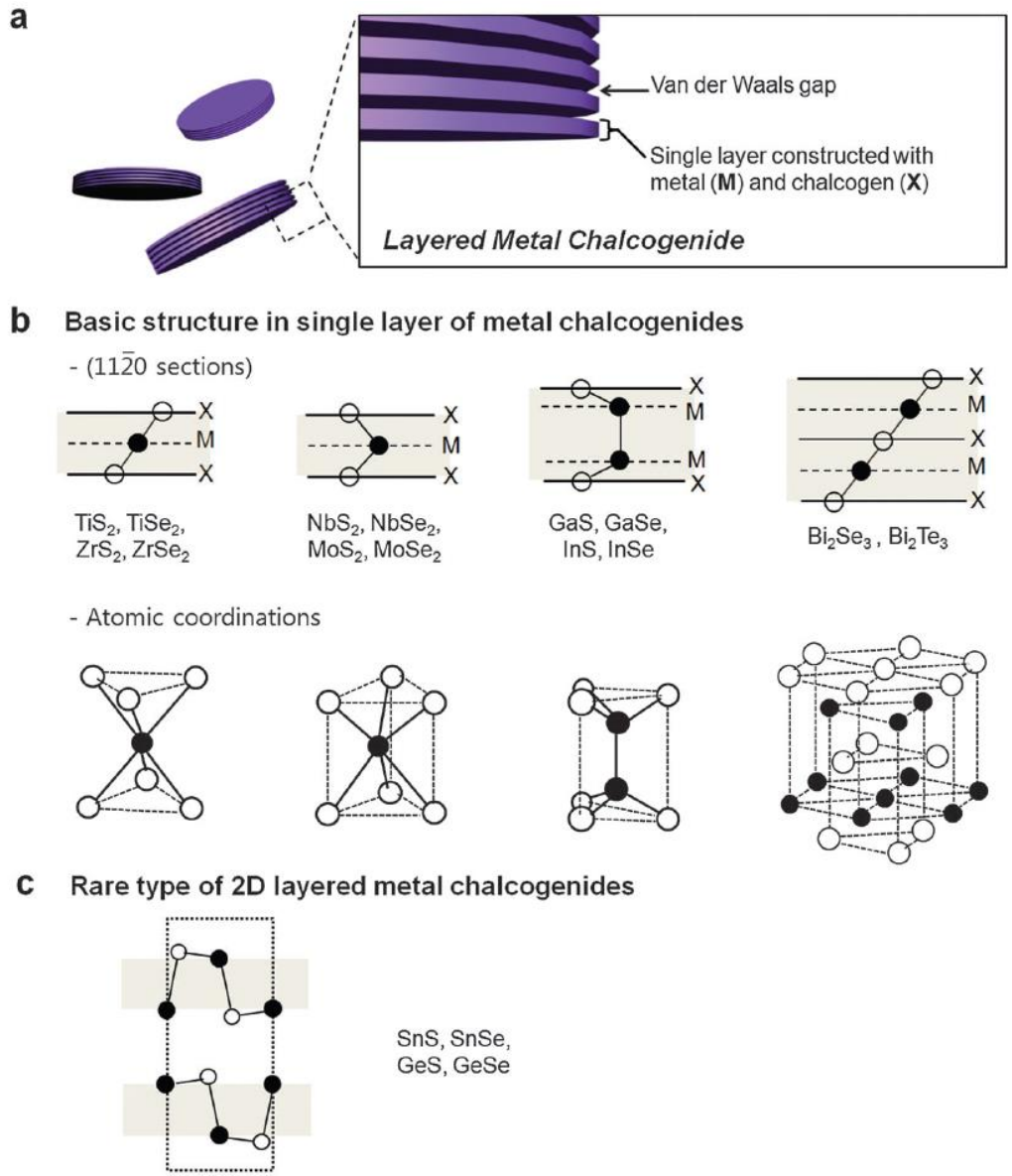

Figure 10: Layered structures of metal chalcogenides. (a) Single nanocrystal is composed of multiple layers stacked along the c-axis by weak van der Waals force. Reproduced from Ref. [79] *with permission from The Royal Society of Chemistry. (b) Single layer of metal chalcogenides exits as various polymorphs. Each layer may have tri-, tetra- or penta-atomic layers of metal and chalcogen. Reproduced from ref.* 80 *with permission of Taylor and Francis. (c) Rare GeS type of 2D layered metal chalcogenides. Reproduced from p.91 from ref.* 81 *with permission of Springer.*

2. Defect induced anisotropy

2.1. Symmetry breaking during nucleation

Since bulk silver and gold have an *fcc* structure, the formation of anisotropic shapes is thermodynamically not favored. However, several works have reported anisotropic Au or Ag nanoplates or nanoprisms.[55,82] Therefore, symmetry breaking needs to occur during the

formation of metallic nanoparticles. Given the nucleation-growth mechanism, the size, shape and crystalline structure of the initial nuclei play an important role in determining the shape of the final NC. Indeed, if the synthesis is performed under thermodynamic control only, the nuclei formed will obey the same rule and tend to minimize their surface free energy. However, if, right after nucleation, they deviate from the thermodynamic equilibrium shape, it means there is a driving force that stabilizes other shapes. One of the reasons for such a deviation is that the synthesis enters kinetic control, instead of thermodynamic control. Indeed, in practice, the synthesis is performed far from the equilibrium conditions, as several parameters such as a large surface-to-volume ratio, a high proportion of atoms at the edge or low difference in energy between different structures, strongly influence the formation of nuclei in solution.[83,84] These factors lead to the formation of defects and to polycrystalline nuclei then to symmetry breaking that will start the anisotropic growth.

2.2. Twin defects

The most common kinds of defects in face-centered cubic (*fcc*) structures are twin defects and stacking faults.[49] Twin defects are of particular interest in the shape control of NCs. In *fcc* structures, the atomic planes are organized in three different manners, and stacked according to the "abcabcabc"… sequence. If, after an "a" plane, the atoms deposit as if they were on a "c" plane (instead of "b"), and then follow the regular stacking, their sequence will be the following: "abc**a**cbacb". The highlighted "a" plane is a mirror plane, or twin plane (Figure 11). The reason that such defects are very common in *fcc* structures in the (111) direction is that the energy difference between the perfect crystal and the twinned one is very low (the coordination number of atoms in each layer is the same for the perfect crystal and for the twinned one).[49,59] The local symmetry around the twin defect is hexagonal close-packed (*hcp*); for example, between the *fcc* and *hcp* arrangement of atoms in copper along the (111) direction, the difference in binding energy is only 0.01 eV per atom. Adatoms that attach to a surface can therefore easily switch from and *fcc* to an *hcp* structure, forming a twin plane.[85,86] As twin defects are good ways for the crystals to release surface stress, multiply twinned particles can also be formed.

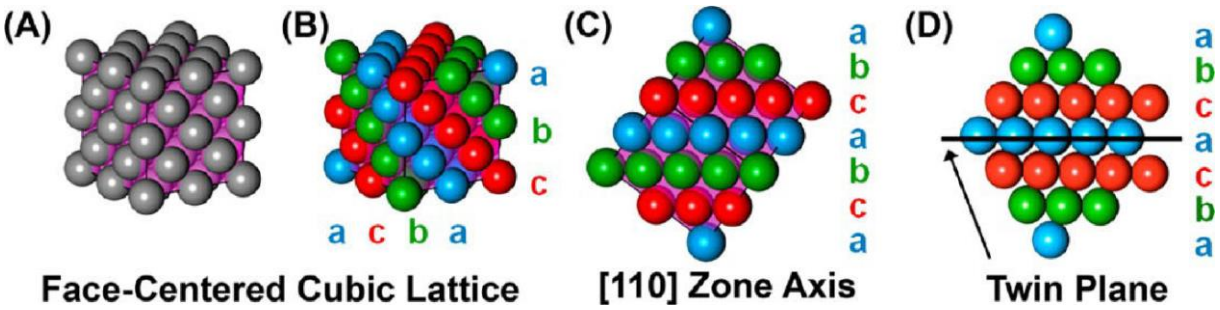

*Figure 11: Model of a twin plane in a face-centered cubic (fcc) metal: (A) fcc lattice; (B) fcc lattice with the repeating « abcabcabc » stacking pattern annotated; (C) annotated fcc lattice from (B) oriented to the [110] zone axis so that the {111} repeating layers are more easily visible; (D) annotated fcc lattice which contains a twin plane, as viewed down the [110] zone axis. Here, the insertion of a « c » layer in place of a « b » layer (« abcacba ») in the repeating pattern has resulted in a structure which is mirrored around the central « a » layer (marked with a horizontal line). Reprinted with permission from ref.*59*. Copyright (2013) American Chemical Society.*

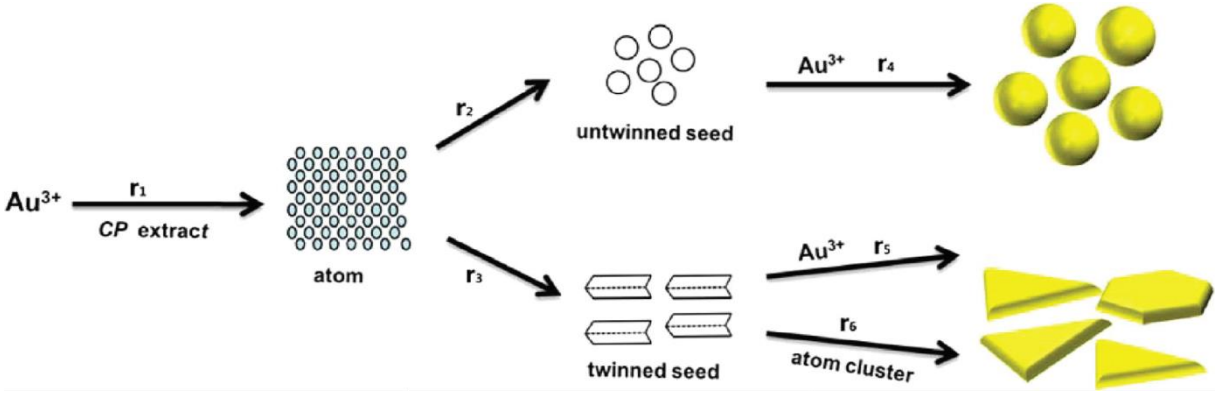

*Figure 12: Schematic diagram of the formation of Au nanoplates. r_1 corresponds to the reduction rate of Au^{3+} that dictates the period of nucleation and the amount of Au^{3+} in the subsequent growth stage. r_2 is the rate of spherical nucleation, leading to spherical nanoparticles (with growth rate r_4). r_3 is the rate of twinned-particle nucleation, followed by rapid deposition of Au atoms on the sides of the nanoparticule, leading to nanoplates (with growth rate r_5). Attachment of atom cluster is also possible via rate r_6 (discussed below). Reprinted with permission from ref.*87*. Copyright (2012) American Chemical Society.*

2.3. Anisotropic growth due to twin defects

2.3.1. Singly-twinned nanoparticles

When a single twin plane is formed, the resulting nucleus, at the early stage of growth, is a hexagonal plate due to the six-fold symmetry of *fcc* structures (Figure 13). Each side of the hexagon is either a concave side or a convex side because of the presence of a twin plane. When atoms diffuse towards the nucleus and adsorb to grow the NC, they can either adsorb on a concave or on a convex face. On the convex side, each atomic site has only three closest neighbors, and the stabilization energy is therefore quite low. On the other hand, on the concave side, newly adsorbed atoms are stabilized by four neighbors from several facets,

increasing the stabilization energy. Atoms will then preferentially adsorb on the concave sides, favoring the growth of the NC along these sides rather than the convex sides. This can be seen on Figure 13 where a singly-twinned nucleus is represented. The growth will be favored on the facets that present a concave-type surface while the convex-type surface does not favor adsorption of new atoms, and will remain unchanged. This can also be explained by the Gibbs-Thomson formula which states that the chemical potential is inversely proportional to the curvature:

$$\Delta\mu = \gamma\Omega(1/R_1 + 1/R_2)$$

where $\Delta\mu$ is the change in the chemical potential, γ the interfacial free energy, Ω the atomic volume and R_1 and R_2 are the radii curvature.[2] For a convex surface where the curvature is positive, the chemical potential change is positive, and the adsorption of atoms is favored on a flat surface rather that a convex surface. On the other hand, for a concave surface where the curvature is negative, the change in the chemical is negative, and the adsorption of atoms on the concave side is favored.

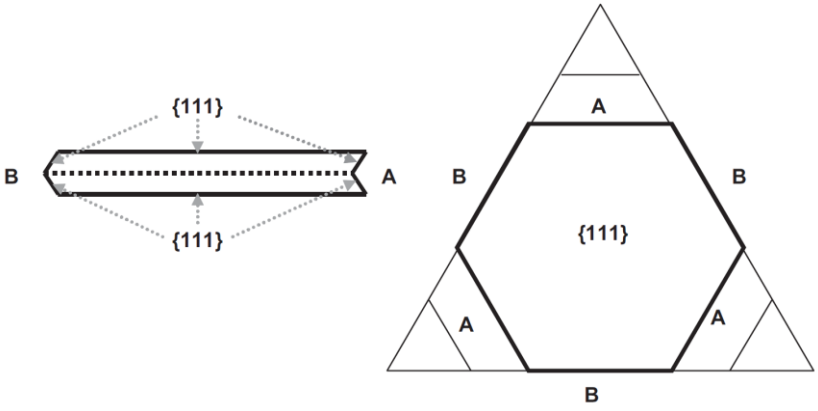

*Figure 13: Growth model for a singly-twinned nanoparticle. The A-type concave facets grow more rapidly than B-type convex facets, yielding triangular prisms with exposed B-type facets. From ref.*88*. Copyright 2005 by John Wiley & Sons, Inc. Reprinted by permission of John Wiley & Sons, Inc.*

2.3.2. Multiply-twinned nanoparticles

In the case of multiply-twinned nuclei, several cases can be observed. First, if a second twin plane is parallel to the first one, all the side of the nucleus will exhibit a concave and a convex structure, equalizing the stabilization energy for adatoms, leading to a homogenous growth along the six directions (Figure 14). The out-of-plane growth is however still not favored as atoms prefer to adsorb on concave surfaces rather than flat surfaces. One can further imagine the effect of extra twin planes parallel to the first one: triply-twinned nanoparticles will grow in the six directions, but with different growth rates as some sides

exhibit only one concave-type surface while the others exhibit two. Those nanoparticles will yield non-equilateral hexagons as shown in Figure 15.

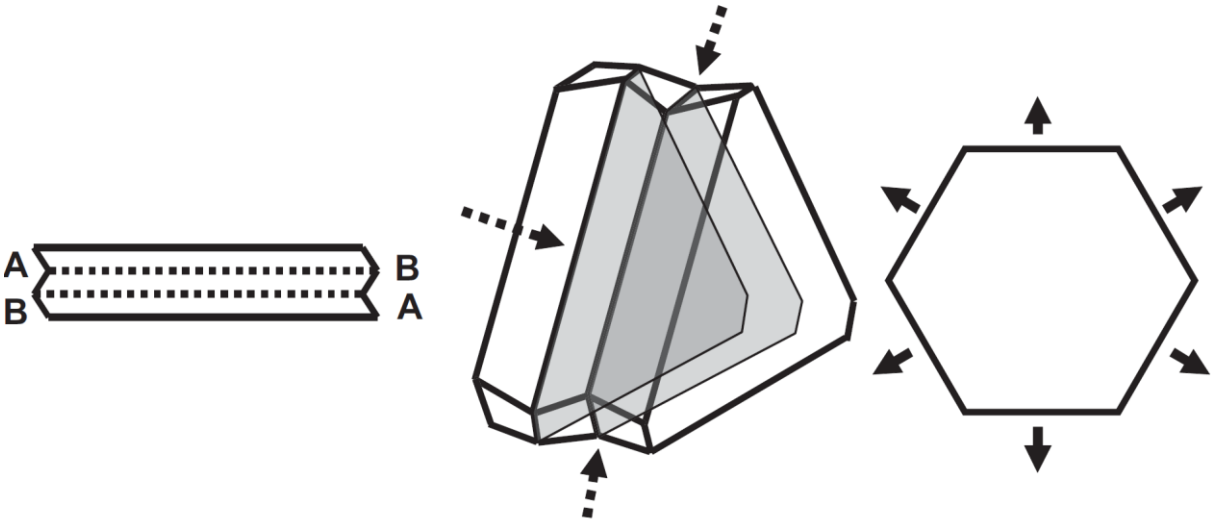

*Figure 14: Growth model for a doubly-twinned nanoparticle. All six sides now exhibit A-type concave facets (dashed arrows) which causes rapid growth in all the six dimensions (solid arrows). From ref.*88*. Copyright 2005 by John Wiley & Sons, Inc. Reprinted by permission of John Wiley & Sons, Inc.*

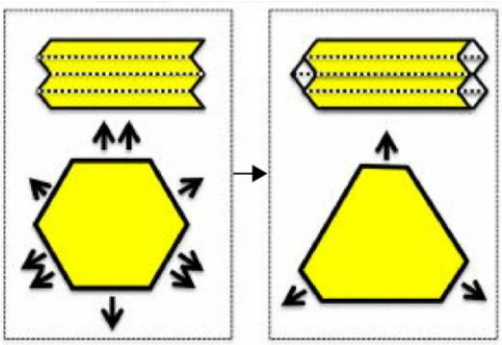

*Figure 15: Growth model for triply-twinned nanoparticles yielding non-equilateral hexagons. Reprinted with permission from ref.*89*. Copyright (2011), American Institute of Physics.*

Second, because twin planes can also form in directions that are not parallel to each other, different morphologies can be obtained. Indeed, in fcc metals for example, {111} twin planes can form at an angle of 70.53°, while $2\pi/5 = 72°$. This explains why the five-fold symmetry is often present in fcc structures. Thus, icosahedra and decahedra are often formed.[90] The remaining gap of 7.35° between two {111} facets is filled by the stretching of the bonds between atoms, which leave their low energy configuration but allow a more energy-favored arrangement of atoms at the surface (Figure 16).[91] This stretching, however, is favored for small size of NPs. Calculations show that multiply-twinned Ag seeds are the more energetically favored.[92] An increase in the size of the NP increases the stretching of the bonds, decreasing the stability of the structure that was stuck in a local minimum of energy.[91] The

stability of the structure therefore depends on their size[90,92] but also on a complex interplay between the minimization of the surface energy (shape) and the minimization of the bulk energy (local atomic orientation).[93] At small sizes, icosahedra are favored, and as the NP grows, decahedra become predominant at medium sizes, and finally thermodynamically favored Wulff polyhedra at large sizes.[2] Simulations performed in 2002 show that for Ag nanoparticles of small sizes (below 170 atoms), the icosahedral shape is dominant, then the icosahedral shape becomes predominant, and above 600 atoms, fcc structures compete with decahedra (Figure 17).[94]

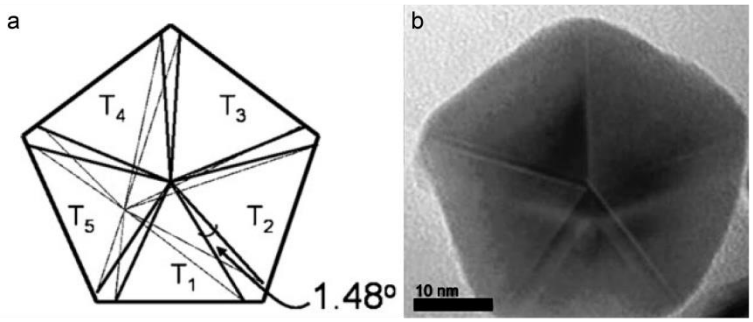

*Figure 16: a. Sketch of penta-twinned decahedral nanoparticle. The tetrahedra that make the decahedron share a common axis, and present an angle of 70.52° between two {111} facets, leaving a theoretical gap of 1.48° between two tetrahedral. From ref.*85*. Copyright 2010 by John Wiley & Sons, Inc. Reprinted by permission of John Wiley & Sons, Inc. b. TEM image of a gold decahedron nanoparticle. Reprinted with permission from ref.*95*. Copyright (2008) American Chemical Society.*

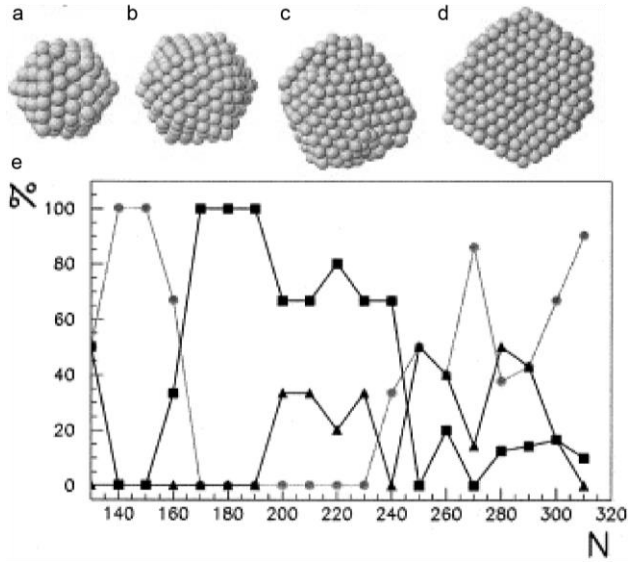

Figure 17: Dependence of shape with size of Ag clusters. a, b, c and d: typical structures obtained for Ag clusters. a. Icosahedron at 147 atoms, b. icosahedron at 309 atoms, c. decahedron at 561 atoms and d. fcc polyhedron at 923 atoms. e. Percentage of different shapes obtained for increasing number of atoms N in the cluster. Circles are icosahedra,

*squares are decahedra and triangles are fcc structures. Reprinted from ref.*94*, Copyright (2002), with permission from Elsevier.*

2.4. Inducement of twin defects and oxidative etching

The mere role of ligand templating cannot explain the anisotropic growth of NPs. The nature and shape of the initial seeds definitely play an important role, as seen previously. An interesting aspect is the selection of the initial seeds: why are the anisotropic seeds, less thermodynamically stable, selected to grow over spherical seeds? What induces the twin defects described above, and what is the mechanism that removes the other shapes of NPs to leave in solution up to 90% of anisotropic NCs?[96,97]

Chen *et al.*[96] have developed a seedless growth of gold nanoplates that yields 90% of monodisperse Au seeds without any purification step. They used hexadecyltrimethylammonium chloride (CTAC) as the surfactant, and iodide ions that have already been observed to direct the anisotropic growth.[98] In a mixture of CTAC, potassium iodide and sodium tetrachloroaurate solution, ascorbic acid is added and starts the reduction of Au^{3+} ions to Au^{+}. NaOH is used to regulate the pH. The obtained nanoplates have a thickness of ≈15 nm and their edge length can be tuned from ≈40 nm to ≈120 nm by changing the concentration of precursors. When the reduction of gold ions is sped up by using $HAuCl_4$, no gold nanoplates can be obtained, showing the importance of the kinetics in obtaining anisotropic NPs (see 2.5). As without iodide no nanoplates can be obtained, it seems to play an important role in the formation of anisotropic structures. Millstone *et al.* suggested that iodide preferentially binds to {111} facets of Au nanoplates, favoring the anisotropic growth.[98] However, iodide can also play the role of selective etchant to remove less stable NCs, leaving in solution only planar structures. Indeed, iodide can oxidize metallic gold nanoparticles following the mechanism:[96]

$$4I^- + O_2 + 2H_2O = 2I_2 + 4OH^-$$

$$I_2 + I^- = I_3^-$$

$$2Au + I_3^- + I^- = 2AuI_2^-$$

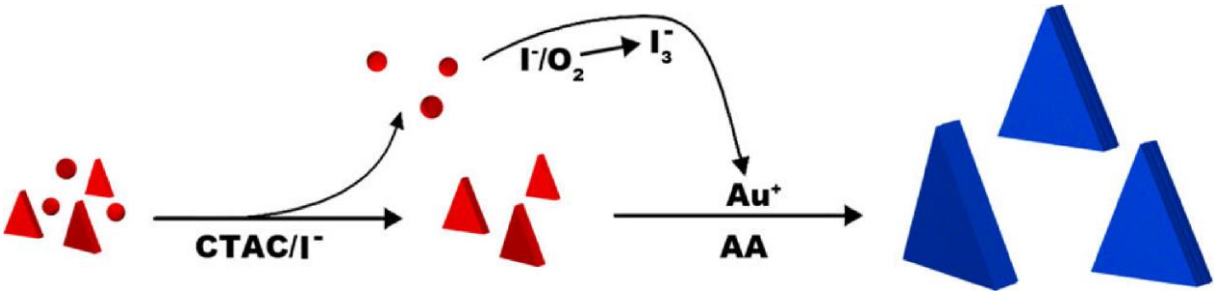

*Figure 18: Growth of Au nanoplates through oxidative etching of Au spherical nanoparticles. Reprinted with permission from ref.*96*. Copyright (2002) American Chemical Society.*

Thus, iodide ions can have a dual-function as capping agent that directs growth and as etchant that selects planar structures.

A similar etching mechanism has been observed by Zhang *et al.* during the synthesis of silver nanoplates.[48] When $AgNO_3$ is reduced with $NaBH_4$ in the presence of trisodium citrate and poly(vinylpyrrolidone) (PVP),[99] spherical Ag NPs are obtained. However, after the addition of H_2O_2, the extinction spectra showed a shoulder at 500 nm corresponding to the formation of anisotropic structures. After the optimization of the nature and ratio of reagents, Ag NPs can be obtained with a yield of 100% (with succinate and citramalate replacing the citrate). The proposed mechanism for such a high yield is that upon injection of $NaBH_4$ silver nanoparticles are produced and stabilized by the citrate and borohydride ions. However, due to the presence of H_2O_2 that acts as a etchant, a dynamic equilibrium in solution is formed between the reduction of metallic ions by $NaBH_4$ and the oxidation of metallic nanoparticles by H_2O_2 (following the equations: $Ag^0 + H_2O_2 = Ag^+ + OH^- + OH^\bullet$ and $Ag^0 + OH^\bullet = Ag^+ + OH^-$).[100] Therefore, the growth of the Ag NPs is hindered by the etchant. Over time, the $NaBH_4$ is consumed and the stabilization of the NPs weakens, allowing for their growth. Due to the presence of the etchant, the resulting NPs exhibit lots of defects, including twin planes that in turn favor planar growth. H_2O_2 thus removes less stable NPs from solution and introduces twin defects in the remaining ones.

Although the proposed mechanism differs from the previous one, Yu *et al.* also found that H_2O_2 plays a crucial role in the formation of metallic nanoplates.[101] The equilibrium between the reduction by $NaBH_4$ and the etching by H_2O_2 is still an important step. However, in basic conditions, where it exists under the form of HO_2^-, H_2O_2 acts not as an oxidant, but as a reducing agent: $Ag^+ + HO_2^- = Ag^0 + HO_2^\bullet$. The formed radical can dissociate into O_2 that further oxidizes Ag NPs to form Ag^+ ions that can be used for the growth of NPs.

This oxidative etching can be detrimental to anisotropic NPs. Indeed, single crystals are more resistant to oxidative etching that twinned NPs that present at their surface some less stable features. This is somehow contradictory to the previous mechanisms, but it is in fact complementary. The oxidative etching needs to be controlled in such a way as to introduce some twin defects in the NCs but not dissolve them completely. It is possible to selectively eliminate singly- or multiply-twinned NPs from solution by using more or less reactive agents.[102–104] Getting rid of the oxidative species might be a solution to control the etching, either by bubbling to remove the oxygen or by using proper ligands that stabilize the surface efficiently.[105–107]

The mechanism of anisotropic growth is therefore complicated, and strongly depends and the species in solution, in the environment (the oxygen present in air for instance) as well as on the speed of the reaction, the shape of the initial seeds and the ligand templating effect.

2.5. Kinetic control and selective passivation of nanoplate growth

As mentioned previously, the kinetics of the reaction also plays an important role in the shape determination of the NPs. Indeed, a change in the reduction rate of the metallic ions changes the shape of the metallic NPs. By speeding the reduction of Au^{3+} ions with $HAuCl_4$, nanospheres are obtained rather than nanoplates.[96] Similarly, iodide ions have been proposed to bind to {111} facets, stabilizing the nanoparticles, and therefore decreasing the growth rate along the corresponding direction.[108] Binding strength of halide ions is the following: $Cl^-<Br^-<I^-$, decreasing the available metallic surface that acts as a catalyst for the reduction of metal ions.[109] Besides, the reduction rate of Au^+ ions is strongly affected by the presence of halide ions in the growth solution, and the reduction rate of gold ions will be decreased with the use of a larger halide ion.[60,110] The binding of halide ions to the surface of the NPs and their influence on the reduction rate of gold ions are critical in the kinetics of Au NPs growth. For example, the use of a high concentration of iodide ions will yield nanoplates, while the use of bromide yields single crystalline cubes (Figure 19 A-C).[60] This is due to the strongly reduced reduction rate of gold ions with iodides: the growth of planar structures requires twin defects to be present in the NPs, defects that appear at low growth rate under kinetic control. Iodide, slowing down the reduction of gold ions, and limiting the availability of the NP surface, allows therefore the formation of twin defects.

This shows the importance of kinetic control in the growth of planar NPs. Slower reduction rate generally leads to more thermodynamically favored shapes with lower-energy facets while, with faster reduction rates, kinetically-controlled growth yields nanoparticles with a variety of shapes, with higher-energy facets. The limit between thermodynamic growth and kinetic growth can be determined by a critical growth speed: under the speed of deposition,

the NPs are driven to grow into their thermodynamically favored shape (plates, given they present twin defects), while speeding the deposition rate forms more complex shapes, energetically unfavorable.[53] The reducing agent used (ascorbic acid, $NaBH_4$…), the environmental conditions (pH, temperature…), as well as the use of selective adsorbents on the metallic NPs can dramatically change the growth kinetics. Ascorbic acid is a milder reducing agent than $NaBH_4$, and its reducing strength can be tuned through the change of the pH in the growth solution.[59,111] The selective passivation of a given facet also affects the growth. For example, the deposition of Ag atoms on the surface of gold NPs passivates and stabilizes these surfaces, slowing down their growth. This deposition depends on the amount of Ag^+ ions in solution, on the reducing agents used, and on the available surface of the Au NPs. Ag will deposit preferentially on the surface with a high coordination number, thus with as many Au atoms as possible.[62] (see Figure 19 D-G). The growth of planar nanoparticles is therefore not only controlled by the speed of the reaction, but also by a precise control of the stabilization ligands used for the synthesis (see part 3) and the species present in the growth solution. In the absence of Ag^+ ions, halide ions slow down the reduction of metal, slowing down the particle growth, while in the presence of Ag^+ ions, halide ions, that also bind to the surface of the NPs, destabilize the Ag layer, speeding up the growth of the NPs.[59,60] Furthermore, the growth of planar structures requires the presence of twin planes, which form during the nucleation step: the shape of the original seed is another critical parameter for the determination of the shape of the final NP.[112]

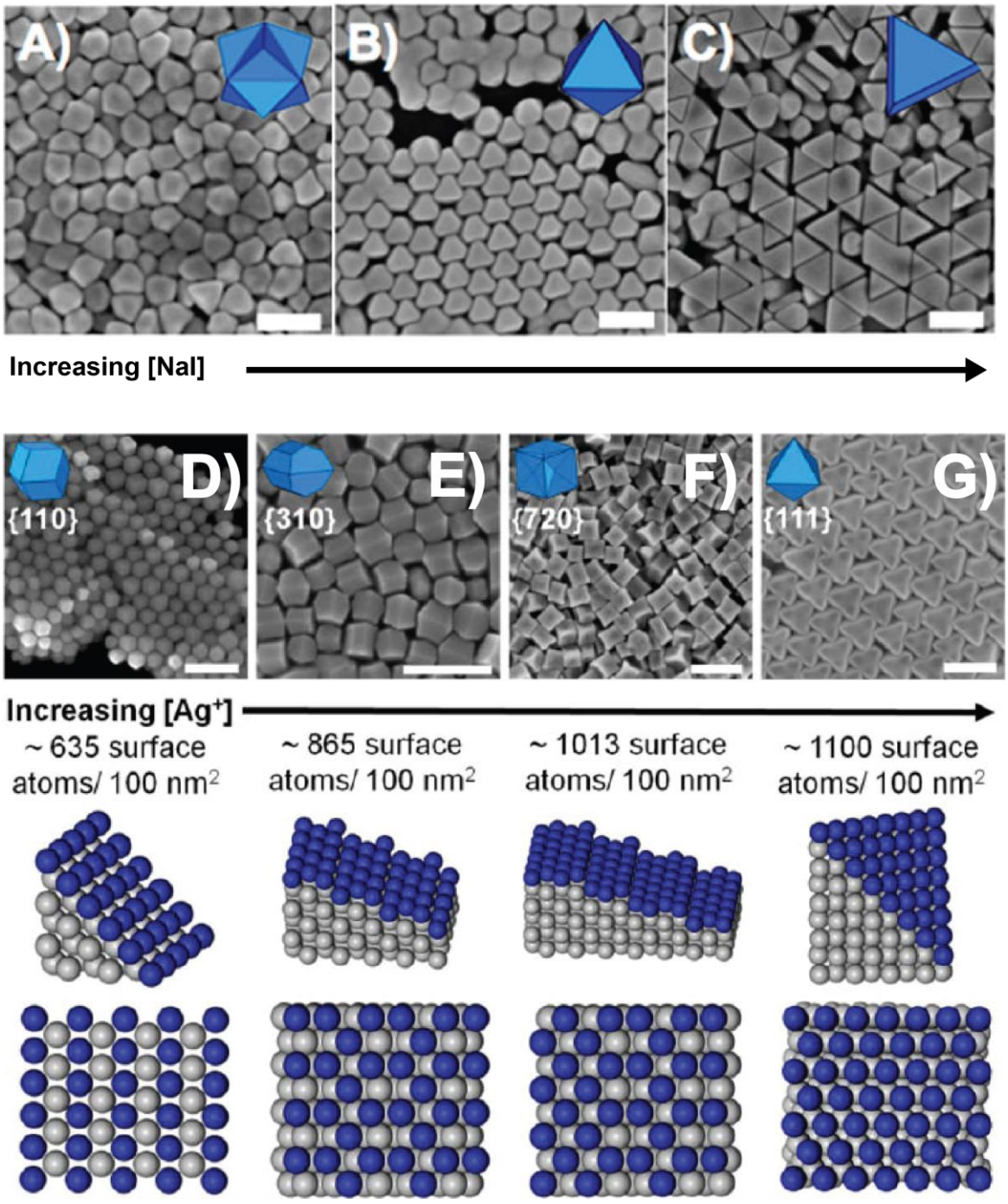

*Figure 19: (A-C) Scanning Electron Microscope (SEM) images of gold nanoparticles synthesized in the presence of (A) 0, (B) 10, and (C) 75 µM of NaI. Adapted with permission from ref.*60*. Copyright (2012) American Chemical Society. (D-G) SEM images of gold nanoparticles synthesized in the presence of an increasing concentration of Ag^+ ions. Higher concentrations of Ag^+ lead to the stabilization of facets with an increasing number of exposed surface atoms. Reprinted with permission from ref.*59*. Copyright (2013) American Chemical Society.*

Selective passivation of facets during growth also allowed to synthesize even more anisotropic structures, such as Freestanding ultrathin metallic nanosheets (FUMNSs) which

are only a few atomic-layers-thick.[113] For example, CO molecules strongly adsorbs on the {111} planes of Pd nanosheets, favoring growth in the perpendicular directions.[114]

3. Ligand engineering

3.1. Ligand templating

Since the early 2000s, it has been shown that in a synthesis the right choice of ligands could tune the shape of nanocrystals, first leading to spherical, then to rods and to multipods and finally to 2D materials[1,115,116]. In particular ligands as amines can dissolve metallic salts at room temperature leading to lamellar phases which could serve as template for the growth of nanocrystals. In addition, anisotropic crystal structures are more convenient to give rise to anisotropic shapes nanocrystals. In, 2006 Hyeon and co-workers have shown the synthesis of wurtzite CdSe nanoribbons[14] then described as a templated-growth synthesis[63]. These 2D nanoribbons or nanosheets are equivalent to quantum belts[117] and quantum platelets synthesized by Buhro and co-workers.[118] The syntheses of these materials are done below 100°C and consist of the reaction of a metallic salt dissolved in a primary amine (for example octylamine) or a mixture of a primary and a binary amine with a chalcogenide precursor such as octylammonium selenocarbamate or selenouera for selenium or trioctylphosphine tellurium (TOPTe) for tellurium. This is a soft template process. Indeed, the dissolution of a cadmium salt, either $CdCl_2$ or $Cd(Ac)_2$ (Ac = acetate), in an amine produces a lamellar amine-bilayer mesophase confirmed by low angle X-Ray diffraction. These 2D nanoparticles exhibit a wurtzite structure with the thickness in the [11-20] direction, the length in the [0001] direction and the width in the [1-100] direction. In addition to CdSe semiconductor, various semiconductors such as CdS, CdTe,[119] zinc chalcogenide,[120,121] CuS[122] or more recently PbS have been synthesized by this path.[120]

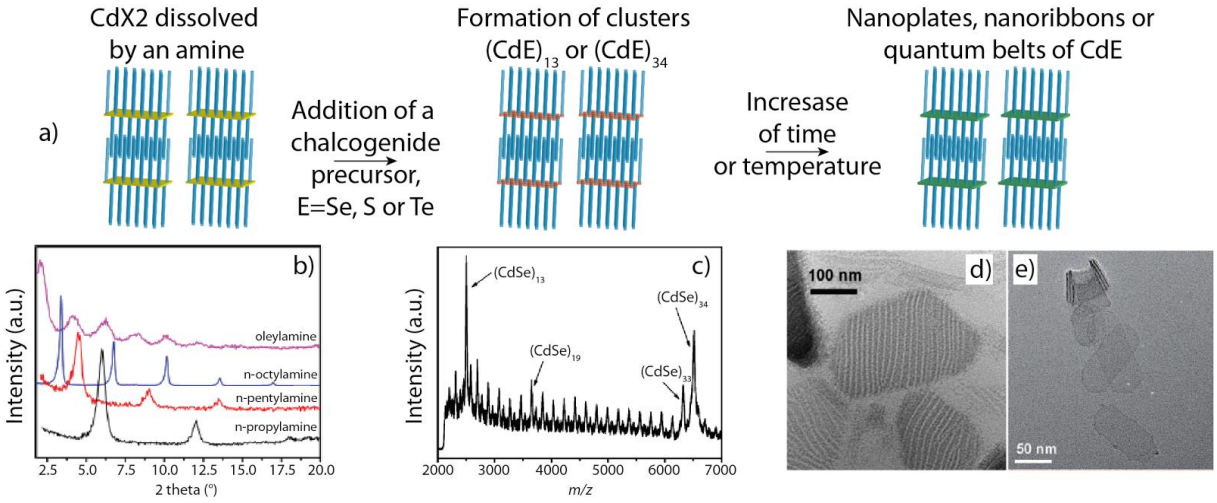

Figure 20: a) Scheme of the three steps synthesis in wurtzite 2D nanocrystals starting with dissolution of a salt in amines, then the introduction of the chalcogenide precursor, finally leading to 2D nanocrystals. b) Low angle X-ray diffraction of the lamellar structure containing

*$(CdSe)_{13}$ clusters in various amines. Adapted with permission from ref.*123*. Copyright (2013) American Chemical Society. c) LDI mass spectrum of CdSe magic-sized clusters. Reprinted with permission from ref.*124*. Copyright (2014) American Chemical Society. d) TEM image of unbundled $(CdSe)_{13}$ in the stripes. Reprinted with permission from ref.*118*. Copyright (2011) American Chemical Society. e) TEM images of CdSe nanosheets. From ref.*63*. Copyright 2009 by John Wiley & Sons, Inc. Reprinted by permission of John Wiley & Sons, Inc.*

Concerning the understanding of the growth mechanism, CdSe remains the most attractive semiconductor and the reader can refer to the following reviews.[61,125–127] The cadmium precursor dissolved in amines forms anisotropically ordered layers which will serve as templates for the nucleation and growth of the wurtzite nanoplates once the precursors of selenium is introduced. Both Hyeon[128] and Buhro's groups[118] have spectroscopically observed at the early stage of the synthesis the formation of magic sized clusters with a majority of $(CdSe)_{13}$ and $(CdSe)_{34}$. The $(CdSe)_{34}$ magic sized clusters are less thermodynamically stable than the $(CdSe)_{13}$, thus after few hours or less, only the $(CdSe)_{13}$ clusters are observed. These clusters are locked into stripes stabilized by the amines, which stack in the thickness and the width directions. If they are unbundled before the crystallization, these stripes will appear as sheets stacked along their width (Figure 20 d). The amines are weakly bound to the clusters, which favors the assembly of clusters up to the formation of nanoplatelets. Thus, these $(CdSe)_{13}$ are then converted to 2D nanocrystals, either with an annealing step at higher temperature which stay below 100°C or with a longer time of reaction (up to 48h). After crystallization the quantum belts unbundle in their width direction but are stacked in the thickness direction. The addition of a long primary amine, such as oleylamine, and sonication allows the separation of the quantum belts. The as-obtained nanoparticles have a well-defined thickness of few monolayers. The top and bottom surfaces of these platelets are nonpolar with an equal number of cadmium and chalcogenide atoms and are stabilized by uncharged amine. An increase of the reaction temperature thermodynamically favors the synthesis of thicker nanoparticles.

More recently, Buhro and co-workers[124] have also shown that instead of using a pure primary amine, a mixture of a primary and secondary amine to dissolve the cadmium precursor allows the formation of CdSe quantum platelets with pure $(CdSe)_{34}$ magic sized cluster as intermediate of the reaction at room temperature. The $(CdSe)_{34}$ clusters can also convert to the more thermodynamically stable $(CdSe)_{13}$ by lowering the temperature to 0°C, but then the annealing temperature should be higher to crystallize them in quantum platelets.

These precisely defined clusters can be achieved with different materials leading either to quantum platelets[120] or to quantum nanowires such as ZnTe.[129] These quantum wires exhibit similar optical properties as quantum platelets with well defined absorption peaks and unusually thin transitions. Wurtzite quantum platelets and zinc-blende nanoplatelets exhibit the same optical features which will be treated in section 3.2. As original objects, we can cite

the heavily doped Mn:CdSe nanoribbons resulting from the crystallization of doped $(CdSe)_{13}$ magic-sized cluster which can include up to 2 Mn atoms per cluster, meaning the clusters have for composition ($Cd_{13-n}Mn_nSe_{13}$) with n=0, 1 or 2.[128] All these nanoplates present a wurtzite structure but more recently it has been shown that PbS nanosheets which present a rock-salt cubic structure could also be synthesized by this soft template process.[120]

3.2. The case of zinc-blende cadmium chalcogenides nanoplatelets

Cadmium chalcogenides nanoplatelets are one of the most successful syntheses among 2D colloidal systems.[130] These 2D nanoparticles[127,131,132] have been named nanoribbons, nanobelts,[118] nanosheets, nanoplatelets[13] (NPLs) by the different groups.[133] What makes them appealing is their anisotropic growth controlled at the atomic scale. In these NPLs, the quantum confinement only occurs in one direction, since the lateral extension is typically larger than the Bohr radius (7nm for CdSe). Moreover, there is no roughness along the confined direction. This latter property provides the NPLs with exceptionally narrow optical features. The absence of roughness explains that there is no inhomogeneous broadening. As a result, the spectrum of a single NPL overlaps with the spectrum of the ensemble measurement, while the full width at half maximum can be as low as 7 nm.

CdSe NPLs have been investigated first.[13] Their first reported synthesis begins with a mixture made of long-chain cadmium carboxylate (myristate or oleate), selenium powder and octadecene used as non-coordinating solvent. After the degassing step, the temperature is raised. The selenium powder typically dissolves around 150°C and, quickly after that, the solution turns yellow to pale orange. At this point a second metallic precursor is introduced under a solid form and capped with short carboxylic acid (acetate typically). Generally, cadmium acetate is used but the synthesis actually works with other cations. The time of the introduction of this short carboxylic chain is critical. It has to occur when some small nanocrystals are already formed, but before the formation of large QD.

The obtained nanoplates have a parallepipedic shape. The stoichiometry of the precursor also controls the shape of the lateral extension and the shape can be tuned from square (see Figure 21 a) to rectangle. Thanks to the perfect control of their thickness, they tend to stack under pile and can even self-assemble[134,135] into µm-scale needles.[136] The lateral extension also strongly depends on the thickness of the NPL. Thinner NPLs tend to present a larger lateral extension, up to the point where they are able to roll on themselves[132,137] (see Figure 21 b).

In spite of huge progress in the synthesis of the 2D NPLs, they are generally synthetized with spherical 0D QD as by-products. As a result, a selective precipitation is generally conducted. The general procedure takes advantage of the large lateral extension of the NPLs which tends to limit their colloidal stability. Addition of a limited amount of non-solvent

(ethanol or acetone) in the crude mixture after the synthesis generally allows precipitating the NPLs while keeping the QD in solution.

To reduce the amount of solvent used during this cleaning procedure, electrophoretic sorting of the NPLs is also possible.[138] By applying a "large" electric field (400V over 1cm) on the solution resulting from the synthesis in presence of acetone, the NPLs get deposited on the positive electrode with a selectivity (defined as the ratio of the deposition rates) of 400 compared to QD.

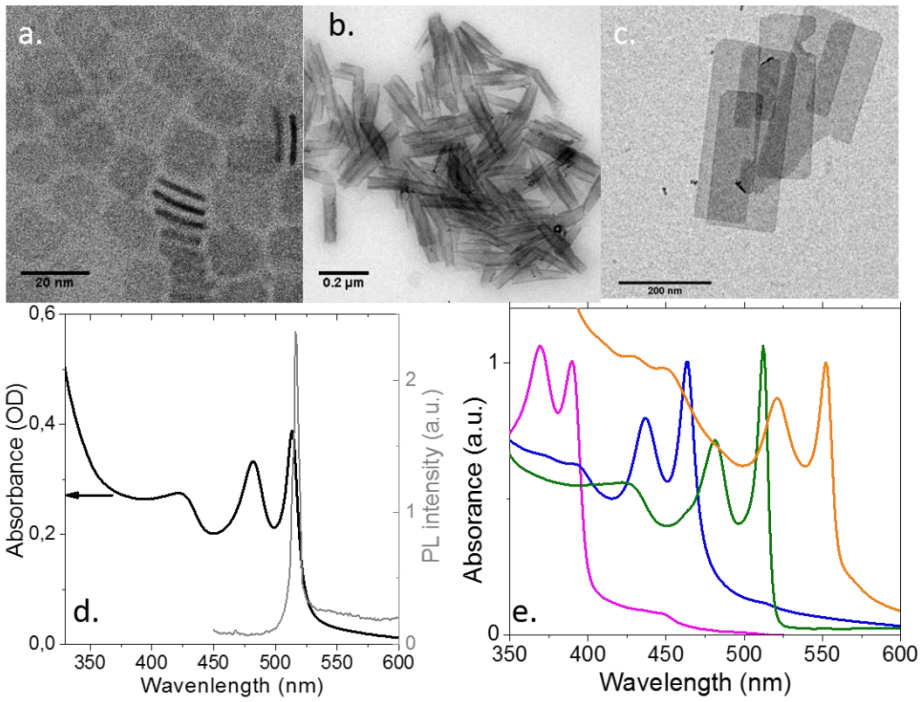

Figure 21: TEM Images of CdSe NPLs with small (a) and large lateral extension (b). The latter rolled on themselves. c. TEM image of CdTe NPLs. d Absorption and photoluminescence spectra of CdSe NPLs with a first excitonic feature at 510nm. There is almost no Stoke shift between the maximum of the absorption and the photoluminescence (PL) signal. The PL linewidth is 10nm. e. Absorption spectrum of CdSe NPLs with different thicknesses and presenting a first optical absorption feature at 390nm, 460nm, 510nm and 550nm.

The most striking property of the NPLs is their exceptionally narrow optical feature (Figure 21 d), with full width at half-maximum (FWHM) as low as 7nm for a photoluminescence (PL) signal around 500nm. Thanks to their perfectly controlled thickness, no inhomogeneous broadening is observed and the PL signal of a single NPL overlaps with the signal obtained from an ensemble.[139] The homogeneous broadening is typically below $2k_bT$. For core only structures, we obtain PL efficiency of 20%.[13] A general trend is that nanoplates with a smaller lateral extension tends to have a larger PL efficiency. We believe that such behavior result from the larger probability for the large object to include defect acting as a non-emissive

recombination center. The NPLs present almost no Stoke-shift between the energy of the absorption and the energy of the emission (see Figure 21 d). As the thickness rises, the optical features get redshifted as expected from quantum confinement.[13] However, due to the perfect control of the thickness with an integer number of layer, the optical features can no longer be controlled continuously as for spherical objects, see Figure 21 e. In the case of CdSe NPLs, different populations can be obtained with a first excitonic feature at 390, 460, 510 and 550 nm. Possibly, if the lateral extension is very small, some lateral confinement occurs and the peaks can be slightly blue-shifted. In these CdSe 2D quantum wells, the optical features have been attributed to the heavy hole-electron and light hole-electron transition.[140] The dynamics of the exciton is also strongly impacted by the 2D aspect of the nanoparticles. Indeed, the typical PL decay time of CdSe NPLs is of a few ns at room temperature, which is one order of magnitude faster than for QD at the same wavelength and with similar quantum yield. At low temperature, the exciton lifetime get even shorter and can be as low as 150 ps.[139]

From an experimental perspective, the absorption cross section and the extinction coefficient[141] have been recently determined and are of utmost interest for the determination of the NPLs concentration. Surprisingly the scale of the absorption seems to have a dependence with the surface which is superlinear.

Quickly after the synthesis of the CdSe NPLs, the procedure has been extended to other chalcogenides.[140,142] CdS nanoplates come with a large lateral extension. Compared to CdSe, their optical absorption is broader. The broadening results from the low spin-orbit coupling in CdS which tends to limit the splitting of heavy-hole and light-hole bands. As a result, the two transitions, which appear splitted in CdSe, are here only splitted by an energy smaller than their homogeneous broadening. Finally, the PL efficiency of pure CdS NPLs is low. CdTe nanoplates are the one with the narrowest excitonic features, down to 7 nm, while a value of 12 nm is more typical for CdSe NPLs. CdTe NPL are obtained using TOPTe as precursor and cadmium propionate instead of the acetate. Moreover, the CdTe NPLs are synthetized with the largest lateral extension up to 1µm (see Figure 21 c).

3.3. Thickness tunability

In this section, we will discuss the thickness tunability of zinc blende cadmium chalcogenides nanoplatelets. In this cubic structure, all the three directions x, y and z should be equivalent. Nevertheless, during the synthesis, the introduction of an acetate salt “breaks” the isotropic growth of nanocrystals and leads to nanoplatelets of 2, 3, 4 or 5 monolayers. The thickness of the nanoplatelets is in the [001] direction and a monolayer is defined as a succession of a plan of cadmium and a plan of chalcogenide in the z direction. The top and bottom surfaces are terminated by cadmium planes and are passivated by the oleate ligands

(see Figure 6). When the nanoplatelets stack, the space between two nanoplatelets is of few nm[132,134] which corresponds to two interpenetrated oleate ligands.

Although the optical properties of the CdSe zinc-blende nanoplatelets and the wurtzite quantum platelets are similar, the growth conditions are different. While for the wurtzite nanoparticles magic-sized clusters are intermediate of the reaction (discussed in section 3.1), such clusters have not been highlighted as intermediate for the zinc-blende nanoplatelets.[130] If the growth of zinc-blende nanoplatelets occurs via the formation of some magic-sized clusters, they react much faster than they are produced and it remains difficult to isolate them.

Thus, the growth of zinc-blende nanoplatelets can be seen as a two-step process: (1) nucleation of nanocrystals and (2) growth of nanocrystals up to some sizes which are seeds for nanoplatelets, followed by the lateral extension of these seeds leading to nanoplatelets initiated by an acetate or a propionate salt[130] ($Cd(prop)_2$) (see Figure 22 a). During the growth of the nanoplatelets, the exciton absorption spectra continuously red shifts as the nanoplatelets grow, expressing the weakening of the quantum confinement from 0D nanocrystals to 2D nanomaterials. It should be pointed out, that in 2014 Asaula and co-workers[143] have synthesized CdSe nanoplatelets with pure cadmium octanoate in the presence of selenourea without using a mixture of a short and a long carboxylate chain. Nevertheless, the crystal structure of the synthesized nanoplates remains unclear. In the following discussion we will mostly focus on the syntheses with mixture of two carboxylate chains.

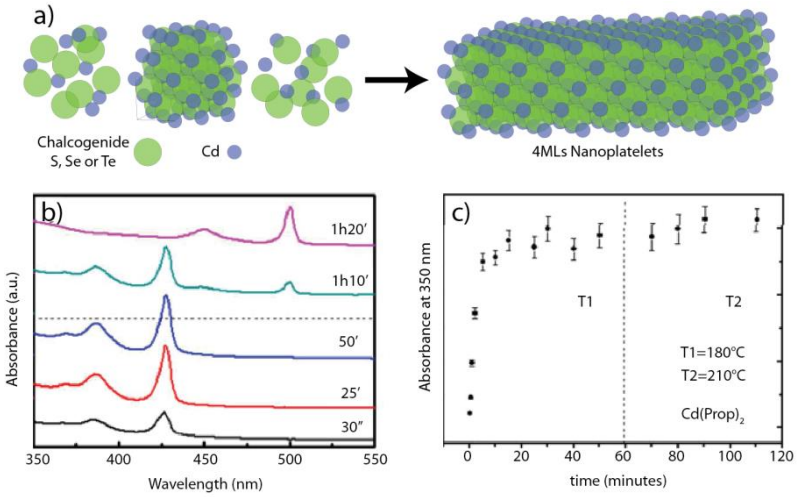

*Figure 22: a) Scheme of the two-step growth of cadmium chalcogenide nanoplatelets, b) absorption spectra of CdTe nanoplatelets at different times during a reaction first at 180°C and then at 210°C (dashed line) with $Cd(prop)_2$ as a short chain carboxylate. c) Absorbance at 350nm as a function of time for the CdTe nanoplatelets growth. Adapted with permission from ref.*142*. Copyright (2013) American Chemical Society.*

Nanoplatelets of 2 and 3 monolayers (MLs) are the easiest to synthesize. Indeed, a mixture of $Cd(RCOO^-)_2$ ($R=CH_3$ or C_2H_5) and $Cd(R'COO-)_2$ ($R'=C_nH_{2n+1}$ with $n>14$) in presence of a chalcogenide precursor in mild heating conditions (lower than 220°C) are sufficient to synthetize the two thinnest populations of nanoplatelets without production of quantum dots as byproducts. It is also possible to anneal 2MLs nanoplatelets to get 3MLs nanoplatelets. As an example, Figure 22 b and c present the absorption spectra of constant volume aliquots of CdTe nanoplatelets during a reaction and their optical density at 350 nm as a function of time.[142] During the first step of the synthesis, 2MLs nanoplatelets are formed absorbing at 428 nm for their first excitonic peak. After 15 minutes the absorption at 350 nm - which reflects the total amount of crystalline CdTe - is stable, so all the precursors were consumed. Finally, after 60 minutes at 180°C, the temperature is increased up to 220°C, and a change in the absorption spectra occurs. The thinnest nanoplatelets of 2MLs disappear in favor of the 3MLs nanoplatelets but with a constant optical density at 350 nm. It seems that the transformation comes from either an intra-reorganization of the nanoplatelets or from a dissolution of the 2MLs NPLs and a fast recrystallization of 3MLs NPLs. There is no addition of free precursors in solution on top of the already existing nanoplatelets since the total amount of crystalline CdTe remains constant (if there was deposition of an additional layer in the thickness, it should lead to an increase of 40% of the absorption at 350 nm). Moreover, we could have expected an increase of two monolayers instead of one (leading to nanoplatelets with their first excitonic peak at 555 nm), since the NPLs present two equal opposite surfaces which should react the same way. In general, higher temperature leads to thicker nanoplatelets. This transformation from 2MLs to 3MLs nanoplatelets may be explained by the really thin thickness of the initial nanoplatelets of only one lattice parameter. The relaxation of the top and bottom surfaces induced by the ligands may weaken the crystalline structure of the nanoplatelets which present 40% of their atoms on their surface. Besides, the annealing may cause a rearrangement of the atoms leading to more stable 3MLs crystalline nanoplatelets with only 28% (2/7) of their atoms on their surface. Another interesting feature is the total transformation from 2MLs-thick nanoplatelets to 3MLs-thick nanoplatelets. Indeed, once a 2D nucleus appears on surface of a NPL, the subsequent monolayer growth happens rapidly[144] in order to minimize the surface energy.[125]

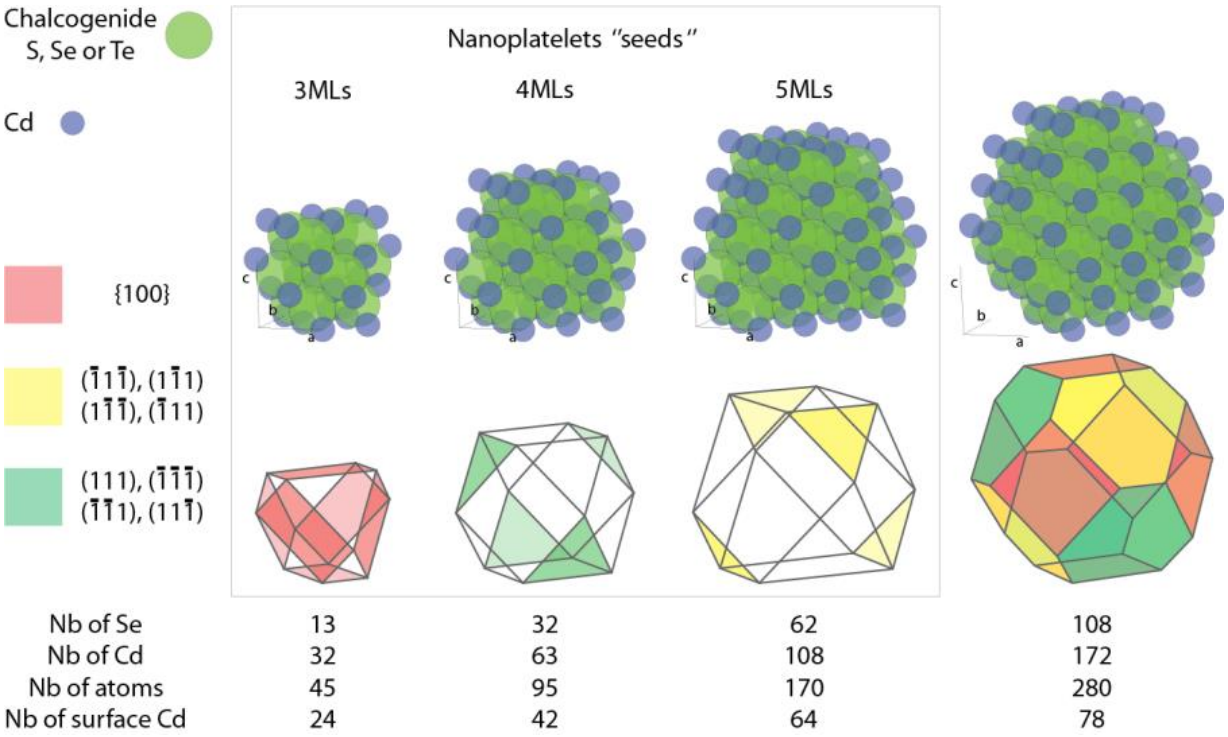

Figure 23: Scheme of CdE (E= S, Se or Te) nanocrystals, "seeds" of the 3, 4 and 5MLs nanoplatelets. The different facets are represented in red for the direction <100> and in green and yellow for the direction <111>. Number of atoms in the nanocrystals and on their surfaces.

Unfortunately, the thickest nanoplatelets cannot be obtained the same way, except for CdS as it would be explained in the next paragraph.[144] In the following discussion, we will mostly focus on CdSe nanoplatelets, a model material in the II-VI semiconductors. In order to synthesize 4MLs and 5MLs nanoplatelets, it is necessary to overpass a limit size of nanocrystals, the seeds of nanoplatelets, to grow thickest nanoplatelets at the expense of thinnest. A simple way to describe the synthesis of thicker-than-3MLs zinc-blende (ZB) nanoplatelets is a homogeneous growth of "spherical" quantum dots which can reach critical sizes - the thickness of the nanoplatelets - followed by their lateral extension initiated by the introduction of a short aliphatic carboxylate chain salt such as cadmium acetate or cadmium propionate. Thus, for 2MLs, the seeds size would be 7.6 Å, and for 3MLs (resp. 4MLs and 5MLs) it would be 10.64 Å (resp 13.7 Å and 16.74 Å). Figure 23 shows the ideal crystalline seeds for the 3MLs, 4MLs and 5MLs nanoplatelets exhibiting both {100} and {111} facets. During these syntheses, the nucleation rate should be low enough to keep in solution enough precursors for the lateral extension. Then, one would expect that with bigger nanocrystals seeds, it would be possible to reach thicker-than-5MLs nanoplatelets. Nevertheless, these kinetics considerations do not take into account the crystal structure and the stability of the facets. And, during the growth, a crystal minimizes its surface energy which also depends on the ligands and their ability to stabilize facets. Regarding the packing density and the number of unsaturated atoms of the {111} and the {100} facets, the surface energy of the {100} facet is

smaller than the {111} facets, thus the growth of atoms on these latest is favored.[145] On the other hand, the calculated values of the adsorption energy of oleic acid on both plans show that oleic acid would stabilize {100} plans less than {111} plans.[145] Thus, depending on the temperature of reaction and the ligands, it is in some points possible to tune the shape of the nanocrystals. Here, during the synthesis of nanoplatelets, a short carboxylate aliphatic chain (less than three carbons) with a low boiling point is introduced. The acetate or propionate salt will lower the influence of the facet stabilization energy by the ligands, due to a fast kinetic of adsorption and desorption with short chain ligands. This will favor the growth of nanocrystals with low-index crystallographic planes such as the {001} facets. The nanoplatelets are indeed exhibiting the top and bottom facets as cadmium rich {001} facets stabilized by oleate ligands, not acetate ligands which are too small to stabilize NPLs in non-polar solvent. Nevertheless, it does not explain the breaking in the isotropic growth which, instead of giving cubic nanocrystals, leads to nanoplatelets. For the four existing populations of nanoplatelets (2 to 5MLs), the seeds diameter would be inferior to 1.7 nm with a number of atoms inferior to 200 with more than 30% of them on the surface (see Figure 23). For the two thickest populations of nanoplatelets, the synthesis requires a first step of growth without the acetate (resp. propionate) salt, where spherical zinc-blende nanocrystals are obtained with mostly cadmium rich surfaces, since cadmium is in excess and the only ligands are oleate which can mostly bind cations. Once the acetate salt is introduced at high temperature (superior to 190°C), equilibrium of exchange may happen on the different facets between acetate and oleate. Presumably, regarding the oleate steric hindrance compared to acetate, acetate capping nanocrystals would mostly exchange with oleate on two opposite facets. With a simultaneous precursor reaction, it can lead to the growth of nanoplatelets. Given this fact, it could explain the difficulty to synthesize nanoplatelets thicker than 5MLs. If the growth conditions imply first spherical nanocrystals, they will typically exhibit both {100} and {111} facets and the larger the nanocrystals, the larger the surface of these facets. By supposing that the seeds of 6MLs nanoplatelets are 2 nm nanocrystals (6.5 monolayers x lattice parameter of 0.304nm = 1.976nm), the probability to exhibit the {100} facets in all the six directions is higher than for smaller nanocrystals. And despite the introduction of the short ligands, two facets perpendicular to each other may be stabilized by the oleate thus blocking the anisotropic growth. This limitation may be overpass with a better control of the syntheses.

It should be pointed out that Peng and co-workers[144] have successfully synthesized pure CdS nanodisks with similar optical properties as nanoplatelets[140] of four pure populations. In these syntheses, all the precursors including cadmium acetate dihydrate, sulfur and a fatty acid, are conjointly introduced in octadecene in a three-neck flask and are heated to various temperatures under inert atmosphere. In addition to the annealing temperature and reaction duration, the choice of the fatty acid is a key factor to control the thickness of the nanodisks.

Thus, as for other materials the two thinnest populations of nanodisks could be synthesized in mild conditions with various fatty acids of moderated hydrocarbon chain length from C_{14} (myristic acid) to C_{18} (oleic acid). On the other hand, the only way to get the pure thickest population seems to be the use of a fatty acid with an unusually long hydrocarbon chain: the melissic acid (C_{30}). This observation is in accordance with the fact that thick CdSe nanoplatelets are better stabilized by longer chains.[64] Thus, if the synthesized nanodisks are too thin, they will tend to grow in the thickness to reach a better stabilization with the ligands present in the reaction mixture.

3.4. Colloidal 2D heterostructures

NPLs combine very narrow optical features with fast PL decay, which makes them appealing candidates for next generation quantum emitters, but also for more applied perspectives such as their use as display phosphors or for lasing. In this sense boosting further their luminescence yield is of utmost interest. For spherical objects, the well-established strategies is the *in situ* growth of an heteostructure.[146] With type-I and quasi-type-II band alignment (see Figure 24 a and b), the exciton wavefunction is more confined within the core and has less opportunity to visit the surface defects. As a result, the PL efficiency can be boosted. Alternatively type-II band alignment (see Figure 24 c), provides the exciton with a mixed material character and in particular allows shifting of the optical features below the band gap of each material. In this section we discuss the specific growth method of the 2D colloidal heterostructures. The latter can be obtained either thanks to isotropic growth leading to core/shell structures or only in their plane to achieve core/crown objects.

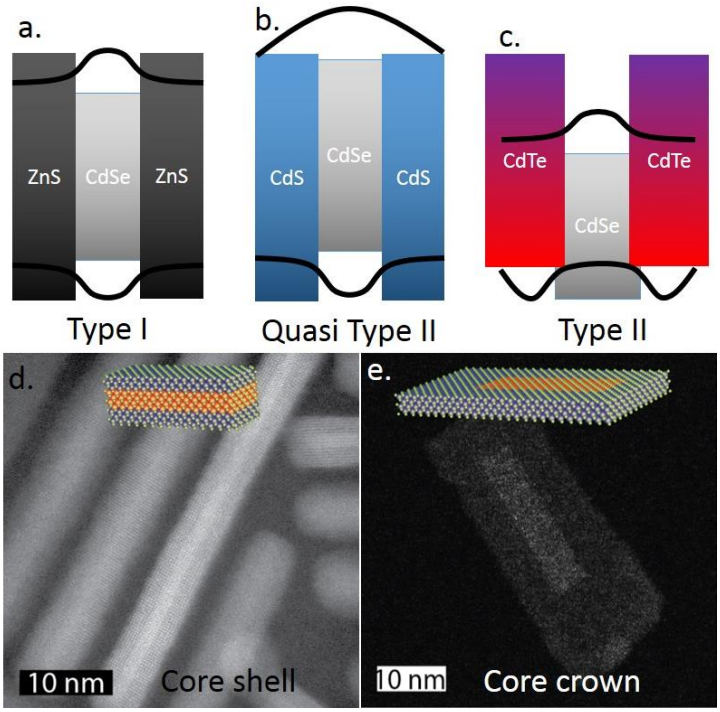

Figure 24 : Scheme of a heterostructure band strcture with a type-I (a), quasi-type-II (b) and type-II (c) band aligment. d TEM image of a core/shell (CdSe/CdS) NPL. The inset is a scheme of the core/shell heterostrcture e. TEM image of a core/crown (CdSe/CdS) NPL. The inset is a scheme of the core/crown heterostructure.

3.4.1. Core-shell

Cadmium chalcogenides nanoplates remain fragile objects and so far most of the high temperature approach to grow heterostructures based on method developed for 0D QD have been unsuccessful. Introducing the NPLs at low temperature in presence of amine strongly broadens the excitonic feature due to ligand exchange. However, such core/shell structures are good candidates to boost the PL efficiency. Alternative low temperature methods have thus been developed.

A first method proposed by Mahler *et al*[147] relies on the *in situ* formation of H_2S. CdSe NPLs, thioacetamide, cadmium nitrate and octylamine are mixed in chloroform. The reaction of thioacetamide with the amine leads to the *in situ* formation of an ammonium sulfide, acting as the sulfur precursor. The reaction is conducted for a couple of hours at 70°C and has been used to grow CdS and CdZnS shells with typical thicknesses of the order of 3.5 monolayers (see Figure 24 d).

With the growth of the shell, a significant redshift is observed resulting from the decrease of the confinement direction, *i.e.* the thickness. Current core/shell structures based on cadmium chalcogenides present a red excitonic feature (630-670nm). Their PL efficiency

can be as high as 80%,[148] however this method suffer from a limited reproducibility. As the shell is grown, the linewidth of the PL emission rises but remains between 19 and 25 nm (depending on the nature of the shell and the thickness) which is still below the value obtained for spherical QDs (see Figure 25 a and b).

The previous approach only offers a limited tunability on the thickness shell. Another low temperature approach has been developed to offer as for SILAR[149] (Successive Ionic Layer Adsorption and Reaction) the possibility to grow the shell layer by layer. The procedure has been named colloidal ALD.[150] Similarly to the atomic layer deposition, the process is self-limited. In this case, the growth is conducted in polar medium, which allows the direct use of S^{2-} precursor as sulfide source. The growth relies first on the phase transfer of the NPLs from a non-polar phase where the NPLs are suspended with oleate ligands to a polar phase (dimethylformamide as solvent) where the new ligands are typically S^{2-} or SH^{-}. The ligands react with the nanocrystal surface which comes with a change of color resulting from the partial extension of the carrier wavefunction in the newly formed sulfide layer. After the washing of the excess ligands, some cadmium precursor is added in the polar phase; again, the color of the reaction medium redshifts. The reaction can be continued by successively introducing the Cd and S precursors and washing the unreacted precursors between each step. Compared to the previous method, this procedure allows the fine tuning of the shell thickness. Moreover, this method allows tuning the surface from cation-rich to anion-rich and thus to adjust the surface gating. In particular, this method has been used to tune the nature of the majority carriers (electron or hole) in thin-film transistors based on narrow band-gap transistors.[151,152]

This method has also been extended to other chalcogenides such as Se[153] and Te, however selenide and telluride precursors are not available under a commercial and stable form. Thus a preliminary reduction step of the chalcogenides by a strong reducing agent (sodium borohydride) is necessary. Moreover the growth of the shell needs to be conducted air free.

These low temperature growths of the shell have led to improved performances in terms of PL efficiency. However there is still a need to develop a high temperature shell growth to obtain more reliable syntheses and a lower density of defects, leading to even higher PL yields.

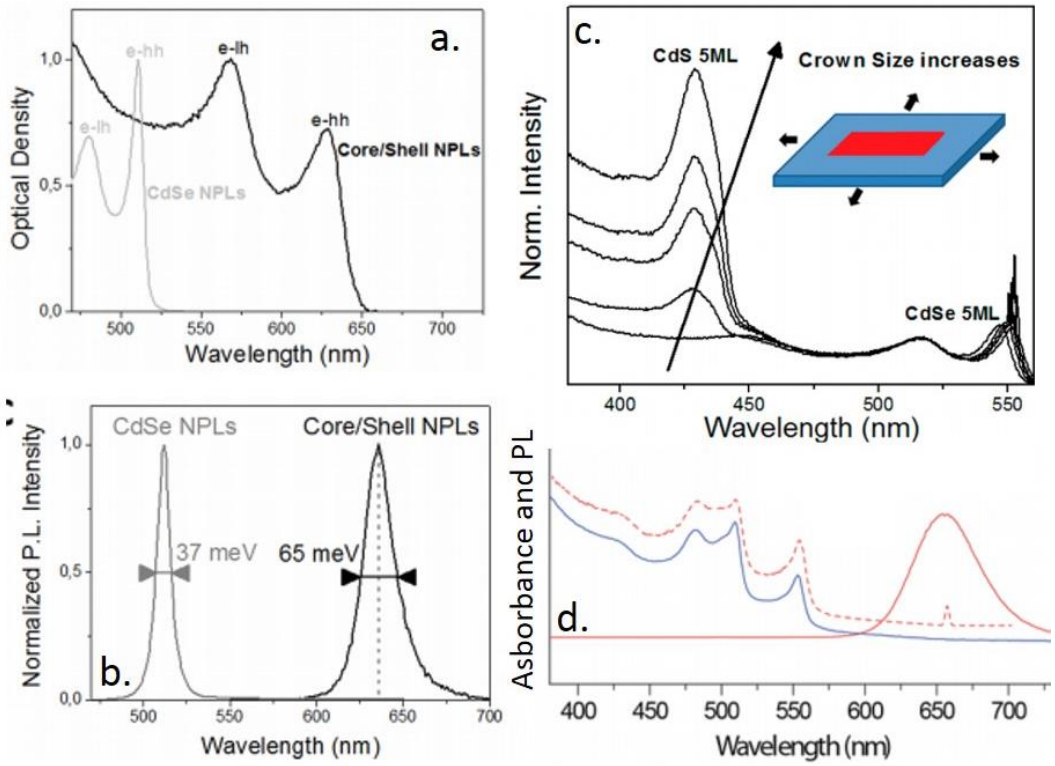

*Figure 25 : Absorption (a) and photoluminescence (b) spectra of CdSe core and CdSe/CdS core/shell. Adapted with permission from ref.*148*. Copyright (2013) American Chemical Society. c. Photoluminescence excitation spectrum of CdSe/CdS core/crown NPLs with different lateral extension of the CdS crown. Adapted with permission from ref.*154*. Copyright (2014) American Chemical Society. d. Photoluminescence (red line), photoluminescence excitation (dashed line) and absorption spectra (blue line) of CdSe-CdTe core crown NPLs. Adapted with permission from ref.*155*. Copyright (2014) American Chemical Society. The PL signal is strongly redshifted compared to the absorption of both CdSe (absorption at 510nm) and CdTe (absorption at 560nm) confirming the type-II band alignment.*

3.4.2. Core-crown

While the growth of a shell is isotropic and occurs over all the facets of the NPLs, the 2D shape allows another growth mode occurring only in the plane direction.[69,156] In this case we rather obtain core –crown objects[154] (see Figure 24 e).

The reaction is conducted in a medium very similar to the one used to grow the core and which has to favor the 2D growth rather than secondary nucleation. In a typical reaction, a mixture of cadmium oleate and acetate is first prepared. Then the core NPLs are added and this step is followed by the quick addition of the S precursor (sulfur in octadecene, or S-ODE). The core NPLs are used as nucleation sites and a surrounding CdS layer is formed. The lateral extension of the crown is controlled via the amount of introduced precursor and can be tuned from a few lattice parameters up to 100 nm. Core/crown CdSe/CdS NPLs present a fairly high PL efficiency (60%), while maintaining their narrow emission linewidth (less than 15nm).

The CdS crown is actively absorbing and the absorption spectrum presents a typical increase around 500 nm due to the CdS (see Figure 25 c). However the PL signal remains driven by the CdSe core and no PL coming from CdS is observed (see Figure 25 c). This actually results from the fast transfer of the hole to the CdSe due to more favorable confinement, which is followed by the transfer of the electron due to the large binding energy of the exciton in the NPLs. As a result, the CdSe core behaves as the emissive recombination center.

The core/crown heterostructure has been extended to type-II band alignment.[155,157] In this case, the crown is made of CdTe. Te under the form of TOP-Te is used instead of the S-ODE. Thanks to the band alignment between CdSe and CdTe the PL signal can be pushed further than the bulk band gap of each material (800nm) (see Figure 25 d). Due to the reduced wavefunction overlap, the electron being localized within the CdSe and the hole within the CdTe, the recombination of the electron hole pair become less likely to happen and long lifetime are observed (200-300ns).

3.5. Alloying and doping:

3.5.1. Alloying

Because of the perfect control of the thickness in the cadmium chalcogenides nanoplatelets, there is no inhomogeneous broadening of the optical features. However this comes at the price of the loss of continuous tunability of the optical properties (see Figure 21 e). To recover this tunability of the optical features, alloying of the CdSe NPLs with S[158] and Te have been proposed.

Alloying with sulphide is used to obtain tunability between the blue and the green (see Figure 26 a). It is simply obtained by mixing sulphide powder with the selenium precursor.[159,160] Alternatively selenium disulphide can also replace the mixture of Se and S in a 1:2 stoechiometry.

The Te alloying is, on the other hand, used to redshift the optical properties of the CdSe NPLs. The introduction of the Te precursor can either be done under Te or TOP-Te form. Nevertheless, the modification of the optical properties are more complex than with sulphide, because of a large bowing effect (see Figure 26 b). Instead of a linear dependence between the pure CdSe and CdTe phase, Tenne *et al*[161] observed a redshift of the transition (toward smaller energy than the smaller band gap material) as well as a large broadening of the PL linewidth.

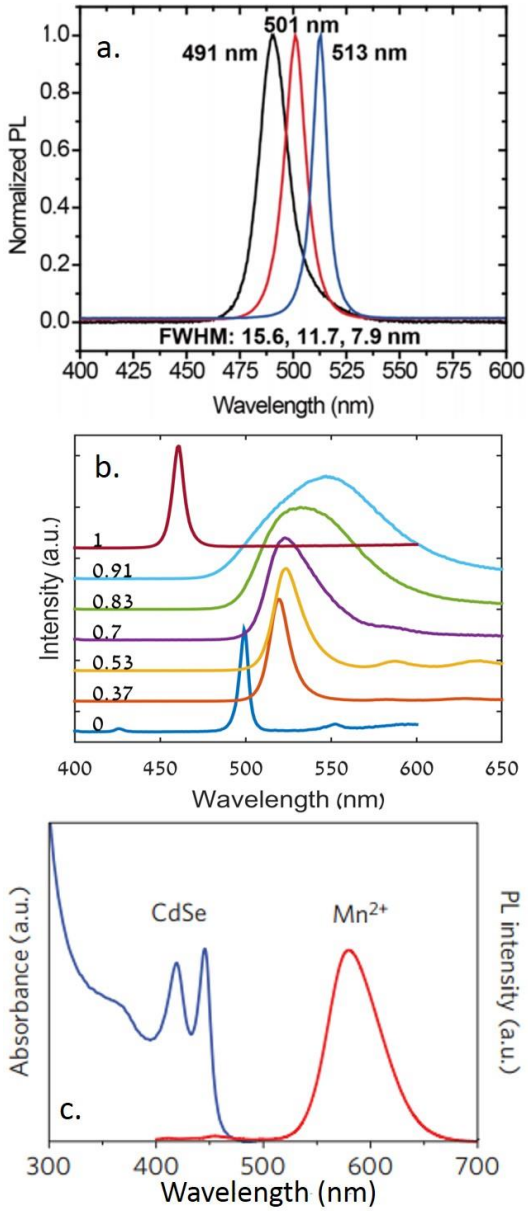

*Figure 26: a. Photoluminescence spectrum of CdSSe NPLs with different ratios of S and Se, adapted with permission from ref.*159*. Copyright (2015) American Chemical Society. b. Photoluminescence spectrum of CdSeTe NPLs, with different ratios of Te and Se. 1 corresponds to the Pure CdSe phase while 0 corresponds to the CdTe phase. The data evidences a bowing effect. Adapted from ref.* 161*. c. Absorption and photoluminescence spectrum of Mn doped CdSe ribbons. Reprinted by permission from Macmillan Publishers Ltd: Nature Materials from ref.* 128*, copyright (2010).*

3.5.2. Doping

The control of the optical and electrical properties of the NPLs also comes through their doping. So far no work has studied the electrical doping of the NPLs. On the other hand, magnetic doping by Mn^{2+} has been reported using wurtzite CdSe nanoribbons.[128] The

introduction of the cation is somehow tricky since acetate precursor will not lead to Mn incorporation but the acetate will rather be used as ligand. It was proposed to introduce the manganese ions under $MnCl_2$ form and their incorporation has been pushed up to 10% where it saturates. The manganese ions are indeed located in the bulk of the structure rather than on the surface as evidenced by the manganese phosphorescence (see Figure 26 c).

3.6. Hybrid system

3.6.1. SiO_2 encapsulation

The encapsulation of NPLs into an inorganic matrix raised some interest to ensure their surface passivation. Moreover, such protective coating is highly desirable in their use as phosphor for displays (see the discussion in section 7.2). One successful method achieved encapsulation of NPLs in a silica coating.[162] The synthesis allows a conformal growth of a thin (3-20nm) silica shell around the NPLs. To do so, tetraethylorthosilicate is used as the silicon precursor and the reaction is slowly conducted in a basic medium. Such functionalization may also be used as a spacer while trying to couple the NPLs to plasmonic structures.[163]

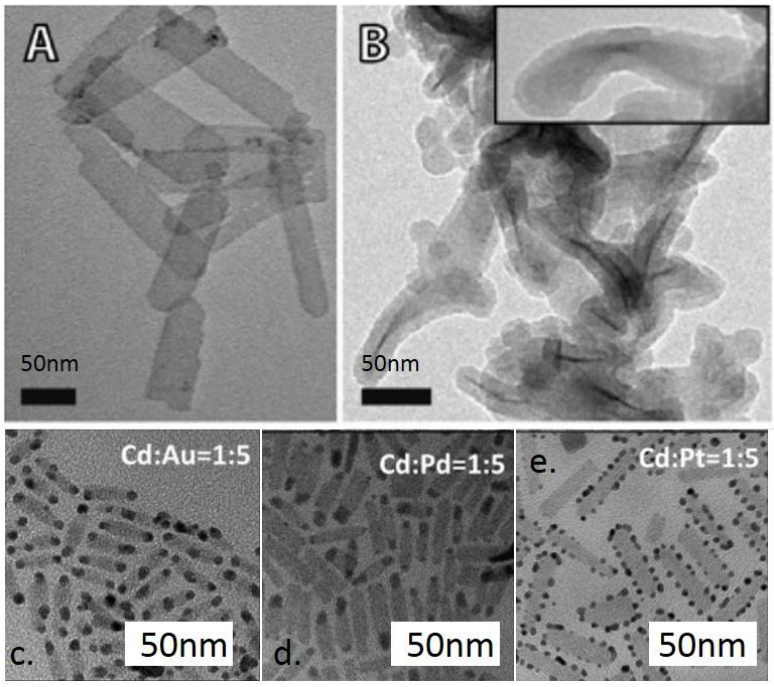

*Figure 27 : TEM images of CdSe nanoplates before (a) and after (b) their coating by a thin SiO_2 layer. Adapted from ref.*162*. Copyright (2014) American Chemical Society. c, d and e are respectively TEM images of CdSe nanoplates functionalized with gold, palladium and platinum tips. Adapted with permission from ref.*164*. Copyright (2015) American Chemical Society.*

3.6.2. Metal functionalization

The metal functionalization of the NPLs is of utmost interest to tune their transport[165,166] and photocatalytic properties.[167] It has been successfully reported with Au[117,164], Pd,[164] Pt[164] and Ni.[167] The general method is close to the one developed to functionalized nanorods.[168,169] It typically relies on the metal salt reduction in presence of amine used as metal ions reducer and some ligands (didecyldimethylammonium bromide). The reaction occurs at temperatures as low as room temperature. The tips are typically located on the edges of the NPLs (see Figure 27 c-e), and come under the form of small metallic bids. Their size typically ranges from 2 to 10 nm.

4. Self-assembly

While the previously described methods to induce anisotropy rely on molecular precursors, self-assembly differs from these methods in the sense that the elementary brick is far larger than the atomic lattice. In this section, we describe the growth of large structures obtained by assembly of colloidal nanocrystals.[170–172] Here we voluntarily discard the "usual" self-assembly of nanocrystals which has been discussed in several reviews[173–175] to focus on the self-assembly occurring during the synthesis and leading to an epitaxial connection between the nanocrystals. We in particular focus on lead chalcogenides (IV-VI compounds) which are typically obtained with this growth process.[176]

4.1. The case of lead chalcogenides self-assembly

Leads chalcogenides compounds are known to be able to form a broad range of nanocrystal shapes from 0D spherical objects to nanocubes,[177] wires[178] and stars[179] (see Figure 28 a-d). The different shapes are obtained by tuning the reaction conditions (temperature, coordination of the solvent, presence of coligand), but they actually all result from the assembly of small nanocrystals. While all shapes and dimensionalities are accessible with this material, 2D sheets have been one of the last to be obtained[180] (see Figure 28 e and f).

The synthesis of 2D sheets of PbS relies on two critical parameters[175]: (i) first the reaction is conducted far from stoichiometry. There is a lead excess compared to sulfide[181,182] by a factor 20 to 1000. Such Pb:S ratio aimed to promote the nucleation step rather than the growth. It leads to the formation of small nanocrystals (3nm and less). The second critical point (ii) is the introduction of chloroalcane (trichloroethylene). Its exact role remains unclear, but halides are also pointed as a source of anisotropy for metal nanoparticles,[183] but have to be introduced in the early time of the reaction. Due to the low boiling point of this chloroalcane, it cannot be introduced until the degassing steps are finished. The chlorine is certainly used to

prevent the growth along certain facets and promote the attachment along the [110] direction[180,181].

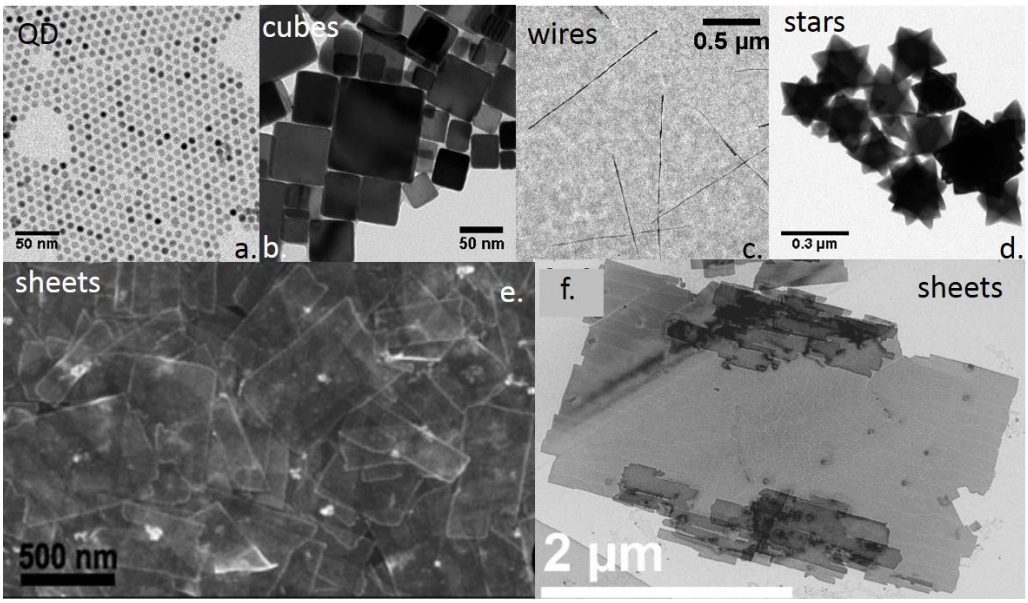

Figure 28 : TEM images of PbSe QD (a), cubes (b), wires (c) and stars (d). e is an SEM image of PbS sheet, adapted from ref 181 *with permission of The Royal Society of Chemistry . f. is a TEM image of a PbS sheet. Reprinted with permission from ref.*184*. Copyright (2012), American Institute of Physics.*

The obtained sheets have a tunable thickness[180] from 2 to 50 nm[185] typically. Their lateral extension is generally quite large[184] from 200 nm up to 10 µm (see Figure 28 f). However, their surface is not as well controlled as for cadmium chalcogenides nanoplates obtained with the ligand templating method and the optical features are even broader than for quantum dots of the same size and composition. The PbS nanosheets also present PL signal typically in the near IR[186] and telecom wavelengths.[182] The PL efficiency is around 6 % and can be raised to 11 % by growing a CdS[187] shell. The latter is obtained through a cation exchange process while the dots are heated in a solution of cadmium oleate at moderate temperature (60 to 100°C). PbS nanosheets have also attracted a large interest because of their large extension which make them good candidates for single nanocrystal electronics and for their use as transistors[184] and for photovoltaics.[188,189]

4.2. Colloidal structure with 2-x dimensionality

Among the 2D class of colloidally prepared lead chalcogenides nanomaterial, some special networks need to be mentioned. By self-assembling small lead chalcogenide nanocrystals, square and honeycomb lattices can be formed.[190] They have been proposed almost simultaneously by the Hanrath's[191] and the Vanmaekelbergh's groups.[190] Since they are full of holes, their dimensionality[192] lies between 1 and 2. What makes such structure appealing is

that for the first time it is possible to obtain a colloidal-nanocrystal-based self-assembly structure combing both order and high degree of coupling between nanoparticles. So far there was really two types of structures. On the one hand, it was possible to make self-assembly structures with high coherence length (up to mm), but due to the presence of long capping ligands, nanocrystals were not electronically coupled between each other. On the other hand, nanocrystals have been used under thin film form for transport, but in this case the main concern regards the local coupling rather than the long distance order. To achieve large coupling, ligand exchange toward short ligands is performed,[193,194] but it degrades the film quality by shrinking the volume of the film and forming cracks. This new type of assembly, combining order and coupling is appealing to conduct material engineering at the nanoscale and formed artificial crystals.

The most successful path to build such mesocrystal is to assemble the nanocrystals at a liquid-air interface. Among the large zoology of shape (Figure 28) that can be obtained by self-assembling lead chalcogenide nanocrystals, this method inherently induces anisotropy towards a sheet form. In a typical preparation, a PbSe nanocrystal solution dispersed in toluene with a sub µM concentration is deposited on the top of ethylene glycol.[190] The two liquids are not miscible and due to the lower boiling point of toluene, the latter quickly evaporate. It leaves nanocrystals on the top of glycol. At first the QDs entropically get order on a hexagonal phase,[195] where the ligands remain present. To observe the necking of the QDs, the bottom phase needs to have some affinity with the QD capping ligands[191] and it is generally admitted that air free conditions[190,191] are necessary to induce this assembly of the nanocrystals and their assembly into square and honeycomb lattice. The removing of the ligands from the nanocrystal surface will induce the fusion of their facets.[196] If the (100) facets merge, the square lattice is obtained (see Figure 29 c), while the honeycomb lattice results from the fusion of the (110) facets (see Figure 29 a and b). The latter phase is only obtained while starting from small nanocrystals (<5nm) and remains difficult to obtain. In this case, the nanocrystals are not all in the same plane and the structure is silicene like.

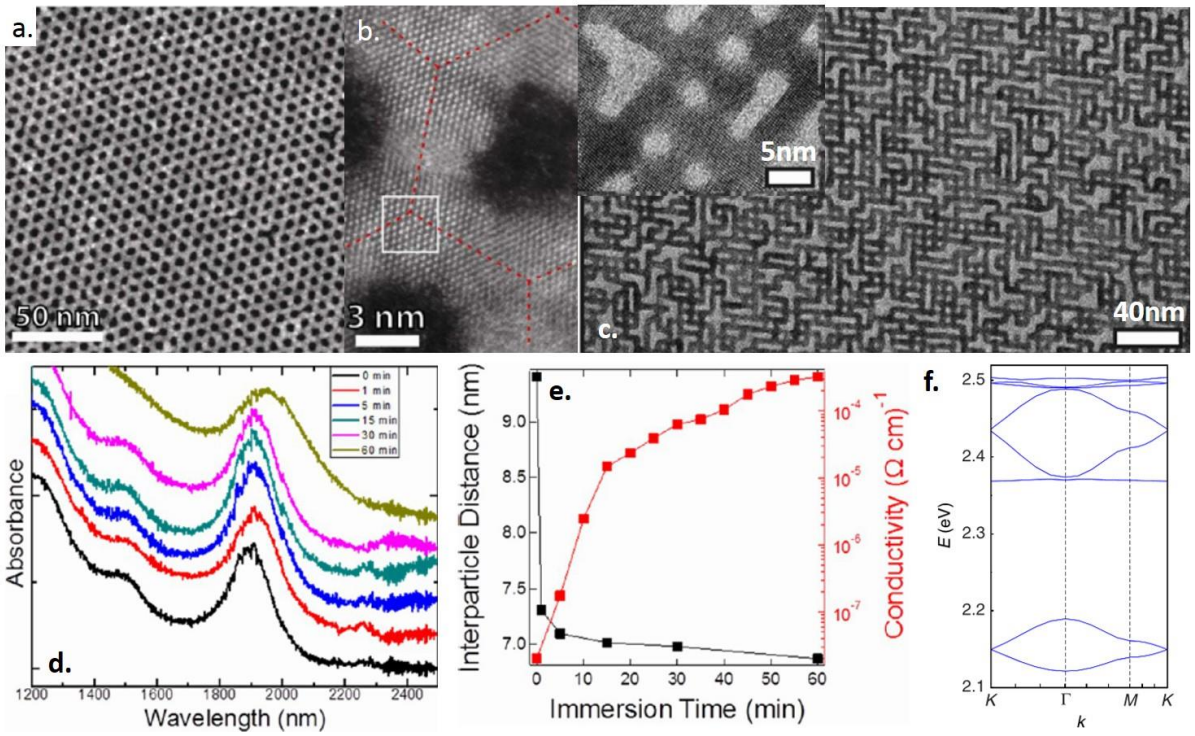

Figure 29 : a TEM image of a PbSe-nanocrystal-based honeycomb lattice. The nanocrystals appear in white. b is a zoom on the inter-dot interface. Adapted with permission from ref.[190] *Copyright (2012) American Chemical Society. c. TEM image of a PbSe-nanocrystal-based percolative network with a square geometry. Adapted from ref* 197. *d. Near-infrared absorbance of the PbSe nanocrystals before and during their assembly. The spectra broaden, but the confinement is preserved. e. Plot of the inter-dot distance and film conductivity as a function of the assembly duration. Adapted with permission from ref.*191. *Copyright (2013) American Chemical Society. f. Calculated band structure for an artificial honeycomb lattice made of HgTe. Adapted from ref.*198.

This material has also attracted a huge theoretical effort for the modeling of its band structure.[198–200] The latter is intermediate between individual QD in which the states are not dispersive and the quantum well. Indeed the mesocrystal keeps presenting some confinement and the excitonic structure is only little affected[191] (see Figure 29 d). Among the theoretical predictions regarding these structures, there are miniband states, Dirac cones (for the honeycomb lattice) and topological gap,[198](see Figure 29 f). This material can thus be seen as an artificial graphene, with several advantages such as the presence of a band gap or heavier mass with respect to carbon leading to spin orbit coupling. Miniband state is also an appealing prediction to achieve in nanocrystal solid band-like transport[201–203] and their associated large carrier mobility. Even if further experimental evidences are necessary to confirm the existence of the predicted states, improved transport properties compared with unfused nanocrystals have already been obtained. Baumgardner *et al.* reported a rise of the conductance by four

decades (see Figure 29 e), during the self-assembly process, while Evers *et al.* have measured transport mobility[197] close to $10 cm^2 V^{-1} s^{-1}$.

Finally this platform of materials is not limited to lead chalcogenides since cation exchange can be conducted towards other cations while preserving the overall mesocrystal structure. Demonstration toward cadmium chalcogenides has already been successfully obtained.[204] Achieving cation exchange towards mercury is also highly desirable from an electronic structure point of view since the final object will benefit from the inverted band structure of the HgTe[205] compound and can possibly generate some topological non trivial states[198,200].

5. Colloidal synthesis of chalcogenides with a layered crystalline structure

Chalcogenides materials possessing lamellar crystal structures have been the subject of numerous studies over the past few years. Such materials, including the transition metal dichalcogenides (TMDCs) exhibit a broad range of properties, from metals to insulators, semiconductors, superconductors, semimetals… rendering them particularly attractive for numerous applications: bio-labeling[25], photothermal therapy[206], transistors[207], lasing[208], optoelectronics[209–211], thermoelectrics, electro- and photocatalysis[212,213], photovoltaics[214], or spintronics. Furthermore, similarly to graphene, the electronic properties of these materials can undergo drastic changes when studied at the monolayer scale. For example, the indirect band-gap semiconductors MoS_2 and WS_2 become direct when reduced down to the monolayer.

5.1. Liquid phase exfoliation

The initial explorations of the electro-optical properties of monolayers have been made possible by the use of the now well known "scotch tape method" (initially used to prepare graphene sheets[26]) to physically exfoliate monolayers from microscopic crystals. The obtained layers are generally quite large and of good crystalline quality. This method has been used on numerous lamellar materials due to its ease of use and the quality of the obtained layers, but this approach is inapplicable for the preparation of large quantities of monolayers. Alternative liquid phase exfoliation strategies have then been developed to achieve larger scale production of colloidaly stable nanosheets. Liquid exfoliation of layered materials is discussed in great details in the eponymous review[27] and will only be briefly described here.

We can distinguish two different main approaches: mechanical exfoliation and exfoliation driven by intercalation. Coleman and coworkers recently demonstrated that mechanical exfoliation of layered materials powders dispersed in a solvent is possible when the solvent surface energy is similar to that of the exfoliated sheets.[215,216] In this case, the reaggregation is avoided, leading to stable dispersions of nanosheets in liquids. This strategy has been successfully applied to a broad range of materials (graphene, BN, MoS_2, WS_2, $MoSe_2$, $MoTe_2$, Bi_2Se_3, TaS_2, SnS_2, GaS…).[27,215,217,218] One can distinguish two main ways to provide the necessary energy to exfoliate the powders. The first demonstrated one has been to sonicate powders in a suitable solvent such as N-methyl-pyrrolidone (NMP)[216,219]. More recently, the same group used a shear exfoliation strategy to prepare the nanosheets.[220] This technique is very promising for large-scale production, as the synthesis has been demonstrated using very simple apparatus such as kitchen blenders.[221] Diverse solvents are suitable for these mechanical exfoliation strategies in liquids and depend on the material to exfoliate[215]. For example, MoS_2 is most easily exfoliated using NMP or *N*-Cyclohexyl-2-pyrrolidone (CHP).[215]

Such mechanical exfoliation in liquid phase can even take place in pure water if heated enough to ensure the colloidal stabilization of the nanosheets.[222] The main drawback of mechanical exfoliation in liquid is generally the lack of dimension control of the exfoliated nanosheets: the dispersion does not contain monolayers only but a mixture of mono- and multilayers. Long exfoliation times can even lead to the formation of TMDCs "quantum dots" as exemplified for MoS_2, $MoSe_2$ WS_2, WSe_2, ReS_2, TaS_2 and $NbSe_2$.[223]

A widely used alternative to mechanical exfoliation is exfoliation through intercalation. Lamellar materials can act as hosts for a variety of small molecules (generally ions), which can penetrate into the space between layers. The interlayer space expands, destabilizing the structure and renders the exfoliation through sonication easy. In the case of TMDCs, intercalation is often associated with simultaneous reduction of the layers especially when the intercalation involves alkali metals such as lithium[224]. Such reduction can strongly modify the resulting monolayer properties. For example, in the case of MoS_2 and WS_2, a phase transition occurs during lithium exfoliation, induced by the charging of the layers. The resulting monolayers exhibit a 1T crystal structure (octahedral coordination for the metal) instead of the usual 2H structure (where the chalcogen atoms surrounding the metal adopt a triangular prismatic geometry). This charge and crystal structure change profoundly affects the electronic properties of the resulting monolayers, 2H-MS_2 are direct band gap semiconductors whereas 1T-MS_2 exhibit a metallic character. The widespread use of these exfoliation methods is hindered by the dangerousness of alkaline metals containing intercalants such as n-butyllithium. Alternative intercalants have been explored to increase the exfoliation yields and render these protocols safer and more cost effective.[225] It is also possible to perform electrochemical lithium intercalation to increase the yield and quality of the obtained nanosheets.[226] The exfoliation by intercalation technique is a method of choice to obtain a high yield of monolayers, at the expense of a crystal structure change induced by the intercalation itself. This structure change is reversible by gentle heating (between 200 and 300°C for example in the case of MoS_2).[227]

Nanosheets obtained through liquid phase exfoliation are generally colloidaly stable. In the case of mechanical liquid exfoliation, the stabilization is insured by interactions with the solvent itself, the concentration of stable dispersions is therefore limited and pretty low (a few hundreds of mg/L). On the other hand, for exfoliation through intercalation, the stability is generally induced by the surface charges generated by the intercalation process. One can then obtain highly concentrated dispersions of nanosheets in polar solvent such as water.[222]

Neither of these liquid phase exfoliation methods allows for a complete morphological control of the obtained nanosheets. The mechanical exfoliation produces a mixture of mono- and multilayers nanosheets, whereas intercalation driven exfoliation induces crystal structure

changes. Furthermore, none of these methods allow for a good control of the nanosheets lateral extension. These drawbacks have motivated the development of direct colloidal syntheses for the production of monolayered metal chalcogenides.

An alternative strategy combining advantages of both approaches has been recently developed as tandem molecular intercalation (TMI).[228] This strategy, tested on different TMDCs (TiS_2, ZrS_2 and NbS_2 obtained via colloidal synthesis and commercial powders of WSe_2, MoS_2 and TiS_2) consists of the intercalation of a mixture of short and long chains Lewis bases such as propyl-, butyl- and hexyl-amine or sodium ethoxide and sodium hexanolate. This exfoliation does not induce any crystal structure change of the monolayers but is more efficient for rather small (100nm) crystallites.

We will present in the following some successful strategies to directly synthesize colloidal stable lamellar metal chalcogenides nanosheets. A first part focuses on TMDCs, with emphasis on TiS_2 as a prototype of IVB and VB dichalcogenides, then on molybdenum and tungsten dichalcogenides. After the presentation of some transformations, manipulations and applications of TMDCs colloidal nanosheets, other lamellar chalcogenides systems will be discussed, such as IV-VI and V-VI chalcogenides.

5.2. Colloidal synthesis of transition metal dichalcogenides

5.2.1. Column IVB and VB chalcogenides

The first attempts to produce size-controlled colloidal TMDCs nanostructures where driven by the will to study the quantum confinement effects in these materials.[229] Due to small excitonic Bohr radius, confinement effects arise for very small lateral sizes and cluster syntheses were developed. Such clusters were mainly produced by reactions in inverse micelles. In a typical MoS_2 cluster synthesis,[230,231] $MoCl_4$ is dissolved in a degassed inverse micelle solution containing octane as a solvent, hexanol as a cosurfactant and tridodecylmethylammonium chloride as a surfactant. Clusters are immediately formed after H_2S injection, and control over the cluster size is possible by changing the nature of the surfactant. Colloidally stable cluster dispersions are monodisperse in size and exhibit strong confinement effects as evidenced by absorption spectra displaying well resolved excitonic features, strongly blue-shifted compared to the bulk spectrum. STM measurements of the clusters indicate that their thickness corresponds to one S-Mo-S trilayer only. Similar synthesis has been reported in details for WS_2[232], $MoSe_2$ and WSe_2[233], all of them reported as single trilayers, with sizes ranging from 2.5 to 8 nm diameter. Furthermore, some evidence has been given of an aggregative growth mechanism for MoS_2 clusters, unstable 4nm clusters

spontaneously evolve to form 8nm clusters over time.[234] TiS_2 clusters have also been synthesized using the same inverse micelle approach, the reported sizes range between 2 and 10 nm.[235]

Subsequently, different hydrothermal synthetic strategies have been described, giving generally access to TMDC nanosheets but without colloidal stability and control over size, shape or aggregation of the obtained nanostructures.[236–238] The nanosheets often self-assemble during synthesis to give flower like morphologies.[239] In the following we will mainly focus on organic-phase colloidal syntheses of TMDC nanosheets, which gives access to stable dispersions of nanostructures.

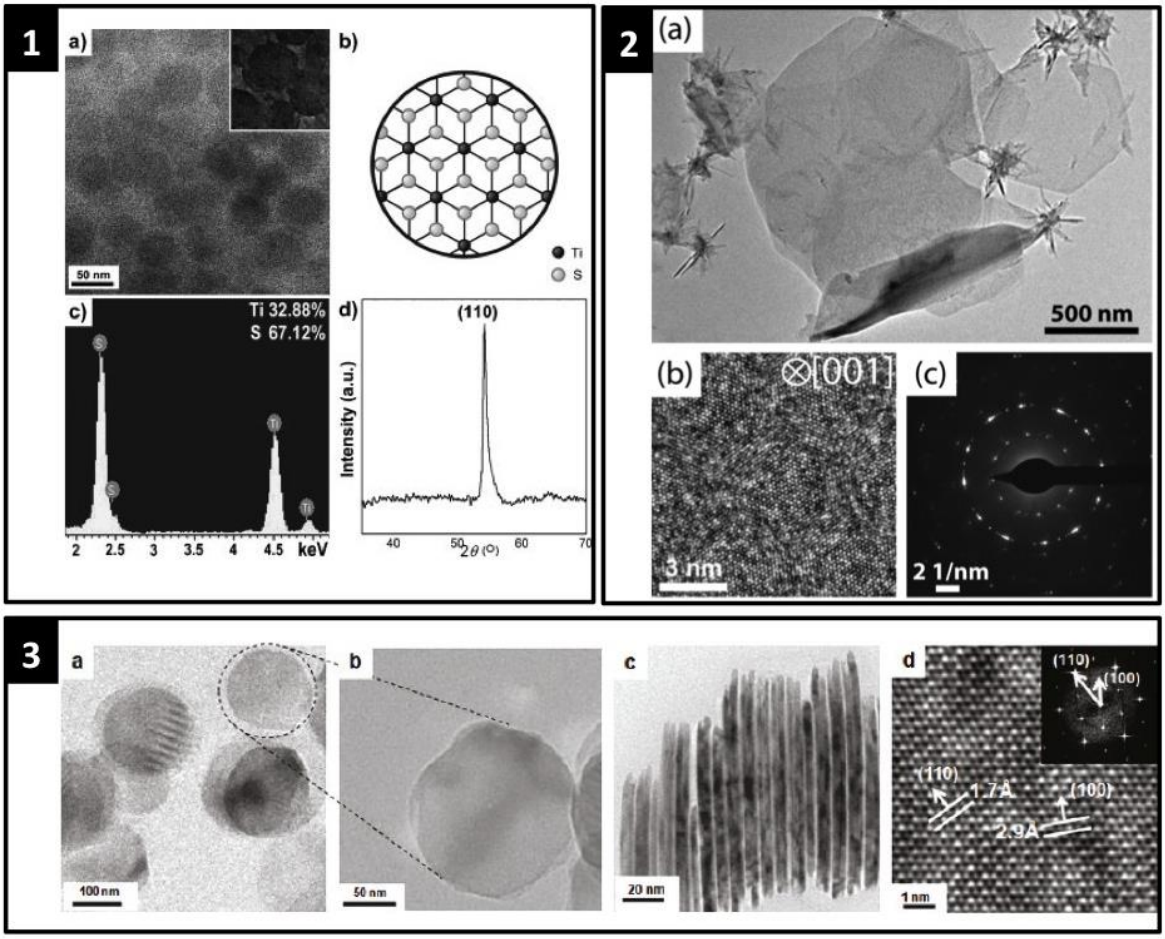

Figure 30: ***1****-(a) TEM image showing top view of 50-nm TiS_2 nanodisks, (b) structural diagram, (c) EDS spectrum, and d) PXRD pattern. From ref.*240*. Copyright 2008 by John Wiley & Sons, Inc. Reprinted by permission of John Wiley & Sons, Inc.* ***2****-(a) Low- and (b) high-resolution TEM images of TiS_2 NSs. (c) SAED pattern of TiS_2 NSs stacked atop each other. Adapted with permission from ref.*241*. Copyright (2012) American Chemical Society.* ***3****- TEM images of TiS_2 discs: (a, b) Low-resolution and magnified images of TiS_2 disc nanocrystals (c) Side view of TiS_2 discs stacked together. (d) HRTEM image and (inset) FFT pattern of TiS_2. Adapted with permission from ref.*242*. Copyright (2011) American Chemical Society.*

Direct colloidal synthesis of larger TiS_2 monolayers has been first reported in 2008, and consists this time in a heating-up process.[240] $TiCl_4$ is dissolved in dried oleylamine by sonication. A sulfur/oleylamine precursor is prepared by dissolving sulfur powder into oleylamine at 110°C. Both precursor solutions are then mixed at room temperature, heated-up to 215°C, and reacted for 12 hours, leading to 50nm diameter TiS_2 monolayer nanodiscs (Figure 31-1). Changing the sulfur stoichiometry and the reaction time allows for a lateral size control from 18 to 50nm diameter. The obtained monolayers have been reported to be unstable, and undergo rapid oxidation when exposed to air.

Syntheses carried out using the same precursors (sulfur and titanium tetrachloride) but using 1-octadecene as the solvent[243] lead to the formation of flower-like or flake-like nanostructures, consisting of numerous randomly oriented aggregated nanosheets. Subsequent reported syntheses are mainly based on the use of oleylamine both as solvent and stabilizing ligand. The morphology of the obtained nanosheets depends on the experimental conditions: nature of the sulfur precursor, type of synthesis (mainly heating-up process or hot injection protocol), working temperature and annealing time. Obtaining well-defined morphologies and preventing aggregation in solution during growth has been the focus of subsequent studies. For example, a simple protocol modification reported by Kuno *et al.*[241] allowed them to synthesize much larger TiS_2 nanosheets, with average lateral dimensions of 500 nm × 500 nm and thicknesses between 4 and 6 nm (Figure 31-2). The synthesis consisted in dissolving a slight molar excess of elemental sulfur in oleylamine, followed by the introduction of $TiCl_4$ at room temperature and heating up the mixture at 300°C for 3 h. By changing the sulfur precursor to carbon disulfide (CS_2) and using a hot-injection protocol at 300°C (directly injecting CS_2 into a mixture of titanium(IV) chloride and oleylamine), Cheon group reported the formation of well-defined TiS_2 colloidal nanodiscs[242]. These nanocrystals are about 100nm diameter and a few monolayers in thickness (4 to 6 nm, Figure 31-3).

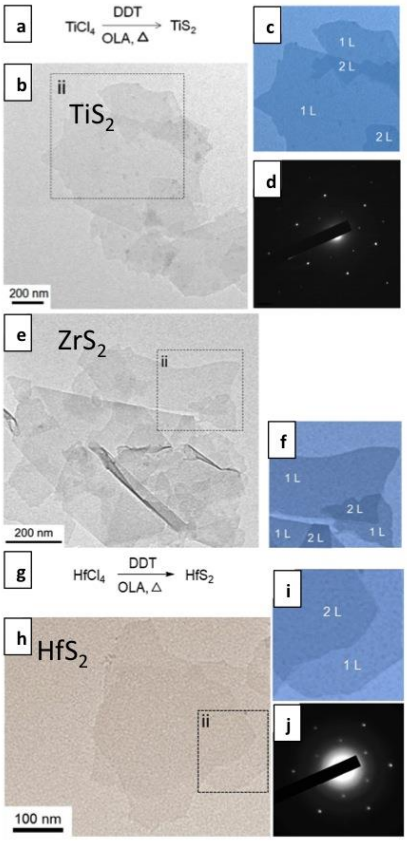

*Figure 31: Single-layer TiS_2, ZrS_2 or HfS_2 nanosheets (a) Single-layer TiS_2 nanosheets formed by using DDT. (b) Low- magnification TEM image; (c) pseudocolor image for a selected area; (d) SAED pattern of a single-layer TiS_2 nanosheet. (e) TEM image of the single-layer ZrS_2 nanosheets; (f) pseudocolor image of a small area. (g) Chemical reaction for HfS_2. (h) TEM image; (i) pseudocolor image for a selected area; and (j) SAED pattern. Adapted with permission from ref.*244*. Copyright (2014) American Chemical Society.*

The same group used a simillar colloidal synthesis strategy to explore the preparation of colloidal nanodiscs made of diverse transition metal sulfides and selenides from the IVB and VB columns: TiS_2, ZrS_2, HfS_2, VS_2, NbS_2, TaS_2 and $TiSe_2$, $ZrSe_3$, $HfSe_3$, VSe_2, $NbSe_2$, and $TaSe_2$.[245,246] Sulfides where systematically prepared using a hot injection protocol with carbon disulfide as the sulfur precursor whereas selenides are synthetized via a heating up process using elemental selenium as the selenide precursor. They also demonstrate that the use of elemental sulfur dissolved in oleylamine is a poor sulfide precursor for the formation of high quality nanodiscs as its reaction pathway generates reactive radicals degrading the crystal structure of the already formed nanodiscs.

Cheon and coworkers suggest still another sulfur precursor change and a modification of protocol from fast hot-injection to slow introduction or generation of the sulfide

precursor.[244] The strategy here is to suppress the nucleation burst, which leads to multilayers nuclei and small nanodiscs. The so-called "diluted chalcogen continuous influx (DCCI)" has been demonstrated efficient for the synthesis of group IVB TMDCs monolayers (ZrS_2, TiS_2 and HfS_2, Figure 32). In a typical synthesis, a mixture of metal chloride, oleylamine and dodecanethiol (DDT) is heated between 230°C and 245°C for prolonged amount of time (about 10 hours). At these temperatures, the DDT slowly decomposes to release hydrogen disulfide (H_2S) during the whole synthesis time. The absence of a strong increase in sulfide precursors at the beginning of the synthesis prevents the fast nucleation of multilayers. At the same time, the small number of generated nuclei allows for the formation of large monolayer nanosheets, between 500nm and 1µm.

5.2.2. Column VIB chalcogenides, molybdenum and tungsten compounds.

We can retrace the same evolution in synthesis strategies for molybdenum and tungsten dichalcogenides. A first successful approach by Cheon and coworkers has been to sufidize WO_3 nanorods[247]. The solvent is here hexadecylamine and the sulfidation is carried out by fast injection of CS_2 at 330°C and annealing for 1 hour. This first synthesis produces bundles of WS_2 nanosheets where the lateral dimensions are controlled by the initial length of the WO_3 nanorods used as the tungsten source. A simpler one-pot strategy has also been reported for MoS_2 and WS_2, based on high-temperature decomposition of single source precursors in oleylamine at 360°C.[248] The authors used $(NH_4)_2MoS_4$ and $(NH_4)_2WS_4$ as precursors for MoS_2 and WS_2 nanosheets respectively. This synthetic scheme does not produce well-defined freestanding monolayers and the reaction products look slightly aggregated. Synthesis of colloidaly-stable WSe_2 nanosheets was reported by Brutchey and coworkers for the preparation of conductive thin-films. The synthesis was carried out by the injection of di-tert-butyl diselenide (tBu_2Se_2) into a solution of WCl_4 in dodecylamine at 150 °C under nitrogen. The solution was then heated to 225 °C and held at this temperature for 6 h prior to quenching. In this case, the generated products are diverse in shape. TEM images show the presence of nanosheets, onion structures and aligned plates.[249]

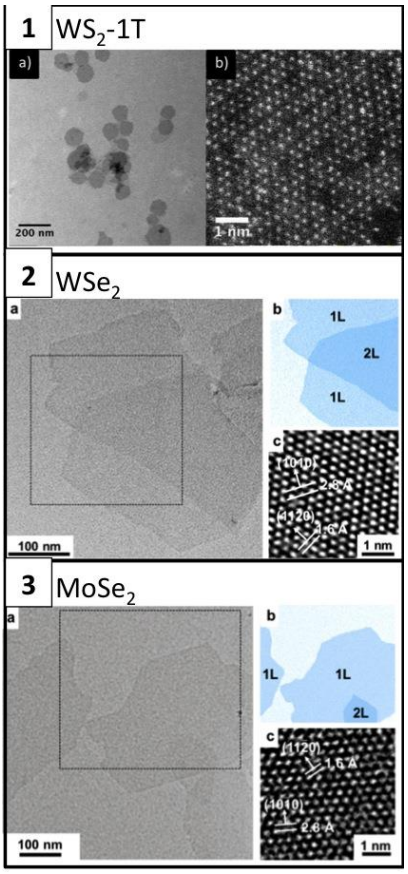

*Figure 32: Colloidal tungsten and molybdenum dichalcogenides monolayers. 1- (a) Low-magnification TEM image of 1T-WS_2 nanosheets. (b) HAADF-HRSTEM image of a 1T-WS_2 monolayer, showing the zigzag pattern of the tungsten atoms characteristic of the distorted 1T structure as well as numerous voids and tungsten vacancies. Adapted with permission from ref.*250*. Copyright (2014) American Chemical Society. 2- Single-layer WSe_2 nanosheets. (a) Low-magnification TEM image and (b) pseudocolor image of the selected area in the box of panel a. (c) High-resolution TEM image, of a single-layer WSe_2 nanosheet. Adapted with permission from ref.*251*. Copyright (2015) American Chemical Society. 3- Single-layer $MoSe_2$ nanosheets. (a) Low-magnification TEM image and (b) pseudocolor image of the selected area in the box of panel a. (c) High-resolution TEM image, of a single-layer $MoSe_2$ nanosheet. Adapted with permission from ref.*251*. Copyright (2015) American Chemical Society.*

The first controlled colloidal syntheses of molybdenum and tungsten dichalcogenides monolayers appeared only recently. In 2014, Mahler *et al.* reported the preparation of 1T-WS_2 monolayers ranging from 20 to 100nm (Figure 33-1). The strategy is based on continuous injection of the precursors in hot oleylamine (320°C). A precursor solution made of a mixture of oleylamine, oleic acid, WCl_5, and CS_2 is slowly injected in hot oleylamine at 320°C for 30 minutes. Here again, the slow introduction of precursors helps to avoid the formation of multilayers. Interestingly, the crystal structure of the nanosheets can be tuned during the synthesis by addition of hexamethyldisilazane (HMDS), inducing the formation of flower-like

2H-WS_2 nanostructures, but at the expense of the monolayer shape. Another strategy to obtain colloidal molybdenum and tungsten diselenide monolayers has been devised by Jung *et al*. in 2015.[251] This time, instead of playing with the precursors introduction to control the nucleation and growth events -then the production of monolayers- they explored the influence of the solvent (acting also as a ligand) on the morphologies of nanocrystalline WSe_2. They systematically changed the solvent in a one-pot reaction where $W(CO)_6$ is reacted with diphenyl diselenide (Ph_2Se_2) in oleylamine, oleyl alcohol, or oleic acid (ligands having the same number of carbon atoms, but different terminal functional groups) at 330 °C under an Ar atmosphere for 12 h. Nanostructures obtained in oleylamine are small (5nm) multilayer (4-8 layers) nanosheets. The products obtained in oleyl alcohol are thinner (2-3 monolayers) and larger (20nm). Finally, when oleic acid is used as solvent and ligand, the nanosheets obtained are monolayers with large lateral sizes of 200-400nm (Figure 33-2 and 33-3). The proposed explanation is based on DFT calculations showing that primary amines strongly bound to the edges of the nanostructures, thus favoring the multilayer growth. On the other side, oleic acid is a weak ligand favoring lateral growth and the formation of monolayers. A close protocol, using dibenzyl diselenide and Bis(acetylacetonato)dioxomolybdenum(VI) ($MoO_2(acac)_2$) as precursors with oleylamine as the solvent, yields $MoSe_2$ hierarchical nanostructures after only 20 minutes of reaction at 240°C. [252]

Even if the exact formation mechanism to obtain colloidal TMDC monolayers is still unclear, it is possible to perceive some general guidelines. The protocols developed so far seek first to control the nucleation rate to avoid the formation of multilayers. This is achieved either by the slow injection of the precursors into the reaction mixture or the use of slowly decomposing precursors inducing a controlled release of active species over time. A second important parameter is the nature of the solvent, always coordinating the formed nanosheets to prevent aggregation during synthesis. It is then possible to favor the lateral growth through the use of suitable ligands selectively binding to the basal planes while keeping the edges available for the growth reaction. The colloidal synthesis of lamellar metal chalcogenide nanosheets is still in its infancy, numerous structures and materials have been exfoliated but not directly synthetized among the about sixty layered TMDC identified by Yoffe.[253]

5.3. Transformations and applications

Colloidal TMDCs nanodiscs and nanosheets can act as building blocks to develop more complex architectures or directly find diverse technological applications. Physical properties of two-dimensional nanosheets can be tuned by a variety of different ways. In the case of substrate grown monolayers, alloying[254], doping[255], or formation of in-plane

heterostructures[256] have been demonstrated. Through colloidal synthesis, still other types of heterostructures are now accessible.[79]

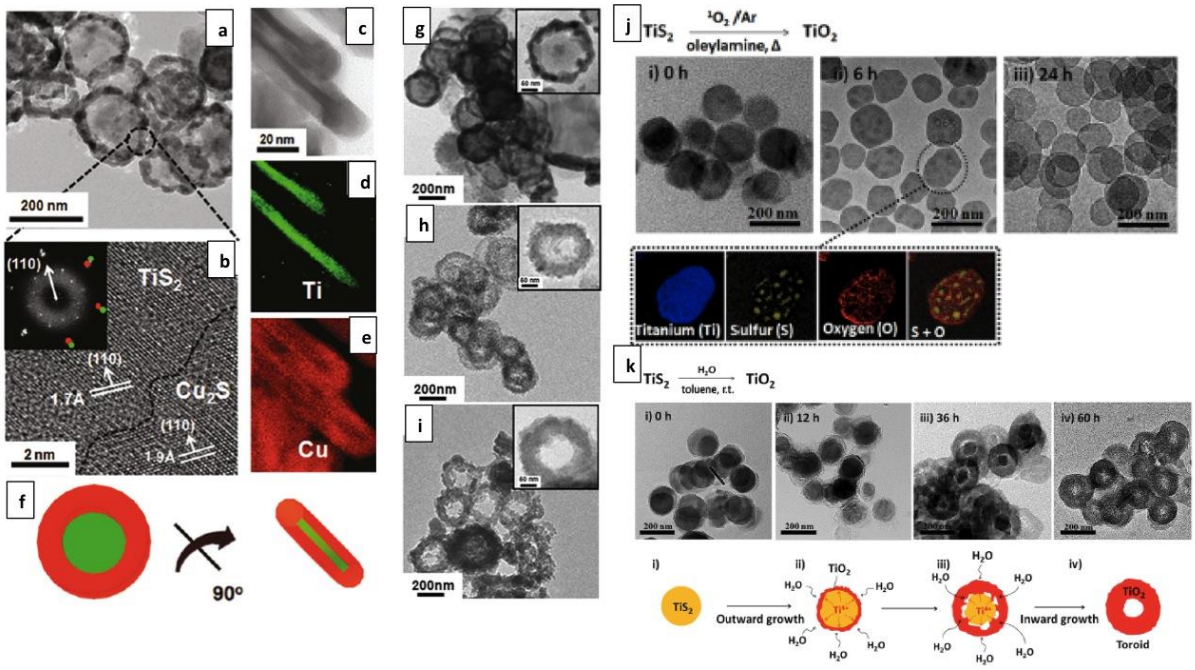

*Figure 33: a) Large-area image of an intermediate TiS_2_Cu_2S structure obtained with $CuCl_2/TiS_2$ = 1. (b) High-magnification image at the interface between TiS_2 and Cu_2S showing orientation match between of Cu_2S and TiS_2 crystal structures. The FFT pattern (inset) shows green and red dots corresponding to TiS_2 and Cu_2S, respectively. (c) Side-view TEM image and EELS elemental analysis (d, e) of an intermediate TiS_2_Cu_2S structure. Ti is shown in green and Cu in red. (f) Schematic rotation of the intermediate structure by 90°, showing both planar and side-view images. TEM images of toroidal-shaped nanostructures synthesized by reactions of TiS_2 discs with Ag, Mn, and Cd cations: (g) TiS_2_Ag_2S; (h) TiS_2_MnS; (i) TiS_2_CdS. The insets show higher-magnification images. Adapted with permission from ref.*242*. Copyright (2011) American Chemical Society. j) Reaction of TiS_2 upon $1O_2$ as chemical stimulus: TEM images of TiS_2 nanocrystals treated with $^1O_2$ for (i) 0 h, (ii) 6 h and (iii) 24 h. Dark contrast dots appear in (ii), EELS analysis of nanocrystals collected at 6 h (Ti, blue; S, yellow; O, red) shows sulfur containing dots (TiS_2) surrounded by oxygen (TiO_2). k) Disc to toroid TiO_2 morphological transformation driven by H_2O. TEM images at each transformation stage from TiS_2 nanodiscs to toroid TiO_2 nanocrystals by reacting TiS_2 with H_2O for (i) 0 h, (ii) 12 h, (iii) 36 h and (iv) 60 h. Adapted with permission from ref.*257*. Copyright (2013) American Chemical Society.*

Using a model system based on colloidal TiS_2 nanodisks, Cheon and coworkers have explored diverse cation or anion exchange reactions, leading to different heterostructures. In a first paper,[242] they reported the reaction of TiS_2 nanosheets with copper (II) cations. The cations react preferentially at the edges of the nanodisks, leading to the formation of TiS_2_Cu_2S heterostructures and then to pure Cu_2S toroidal nanocrystals if the reaction is complete (Figure 34 a-f). Such metallic cation reaction on TiS_2 edges is broadly applicable and allows the formation of TiS_2/Ag_2S, TiS_2/MnS and TiS_2/CdS heterostructures (Figure 34 g, h, i).

These first experiments demonstrate the particular reactivity of the edges compared to the basal planes in the case of two-dimensional lamellar dichalcogenides.

Such 2D-heterostructure synthesis via exchange of one of the elements of the dichalcogenide nanodisk can also be carried out with modification of the anion, in this case replacement of the sulfur by oxygen.[257] Depending on the oxygen source and the experimental conditions, the sulfur can be fully replaced by oxygen with conservation of the initial nanostructure morphology, leading to the formation of pure TiO_2 nanodisks (Figure 34 j). In this case, the reaction is induced by bubbling oxygen gas into a hot oleylamine mixture (140°C) containing the TiS_2 nanodisks. The working temperature generates the reactive $^1O_2$ species. On the other hand, when TiS_2 nanodisks (5mg) are mixed with water (0.3mL) in toluene (3mL) at room temperature for time ranging from 12 to 60 hours, TiO_2 gradually appears on the edges, ultimately forming pure TiO_2 toroidal nanocrystals and completely consuming the initial TiS_2 nanodisks(Figure 34 k).

Reactivity of TMDC nanosheets towards metal salts can be also used to generate numerous metal/TMDC nanosheets heterostructures. A simple route consists in mixing nanosheets, metal salts and a reducing agent, as demonstrated for the formation of MoS_2 or $MoSe_2$ nanosheets decorated with Au, Ag or Pt nanoparticles.[258] The reduction of the metal salt can be induced using chemical, microwave or thermal routes for example.[259] The noble metal decoration of TMDCs nanosheets has been demonstrated down to the monolayer. Chemically exfoliated MoS_2 can be decorated with Pd, Pt or Ag nanostructures using different reducing agents and surfactants depending on the metal deposited.[260] Gold nanoparticles can also be grown on chemically exfoliated monolayers without the use of any reducing agents, simply by mixing a water dispersion of MoS_2 or WS_2 monolayers with $HAuCl_4$ solution in water.[261] This spontaneous gold reduction can be induced by the negatively charged nature of the chemically exfoliated monolayers. Alternatively, the TMDC nanosheets themselves can act as the reducing agents, allowing spontaneous gold reduction at the surface of the layers, even for the mechanically exfoliated 2H-MoS_2 nanosheets.[262] A mechanism involving the oxidation of the molybdenum or tungsten atoms from +IV to +VI has been proposed in the case of WS_2 nanotubes and fullerene-like MoS_2.[263] Metal deposition on TMDCs monolayers can be controlled by a careful choice of the reducing agents, capping molecules and nature of both the nanosheet and the metal itself to induce an epitaxial growth of the metallic structure on top of the monolayer.[260] More complex phenomena have been recently observed on these TMDC/metal systems, leading to the formation of gold nanowires on MoS_2 surfaces[264], or to the synthesis of TMDC hybrid nanobelts (MoS_2, TaS_2, TiS_2, WSe_2 or $TaSe_2$) decorated with Pt or PtAg alloy nanoparticles.[265] Dedicated reviews discuss in more details the synthesis of TMDC/metal heterostructures[266] and the formation of composites including nanosheets.[267] [268]

It is worth mentioning an alternative strategy to prepare TMDC-containing heterostructures where the two components are synthetized at the same time. Using a "one-pot" synthesis, Zhang and coworkers successfully synthetized MoS_2/CdS and WS_2/CdS nanocrystals containing one TMDC monolayer on the (0001) surface of the wurtzite CdS nanocrystals.[269] The protocol consists in the injection of $(NH_4)_2WS_4$ oleylamine precursor solution into a hot mixture of ODE, oleylamine, oleic acid and cadmium oxide. $(NH_4)_2WS_4$ serves both as the tungsten and sulfur precursor.

5.3.1. Manipulations

The development of colloidal TMDCs nanosheets applications implies to master their manipulation: assembly, orientation, organization and thin film deposition for example. Some techniques have then been developed to specifically deal with colloidal nanosheets.

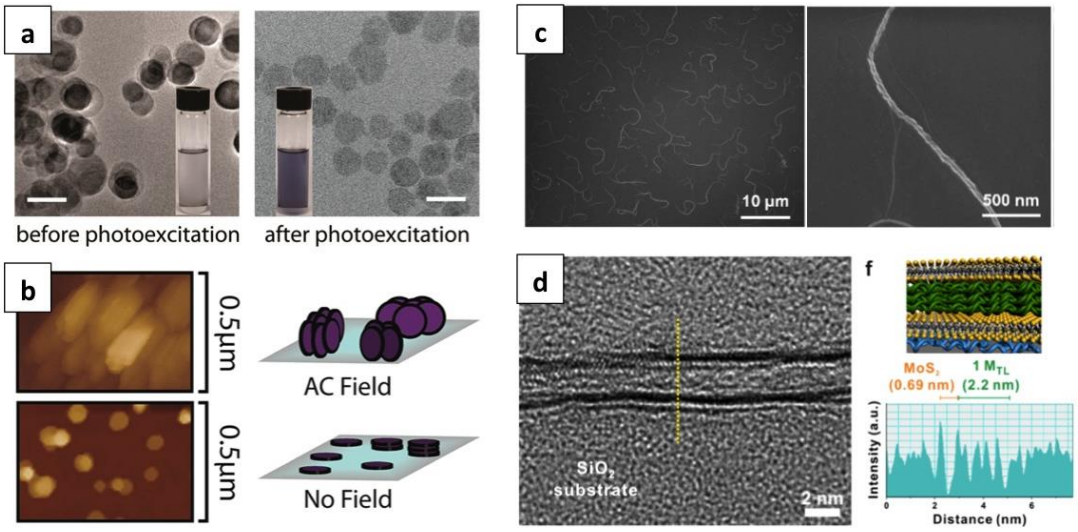

*Figure 34: a) TEM image of a TiS_2 sample before and after 30 min of photoexcitation under pulsed laser irradiation. The scale bar is 200 nm. Reprinted with permission from ref.*270*. Copyright (2014) American Chemical Society. b) AFM images of TiS_2 nanodiscs deposited on a microscope coverslip in the presence (top) and the absence (bottom) of a 2 kHz square wave E_z field. Reprinted with permission from ref.*271*. Copyright (2015) American Chemical Society. c) SEM images of chiral MoS_2 nanofibers. Reprinted with permission from ref.*272*. Copyright (2015) American Chemical Society. d) A representative cross-sectional TEM image of 2 MoS_2/polymer multilayer with the corresponding line scan profile representing the thickness of a single MoS_2 nanosheet and single polymeric trilayer (M_{TL}) of the MoS_2/polymer. Reprinted with permission from ref.*273*. Copyright (2014) American Chemical Society.*

Using solution-synthetized colloidal TiS_2 nanodiscs as a model system, Cheon and coworkers reported two interesting phenomena. After synthesis, dispersions of TIS_2 nanodiscs have a tendency to vertically stack in solution -forming aggregates- due to strong interactions between the basal planes. Under pulsed photoexcitation at high enough power to transiently

modify the charge carrier distribution of the nanodiscs, the stacks disaggregate, forming stable dispersions of individual particles if the solvent is polar enough to stabilize them (Figure 35 a). These light-induced dispersions are stable over time and the vertical stacks can be created again via a decrease of the solvent polarity.[270] The same TiS_2 nanodiscs can also be vertically oriented on a surface using electric fields (Figure 35 b). Contrarily to other anisotropic nanocrystals such as nanorods, applying a continuous electric field does not result in orientation control of the nanodiscs in solution. The problem is circumvented by applying a DC square-wave electric field, the orientation occurs during the changes in intensity. [271]

The charged nature of lithium-exfoliated nanosheets also gives access to electrostatic assembly strategies. For example, a layer-by-layer assembly strategy has been demonstrated using negatively charged MoS_2 nanosheets and a polyelectrolyte (in this case poly(allylamine hydrochloride), PAH), allowing for the formation of MoS_2/PAH multilayers on a substrate (Figure 35 d). After annealing and 2H crystal structure restoration, the multilayers MoS_2/polyelectrolyte exhibit characteristic monolayer fluorescence, highlighting the successful electronic decoupling of the sheets by the polymer spacing.[273]

Self-assembly can also be used to create complex structures in solution. It is for example possible to synthesize chiral nanofibers from exfoliated TMDC nanosheets in solution (Figure 35 c).[272] The structuration is induced in this case by strong stirring of a nanosheets solution (1500rpm) and stabilized by the presence of a non-ionic surfactant such as Pluronic P123, Triton X-100 or Tween 20.

Finally, stable dispersions of nanosheets can also directly be used as ink to prepare functional electronic devices.[274] Different ways of deposition have been explored, such as drop-casting, inkjet printing or vacuum filtration, all of them leading to working devices.[274]

5.3.2. Functionalization

TMDCs have the unique property to form stable colloidal suspensions after exfoliation even without the use of any stabilizing agents such as surface ligands.[215] Being able to functionalize them with organic molecules can further increase their stability and add new functionalities to the nanosheets. The approach is different than for colloidal II-VI quantum dots, where the synthesis is carried out in presence of organic ligands. They remain at the surface of the nanocrystals, where they can be exchanged in a subsequent step.[275] In the case of TMDCs nanosheets,[276] as ligands interactions are weak on the basal planes of the sheets, the functionalization takes place only on defects and edges, or is mediated by a chemical transformation of the sheet itself to render it more reactive (under the charged 1T structure for example). The following ligand-functionalization techniques have been developed mainly

for molybdenum and tungsten disulfides but could be applied on other TMDCs nanosheets as well. They often involve first a chemical exfoliation step using lithium intercalation, inducing charging and structure change of the exfoliated monolayers.

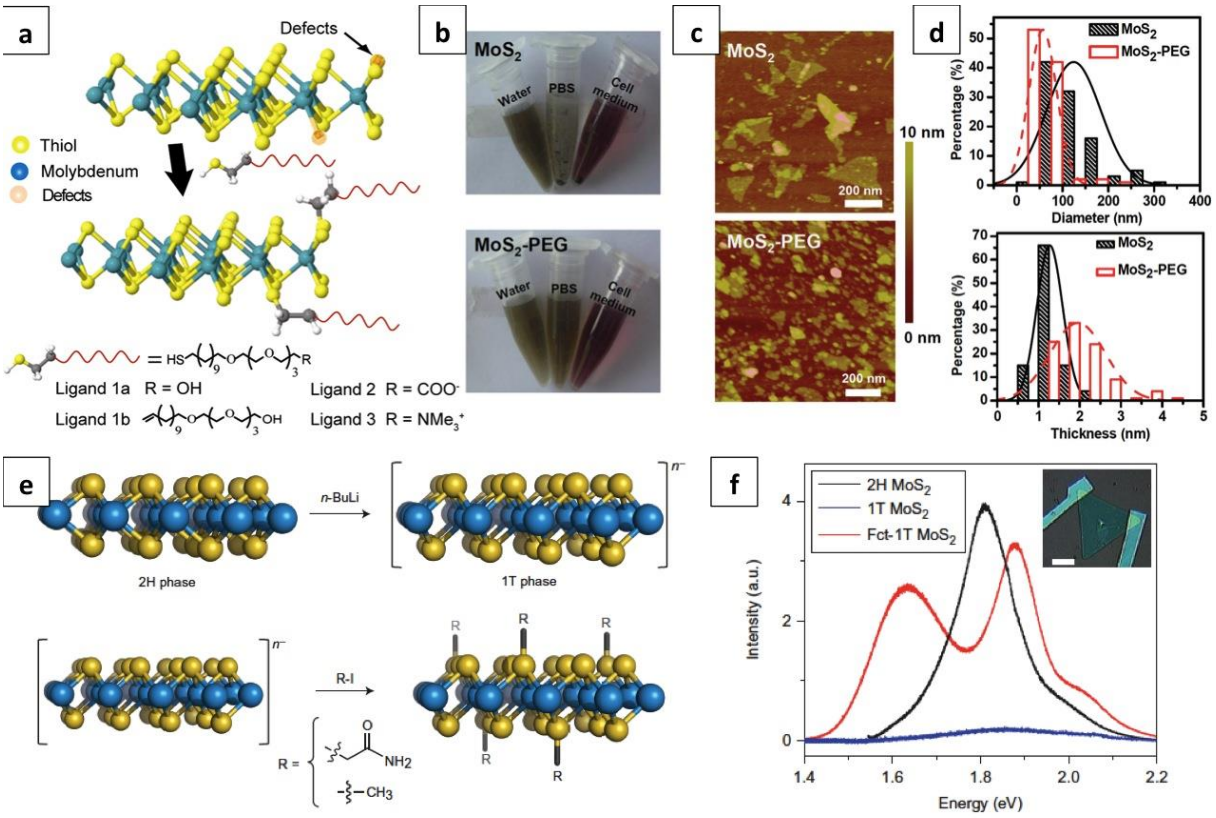

*Figure 35: a) Structural model illustrating thiol conjugation of chemically exfoliated MoS_2 sheets. Reprinted with permission from ref.*277*. Copyright (2013) American Chemical Society. b) Photos of MoS_2 and MoS_2-PEG in water, PBS and cell medium after 3,000 rpm centrifugation. c) AFM images of MoS_2 before and after PEGylation. d) AFM-measured diameter and thickness distributions of MoS_2 and MoS_2-PEG. From ref.*278 *Copyright 2014 by John Wiley & Sons, Inc. Reprinted by permission of John Wiley & Sons, Inc. e) Schematic of covalent functionalization: The 2H phase of TMDs is converted to the 1T phase via lithiation using butyllithium (BuLi), the nanosheets are then functionalized using 2-iodoacetamide or iodomethane (R-I) solution. f) Photoluminescence spectra obtained from single-layer MoS_2 grown by CVD (2H phase), from the metallic 1T phase and from the functionalized 1T phase. A strong photoluminescence peak at ≈1.8 eV is observed for the 2H phase, consistent with single-layer 2H MoS_2, whereas photoluminescence is quenched after conversion to the metallic 1T phase. The functionalized 1T phase exhibits strong photoluminescence, characterized by two bands at ≈1.9 eV and ≈1.6 eV. Inset: typical CVD-grown monolayer triangular nanosheet on which the photoluminescence spectra were measured. Scale bar, 25 µm. Reprinted by permission from Macmillan Publishers Ltd: Nature Chemistry from ref.*279*, copyright (2014).*

A first successful ligand conjugation protocol has been developed by Dravid group, using chemically exfoliated MoS_2 monolayers (Figure 35a-d).[277] Different water-soluble pegylated thiols (dissolved in water or methanol depending their structure) are simply shaken and/or sonicated with the purified exfoliated MoS_2 monolayers for 24 hours. After purification by dialysis or centrifugation, the conjugated nanosheets exhibit ζ-potential change consistent with the ligand charge. The presence of ligands anchored on the nanosheets is also evidenced by FT-IR spectra showing characteristic ligands vibrations. Finally, strong differences in electrochemical hydrogen evolution reaction (HER) efficiency suggest that the ligands are bound on the edges sites, efficiently passivating them.

A second approach, developed by Voiry *et al.* is based on covalent functionalization.[279] The authors exploit the electron rich nature of the 1T phase (MoS_2, WS_2 or $MoSe_2$) to make it react with various electrophiles such as iodomethane, 2-iodoacetamide or aryl diazonium salts (in this case, 4-bromobenzenediazonium tetrafluoroborate, see Figure 35 e). A typical procedure consists of mixing an aqueous solution of purified lithium exfoliated TMDC nanosheets with 2-iodoacetamide in tenfold excess and let it react for 5 days at room temperature. The successful functionalization is characterized by XPS, FTIR and C-NM, highlighting the addition of amide or methyl moieties directly on the chalcogen layer. Surprisingly, the functionalized monolayers keep a 1T structure but evolve from metallic to semiconducting, exhibiting a strong photoluminescence (Figure 35 f). The covalent functionalization of the 1T phase can at the same time stabilize the structure and tune the electronic properties of the monolayers.[280]

Alternatively, it is possible to directly functionalize 2H-MoS_2 nanosheets through metal salts coordination.[281] This strategy, initially reported for inorganic MoS_2 fullerenes functionalization[282] is based on the use of a transition metal cation with high affinity for sulfur and octahedral coordination, coupled with a strong chelating ligand. The metal cation strongly binds to the TMDC surface and act as an anchor for organic chelating ligands. For example, copper (II) acetate can be adsorbed on MoS_2 surfaces with a degree of functionalization as high as 50%. This adsorption is reversible and does not induce structural changes in the nanosheets structure.

Among the different exposed functionalization strategies, thiol conjugation is playing a particularly important role in the development of biomedical applications using nanosheets.[25] Employing dithiols as binding group (such as lipoic acid-PEG molecules) increases the affinity of the ligand for the nanosheet surface.[278] Thanks to their broad light absorption in the visible and near-infrared regions of the spectrum, TMDC nanosheets have been first used as photothermal therapy agents.[283,284] Further studies have also demonstrated their potential as drugs delivery agents,[285,286] using their large surface area to load active

molecules. Using direct synthesis pathways, metal-doped WS_2 have been prepared to combine magnetic resonance imaging (contrast from the dopant) with X-ray imaging (high Z-elements forming the nanosheet).[287] Furthermore, single TMDC nanosheets exhibit different affinities for single and double-strand DNAs and efficiently quench the fluorescence of organic molecules, making them promising platforms for sensing of DNA and biomolecules.[288–290] Biomedical applications of TMDC nanosheets are described in details in recent reviews.[25,291]

The large surface area of TMDC nanosheets render them particularly attractive for diverse energy related applications. In catalysis, molybdenum and tungsten dichalcogenides have been demonstrated to be highly efficient electrocatalysts for hydrogen evolution reaction. Active sites being located on the edges,[292] it is beneficial to work with small dimensions or disordered nanostructures.[293] Alternatively, the activity of the catalyst can be increased by phase engineering, the metallic 1T phase being more active in the case of MoS_2[213] and WS_2[212] nanosheets for hydrogen evolution. Different reviews deal in details with the use of TMDC nanosheets for hydrogen evolution reactions[294] or more generally for light-harvesting applications.[295] The large surface-on-volume ratio of colloidal nanosheets makes then also particularly promising for the development new energy storage materials. Colloidal WS_2[247] and TiS_2[296] nanosheets, obtained through direct colloidal syntheses have been studied as electrode materials for electrochemical storage through lithium intercalation. Both materials behave differently than their bulk counterparts with a much higher storage capacity. Similarly, chemically exfoliated 1T-MoS_2 monolayers exhibit high volumetric capacitance of ≈700 F cm^{-3}, 20 times higher than the 2H crystal structure modification.[297] These promising results are generating a growing interest for the use of TMDC nanosheets in energy storing devices.[298,299]

5.4. IV-VI lamellar chalcogenides

IV-VI semiconductors, such as tin or germanium sulfides and selenides can also crystallize into lamellar systems. Depending on their stoichiometry, they either adopt a Typical TMDC structure for SnS_2 and $SnSe_2$, crystallizing into a CdI_2-type structure, whereas the mono-sulfides and selenides (GeS, GeSe, SnS and SnSe) crystallize into an orthorhombic structure as described in Figure 10.

SnS_2 single layers can be prepared through chemical exfoliation in liquid formamide.[300] Hexagonal nanoplates (lateral dimensions of 150nm and mean thickness of 16nm) have been synthetized similarly to other TMDC colloidal nanosheets, employing thermal decomposition of tin(IV) diethyldithiocarbamate $Sn(S_2CNEt_2)_4$ in oleylamine at elevated temperature

(280°C).[301] Such SnS_2 nanoplates can be also synthesized through hydrothermal[302] or solvothermal[303] protocols, with equally good results. The colloidal synthesis of tin diselenide ($SnSe_2$) nanosheets has been comparatively less explored, protocols yielding phase pure nanosheets have been developed, mainly through solvothermal reactions. For example, reaction of $SnCl_2$ and SeO_2 in benzyl alcohol and PVP (polyvinylpyrrolidone) in an autoclave at 180°C for 16h yields hexagonal nanosheets of 1 micron diameter which are only 6 nm thick.[304] One of the problems of the successful development of such nanosheets is the possible existence of mixed phases SnSe-$SnSe_2$.[305]

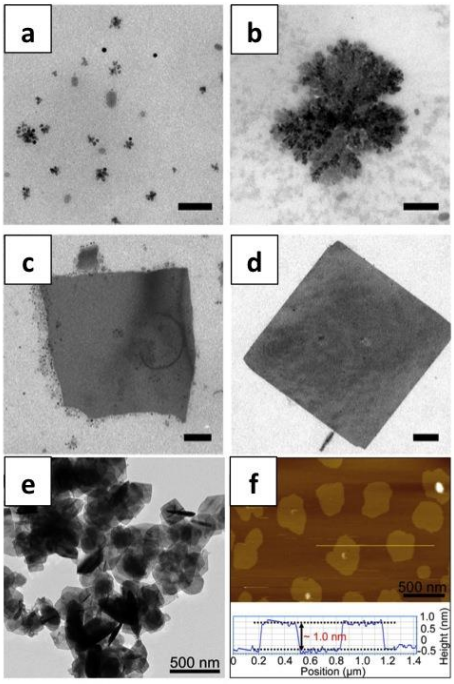

*Figure 36: (a-d) TEM images of aliquots taken during the formation of the SnSe nanosheets highlighting the different growth stages, from initial nucleation, agglomeration, and coalescence of nanoparticle seeds into two-dimensional dendritic nanostructures then lateral growth via nanoparticle attachment resulting in a uniform square-like nanosheet morphology. Scale bars are 100 nm. Reprinted with permission from ref.*306*. Copyright (2011) American Chemical Society. (e, f) TEM and AFM images of SnSe nanosheets with their height data, showing the successful synthesis of uniform single layer SnSe nanosheets. Reprinted with permission from ref.*307*. Copyright (2013) American Chemical Society.*

Both germanium and tin monochalcogenides nanosheets have been prepared using solvothermal approaches. Colloidal nanosheets of GeS and GeSe have been synthesized using a “one-pot” protocol, where a mixture of GeI_4, hexamethyldisilazane, oleylamine, oleic acid, and dodecanethiol (for GeS) or trioctylphosphine selenide (TOP-Se, for GeSe) are heated to 320 °C for 24 h.[308] The obtained nanosheets have lateral dimensions up to a few microns with thicknesses ranging from 3 to 100nm (about 5nm for GeS and more than 20nm for GeSe).

Similarly, SnSe nanosheets have been synthesized via a “one-pot” procedure, slowly heating a mixture of $SnCl_2$, oleylamine, TOP-Se, and HMDS to 240 °C and holding for 30 min.[306] In this case, square-like nanosheets are obtained (see Figure 36 d) with lateral dimensions of about 400nm and thicknesses ranging from 35 to less than 10 nm, depending on the amount of Sn and Se precursors used. This protocol allowed the authors to study the formation mechanism of these SnSe nanosheets: the formation occurs via coalescence of individual nanoparticle building blocks to yield a single-crystal nanosheet (Figure 36 a-d). If enough precursors are available, thickness growth takes place through coalescence of nanoparticles at the surface of the existing nanosheet. The same material can be colloidally synthesized with a controlled thickness down to the monolayer, still using a “one-pot” heating-up reaction. [307] In a typical procedure, a mixture of $SnCl_4 \cdot 5H_2O$, SeO_2, oleylamine, and 1,10-phenanthroline is degassed, heated up to 260 °C and annealed for 30 min under N_2 atmosphere. AFM measurements of the obtained nanosheets confirm their monolayer thickness of about 1nm (Figure 36 e-f)). It is worth noting that, without phenanthroline, 3D SnSe nanoflowers are obtained using the same procedure. In this case, the phenanthroline acts as a strong complexing agent, suppressing vertical growth and aggregation of thicker nanosheets arising during the synthesis of the nanoflowers. The formation mechanism investigation reveals again that an oriented attachment process leads to the nanosheets formation. The same group also reported the colloidal synthesis of SnS and SnS_2 nanosheets using tin diethyldithiocarbamate phenanthroline complexes.[309] Similarly to tin selenide system, tin sulfide nanocrystals and nanosheets can be either obtained under the SnS or SnS_2 stoechiometry, depending on the experimental conditions used.[310] Alternatively, SnS have been recently exfoliated using a liquid phase exfoliation protocol with N-methyl-2-pyrrolidone as a solvent.[311]

5.5. Tetradymite colloidal compounds

Bismuth and antimony chalcogenides have attracted huge interest in the field of thermoelectric[312,313] materials because of their heavy mass. More recently, they have appeared as a model system for 3D topological insulators.[314] In this phase of the matter, the bulk material is expected to be an insulator, while surface conducting states are formed. Bi_2Te_3, Sb_2Te_3 and Bi_2Se_3, are narrow band-gap semiconductors, with band gap value ranging from 0.2eV to 0.3eV. They have a rhombohedral structure with a lattice parameter of roughly 1 nm (quintuplet layer). As a result, they tend to grow under a layer form, with covalent bonds within the plane and where the quintuplets are stacked by weak Van der Waals interaction, as evidenced by TEM picture on Figure 37 b. Due to their lattice geometry, they form hexagonal plates in solution with a tunable lateral extension ranging from 100 nm to a few µm (see Figure 37 a).

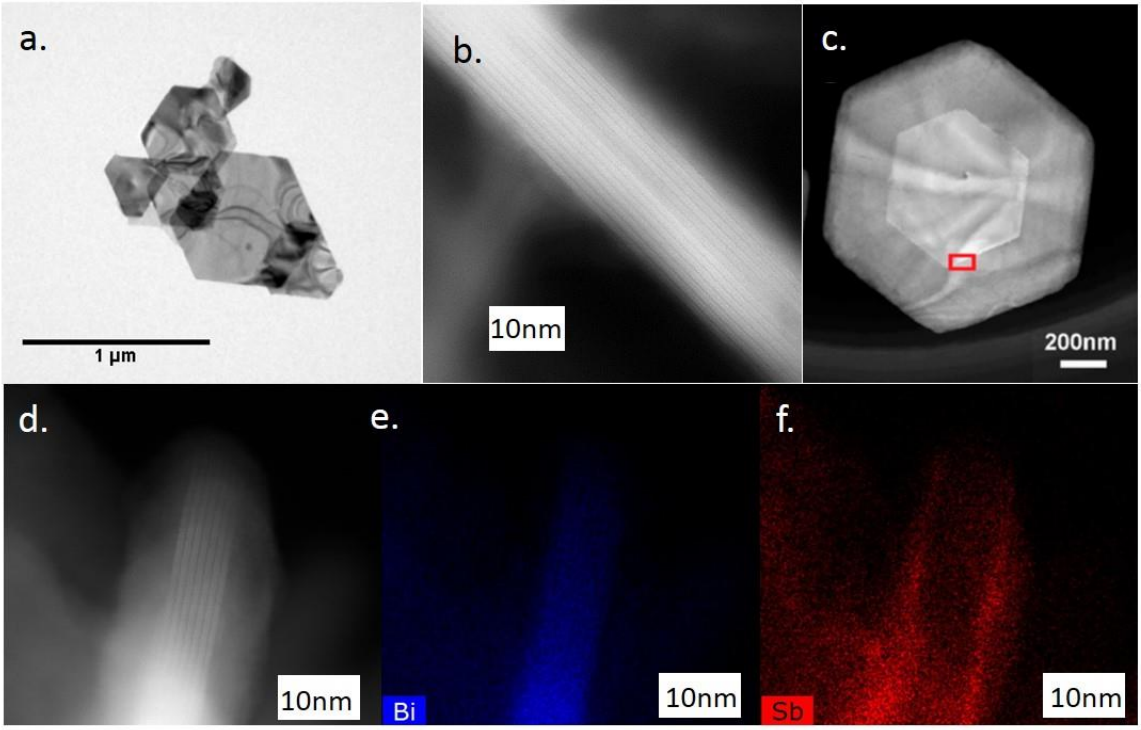

*Figure 37 a. TEM image of Sb_2Te_3 nanoplates. b. High resolution TEM image of Bi_2Te_3 nanoplates. c. TEM image of Bi_2Te_3- Sb_2Te_3 core/crown structure, adapted with permission from ref.*315*. Copyright (2015) American Chemical Society. d. TEM image of Bi_2Te_3- Sb_2Te_3 core/shell structure. e and f are EDX maps on for Bi and Sb respectively on the same area as the part seen in d.*

Their colloidal synthesis[316] has been mostly investigated using hydrothermal path in water[317–320] or polar solvents[315,321,322] as reaction media. More recently, a synthesis conducted in organic non-polar phase has been proposed[323]. The growth relies on the preparation of Bi and antimony oleate. The latter is mixed with a non-coordinating solvent (octadecene) and the reaction with TOP-Te occurs above 120°C. The obtained nanoplates have a thickness between 3 and 50 nm while the lateral size can be tuned with time and temperature. As for Cd based nanoplates, the synthesis has been extended to heterostructures in a core/crown[315] (Figure 37 c) and core/shell[323] (Figure 37 d-e) geometry.

The obtained plates tend to present some antistructural defects[324–326] where in the case of Sb_2Te_3, Te atoms replace some of the cations which tends to result in a p-type doping.[327] Bi_2Se_3 is generally n doped because of similar defects. Among the open questions regarding these materials is the control of their doping, which is a critical question for the observation of the topological surface states. In this sense synthesis leading to a better control of the stoichiometry of the compound is highly desirable.

6. Alternative growths and hybrid materials

While most of the methods to grow 2D anisotropic colloidal nanoparticle can be ranked among the four previously described mechanisms, we have identified several other alternative processes which can possibly expand the range of available 2D materials. Here we discuss the light induced anisotropic growth, the cation exchange and the growth of 2D perovskites.

6.1. Light induced methods

Although wet chemical methods have mostly been studied in the recent past, other synthesis methods exist that present some advantages. In the case of metal nanoparticles for example, direct chemical or thermal synthesis do not offer the same level of control as photochemical synthesis where the reaction of NP growth can be stopped only by removing the irradiation light. In such a synthesis, the excitation light (of a wavelength usually chosen at the plasmon resonance energy of the NP) is absorbed by NPs, and creates an electron-hole pair where the electron reduces the metallic precursors for further growth, while the hole oxidizes the ligands on the surface on NPs.[328,329] This method has been used to grow silver nanoprisms by Maillard *et al.*[329] The ligand used in this synthesis was citrate. Although the final size of the NPs can be controlled by the wavelength of the irradiation light (the NP grows until it stops absorbing light at this particular wavelength), the latter does not seem to play a role in the control of the thickness of the NPs,[330,331] suggesting that the final anisotropy of the NPs is not due to the irradiation, but to some intrinsic properties of the initial seeds or ligand templating, as described previously.[332–334] It has been observed that the illumination of citrate-capped Ag spherical seeds (<10 nm), in the presence of bis(p-sulfonatophenyl)phenylphosphane dihydrate dipotassium salt (BSPP), although a similar result was obtained with poly(vinylpyrrolidone) (PVP),[335] formed 100 nm-edge-long nanoprisms.[336] The mechanism behind this conversion from spherical NPs to nanoprisms can be explained by the selective aggregation of the seeds into small clusters, some of them with an anisotropic, two-dimensional shape. The latter are probably further stabilized by citrate ions whose binding to {111} facets is favored compared to other facets where ligands may be destabilized due to plasmon excitation.[337,338] The subsequent dissolution of the clusters allows for the growth of the nanoprisms at the expense of the clusters (see Figure 38).

*Figure 38: At the early stages of the synthesis, nanoplates and spherical particules are formed. The clusters dissolve and redeposit on the nanotriangles that act as seeds for further growth. From ref.*336*. Reprinted with permission from AAAS.*

Light-induced methods are not limited to photochemical redox reactions. Indeed, light can also be used as a driving force towards oriented aggregation. Using a fluorescence tube, Ji *et al.*[337] have seen that a longer excitation wavelength produces larger Ag nanoprisms. By changing the wavelength from 450 to 750 nm, the edge of the nanoprisms increased from ~40 to 120 nm.[337] The authors explained this by an oriented attachment mechanism (see Figure 39) which could be suppressed using a secondary excitation beam with a properly chosen wavelength (see Figure 40). By choosing a secondary excitation wavelength for the quadrupole plasmon excitation, the interparticle fusion was stopped due to a reorganization of charges at the particle surface. The dipole plasmon excitation, however, which is also present when a fluorescence tube was used, favors aggregation. Finally, many other parameters have to be taken into account, such as pH[339] or temperature, that could also change the final shape of the nanoparticles in the light-mediated synthesis.[328]

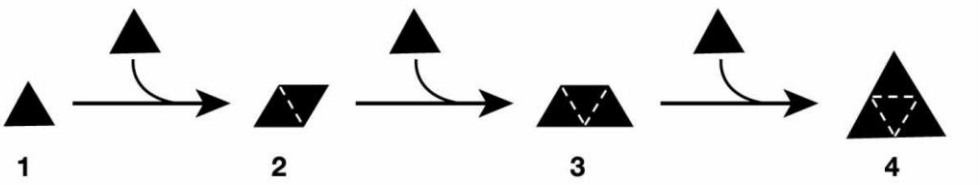

*Figure 39 : Light-induced nanoparticle aggregation, where 4 smaller nanoplates attach in an oriented manner to form a larger one. Reprinted by permission from Macmillan Publishers Ltd: Nature from ref.*337*, copyright (2003).*

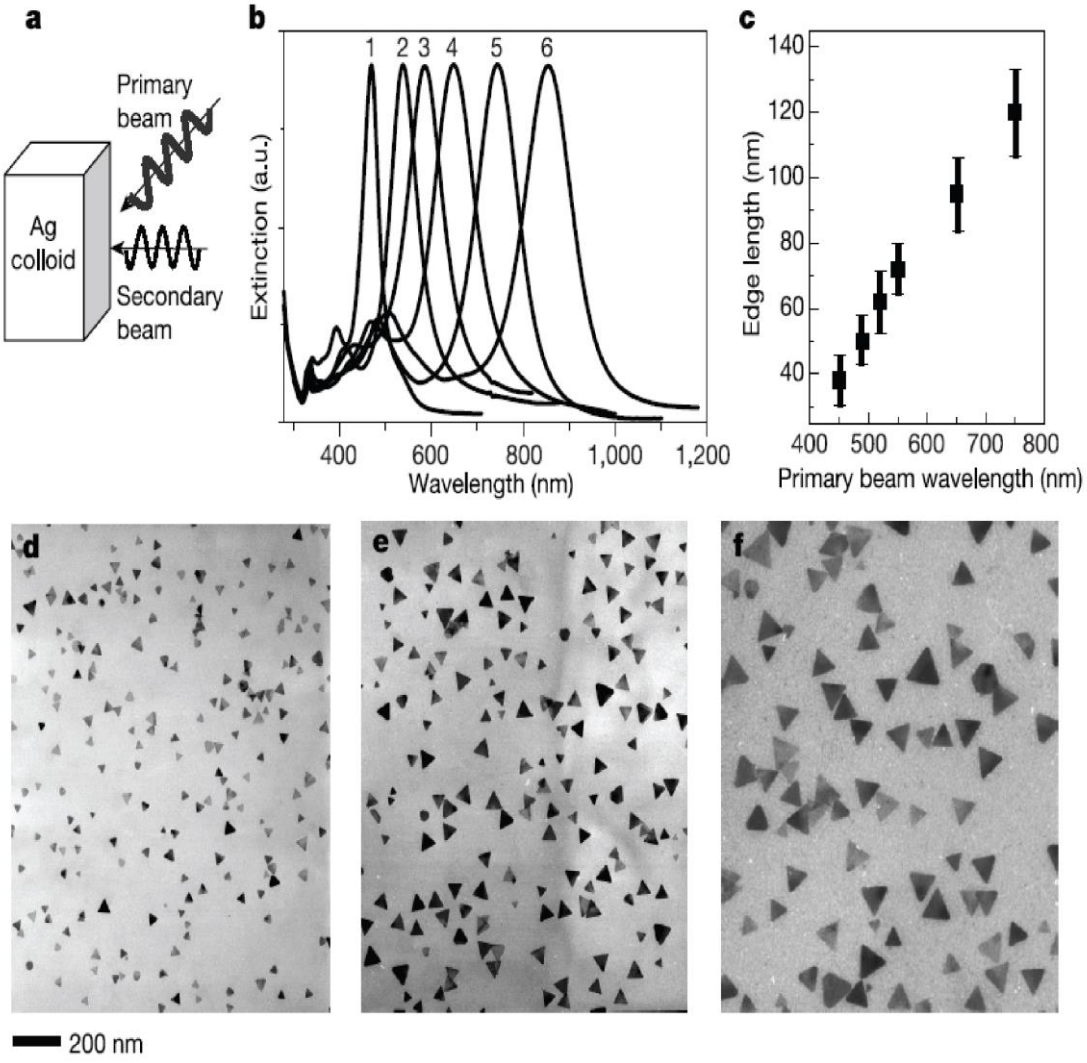

Figure 40: (a) Schematic diagram of dual-beam excitation. (b) The optical spectra (normalized) for six different-sized nanoprisms (1–6 edge length: 38±7 nm, 50±7 nm, 62±9 nm, 72±8 nm, 95±11nm and 120±14 nm) prepared by varying the primary excitation wavelength (central wavelength at 450, 490, 520, 550, 650 and 750 nm, respectively; width, 40 nm) coupled with a secondary wavelength (340 nm; width, 10 nm). (c) The edge lengths as a function of the primary excitation wavelength. (d–f) TEM images of Ag nanoprisms with average edge lengths of 38±7nm (d), 72±8nm (e) and 120±14nm (f). Scale bar applies to panels d–f. Reprinted by permission from Macmillan Publishers Ltd: Nature from ref.[337]*, copyright (2003).*

6.2. Cation exchange

In spite of huge progress over the past few years, some materials remain difficult to obtain under a 2D form. In this perspective cation exchange[340] is an interesting path to expand the range of available materials. The method was adapted to nanocrystals by Son *et al.*[341] It consists in introducing some small cations such as Ag^+ or Cu^+, in the presence of nanocrystals. Thanks to their small cationic radius, the ions can penetrate the atomic lattice of the nanocrystal. If the reaction is slow enough, the anion lattice remain unaffected while the initial

cations get removed and replaced by the new cations. Since the Ag^+ and Cu^+ ions are strongly sensitive to oxygen, the reaction needs to be conducted in a glove box. Starting from a cadmium chalcogenides NPLs, such process leads to the formation of Ag_2X or Cu_2X,[342] as shown in Figure 41 c. The optical properties of the NPLs are strongly affected and switch from an excitonic feature to a plasmon resonance. A second cation exchange step can then be conducted back to the initial cation or towards another cation. The second cation exchange is not as easy: the new cation has to be introduced in a large excess and the solution has to be heated. Nevertheless it is possible to obtain with this process NPLs of ZnS and PbS[343] (see Figure 41 a). Bouet *et al.*[343] evidenced that the cation exchange occurs gradually along the thickness direction (see Figure 41 b), which is consistent with the coexistence of the CdSe and Cu_2Se phase in the XRD diffractogram, as shown in Figure 41 c. The same strategy has been used by Kuno group to prepare ultrathin $Cu_{2-x}Se$ nanosheets (1.6 nm thick) exhibiting quantum confinement as well as a strong surface plasmon resonance in the infrared, induced by the copper vacancies.[342]

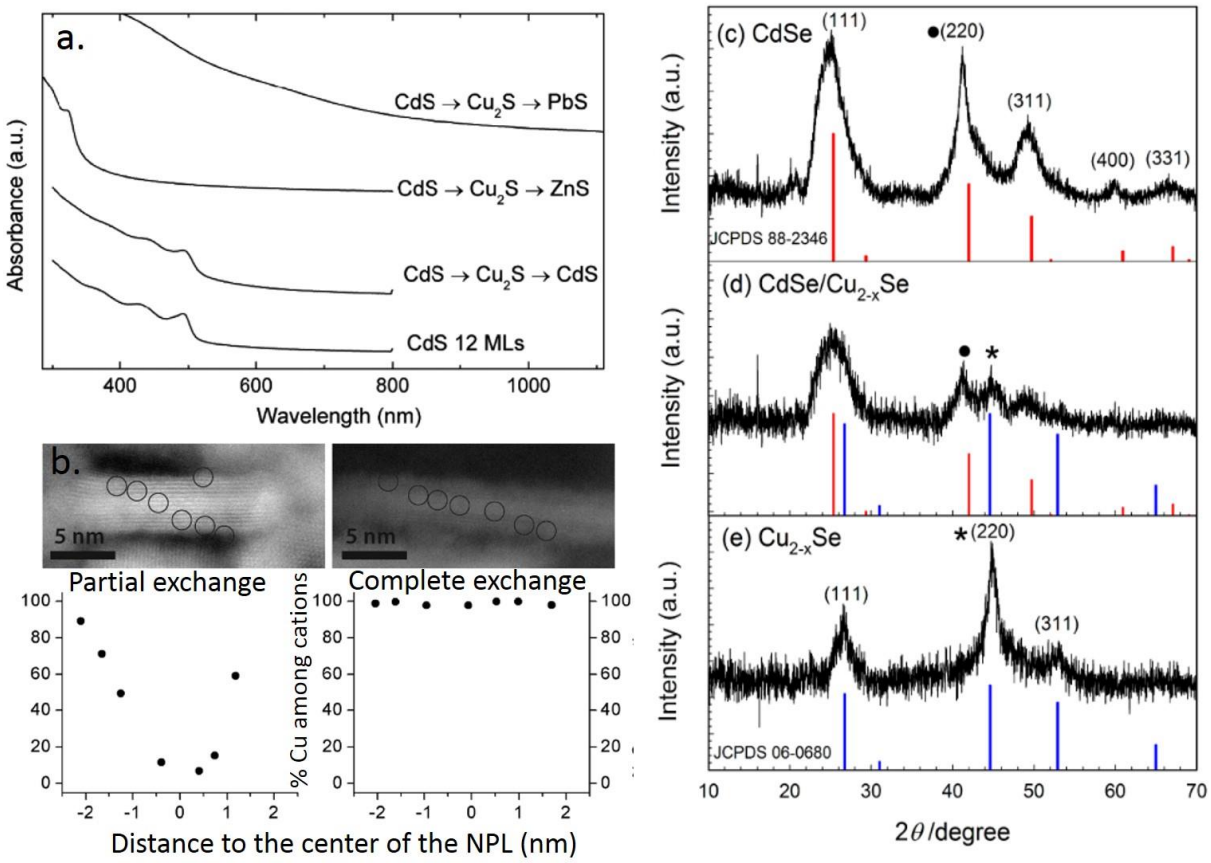

Figure 41 : a. Absorption spectra of CdS NPLs, of CdS NPLs after their back exchange from Cu_2S, of ZnS NPLs after their exchange from Cu_2S and of PbS NPL after their exchange from Cu_2S. b. Cu content for different position on a partially (left) and completely (right) exchanged CdSe/CdS NPLs. The top part is a TEM image where the rounds indicate the position of the EDX

analysis. Adapted with permission from [343]. Copyright (2014) American Chemical Society. c. XRD diffractogram of CdSe, CdSe/Cu_2Se and Cu_2Se NPLs obtained at different step of the Cu^+ ligand exchange. Adapted with permission from [342]. Copyright (2014) American Chemical Society.

6.3. 2D perovskites

The rediscovery and fast development of the halide perovskite materials has been initially induced by their successful use as sensitizers for DSSC solar cells.[344] After a few years of development only, the perovskite solar cells reach record efficiencies of about 20%.[345] Meanwhile, other potentialities of halide perovskites have been explored. Thanks to their high absorption cross-section,[346] near unity fluorescence quantum efficiency[347,348] and exceptional charge diffusion length,[349] halide perovskites, under bulk, thin films or nanoparticles shapes are a potential game changer in diverse applications such as light-harvesting,[350] photo-detection[351] or light-emitting devices.[352,353]

Halide perovskites are of general formula ABX_3, where X is a halogen anion, A is generally lead or tin and B is an organic ammonium or a cesium cation. They can adopt diverse crystal structures depending on their composition and generally undergo several phase changes depending on the temperature.[354,355] While methylammonium lead iodide has been extensively studied over the past few years for photovoltaic applications, other compositions are scrutinized as well for different applications. In particular, if lamellar hybrid perovskites systems have been known for quite a long time,[356,357] the colloidal synthesis of two dimensional hybrid perovskites has only been achieved very recently. Lamellar hybrid perovskites can be obtained when B is an organic ammonium with a bigger carbon chain such as butylamine for example. Furthermore, by varying the ratio metylammonium/long-ammonium cations, it is possible to prepare different lamellar perovskites with a perfectly defined number of PbX_6^- octahedra planes sandwiched by long ammonium ligands, of general formula $(CH_3(CH_2)_3NH_3)_2(CH_3NH_3)_{n-1}Pb_nX_{3n+1}$ (n =1, 2, 3, and 4) for example[358] and behaving as multiple quantum wells.[359] We can either see their colloidal synthesis as similar to the preparation of colloidal nanosheets from materials with a layered crystal structure, or as a soft templating system. On can also point out the similarities of such syntheses with other hybrid lamellar semiconductor preparation schemes like the II-VI semiconductors diamines hybrid materials previously reported. These hybrids can be of diverse compositions: ZnTe[360], ZnSe[361], MnSe[361], CdSe[362], and the thickness of the inorganic layer can also be perfectly controlled through the reaction temperature[363]. Modifications of these syntheses led to the preparation of colloidal CdSe nanosheets for example.[63]

Different strategies have been reported to prepare and study these ultrathin hybrid perovskite crystals. As for other lamellar systems, a first way to obtain them is to mechanically exfoliate bulk lamellar crystals. For example, Baumberg and coworkers report the micromechanical exfoliation of $(C_6H_9C_2H_4NH_3)_2PbI_4$ crystals and identify mono- and few-layers areas with an interlayer spacing of 1.6nm. Differences of behavior from the thinnest regions compared to the bulk are reportedly due to strain relaxation and ligands reorganization.[364] Similarly, Heinz and colleagues exfoliated $(C_4H_9NH_3)_2PbI_4$ crystals but observed strong differences between the bulk and the nanolayers. Due to the change in dielectric environment for example, the exciton binding energy increases by 1/3, up to 490 meV.[359]

Direct growth of hybrid perovskites on a substrate is also possible, simply by dropping a diluted solution of precursors on a hot substrate and let the solvent evaporate. Squared nanosheets of $(C_4H_9NH_3)_2PbBr_4$ are obtained, with lateral dimensions of a few micrometers and thicknesses down to the monolayer. The observed band gap shift towards higher energies compared to the bulk is attributed to structural relaxations.[365]

These methods reported above do not lead to colloidal nanosheets in solution and use lamellar hybrid perovskite systems to obtain monolayers. Direct colloidal syntheses, inspired by the existing ones forming isotropic nanocrystals,[366] have been recently reported for ammonium as well as cesium lead halide perovskites nanoplatelets.

A first approach uses a modification of the colloidal $CH_3NH_3PbBr_3$ perovskite synthesis reported by Schmidt *et al.,*[367] consisting in the reaction of $PbBr_2$ with a mixture of CH_3NH_3Br and longer ammonium bromide in the presence of oleic acid and octadecene. Using octylammonium bromide and carefully purifying the resulting nanostructures, Tisdale group isolated 2D perovskite nanoplatelets of monolayer thickness.[368] It is also possible to tune the thickness of the perovskite nanoplatelets by varying the octylammonium / methylammonium bromide ratio. In this case, nanoplatelets of 1 to 5 $PbBr_6$ octahedra planes are formed, allowing the authors to study the quantum confinement effects in these perovskite quantum wells.[369] A two-step procedure has also been reported, involving the synthesis of PbI_2 nanocrystals which are subsequently infiltrated with ammonium ions, leading to colloidal nanocrystals of lamellar perovskite. [370]

Cesium lead halide perovskites have also been synthetized under the shape of nanoplatelets, with a good control of the thickness of the plates. A first report by Alivisatos and coworkers describes the formation of nanoplates with thicknesses ranging from 1 to 5 unit cells,[371] using a modification of the colloidal synthesis of $CsPbBr_3$ nanocubes by Protesescu *et al.*[348] These nanostructures are strongly luminescent (up to 84% QY) and their composition can be subsequently tuned using a cation exchange procedure, to prepare $CsPbI_3$ and $CsPbCl_3$ nanoplates. The same materials under the shape of nanoplatelets have also been

reported by the group of Manna,[372] using this time a room temperature synthesis conducted in air, where a mixture of Cs oleate, oleylamine, oleic acid, $PbBr_2$ and HBr is destabilized by injection of acetone, leading within seconds to the formation of nanoplatelets. In this case the thickness is simply controlled by the amount of HBr initially present in the mixture.

Such colloidal 2D nanostructures with extremely high quantum yield and narrow photoluminescence can readily find applications for the development of light-emitting diodes[373] or laser gain media.[347]

7. Applications and perspectives

In the last section of this review we discuss some applications of the 2D colloidal nanocrystals. At first we discuss in which way the physical properties of 2D objects are affected by their dimensionality. We then review some of their use for optoelectronic, chemical and biological applications.

Before developing the different applications of 2D colloidal nanocrystals, it is needed to point out that the syntheses rarely yield only one population of NCs, and several sizes as well as several shapes can coexist in the reaction mixture. In order to get rid of the unwanted shapes of NCs, sorting of NPs has to be performed. Several methods exist to select one size or shape over the others. The first one is centrifugation.[130,374] Two-dimensional platelets of CdSe can be separated from spherical QDs by mere centrifugation due to their quite large difference in lateral size. This separation is possible thanks to the shape-dependent drag in the solution which gives different sedimentation velocities according to the ratio between effective mass and friction factor.[374,375] Size-selective precipitation can also be performed by adding a non-solvent that will destabilize the largest NPs which can then be easily separated by centrifugation.[376] These methods are often limited by the small differences in the sedimentation coefficients of the different shapes of NPs, and by the necessary repeated centrifugation steps that make them time consuming. Capillary electrophoresis as well as size exclusion chromatography have also been used to separated different shapes of Au and Ag NPs. The aggregation of NPs in the capillary and the chromatography column was avoided by adding a surfactant that also increased the resolution. The overall yield and throughput of these methods remain limiting for larger scale applications.[377,378] The addition of surfactants can be used in a different way to separate different shapes: indeed, the formation of micelles, above the critical micellar concentration, has been used to perform depletion-induced shape sorting.[379] When colloids (NPs) are separated by a distance smaller that the size of another species in solution (micelles), the formation of a concentration gradient produces an attractive osmotic pressure that pushes towards the aggregation and precipitation of NPs having the largest contact area. By playing on the concentration of the micelles, the attractive potentials between colloids can be discriminated for colloids of different shapes, and shape-selective precipitation can be performed. Finally, electrophoretic separation of NPs has been recently presented.[138] Directly after the synthesis, depending on the surface charge of the NPs, nanoplatelets can be easily separated from the spherical particles present in solution, without any major loss in their optical properties.

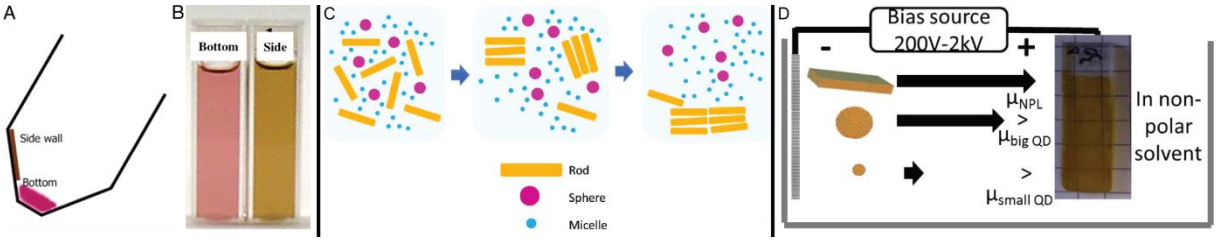

*Figure 42: A. Schematic drawing of a centrifuge tube after precipitation of Au nanoparticles depending on their size and aspect ratio. B. Corresponding solutions of Au NPs precipitated at the bottom or on the side wall of the centrifuge tube in A. Reproduced from ref.*374*. Copyright (2009) National Academy of Sciences, USA. C. Scheme of depletion-induced size- and shape-sorting. Reprinted with permission from ref.*379*. Copyright (2010) American Chemical Society. D. Scheme of electrophoretic separation of spherical and two-dimensional NPs of semiconductor in a non-polar solvent after the synthesis. Adapted with permission from ref.*138*. Copyright (2014) American Chemical Society.*

7.1. Why is 2D special ?

In addition to the challenge of their synthesis, 2D colloidal materials raise great promises in terms of new properties with respect to 0D nano-objects. In this section we discuss some of the specific physical properties resulting from their dimension.

From an electronic transport point of view, 2D materials are of utmost interest to achieve improved conduction. Transport in nanocrystals array occurs through a hopping process. At each step, the charge carriers have to face a tunneling barrier resulting from the presence of ligands at the nanoparticle surface. Short ligand passivation[194,380,381] allows the improvement of carrier mobility, nevertheless reducing the number of hopping steps may also be an alternative method to rise the overall conductivity. Thanks to their large lateral extension, 2D nanomaterials are perfect candidates to reduce the number of hopping steps by a ratio of their lateral size over their confined direction. In addition, the wavefunction overlap of two plates is expected to be proportional to their overlapping area. 2D objects will consequently present larger neighbor-to-neighbor coupling than the punctual contact arising from two spheres. However careful experimental evidence of this dimensionality effect still needs to be obtained.

The electronic structure of 2D colloidal objects differs from 0D objects in the sense that quantum confinement is not prevailing in all directions and plane-wave-like states possibly exist within the plane direction. From an optical perspective, 2D objects present a fairly different density of states than the sparse one of 0D nanoparticles. It raises the possibility to inject more carriers and excitons within the same nanocrystal. Compared to bulk object they also differ by their lower screening of the charge. Indeed, colloidal nanocrystals are surrounded by a low dielectric index medium (solvent, ligand…), contrary to bulk or even

epitaxially grown quantum wells. As a result, there is strong dielectric contrast between the semiconductor and its environment, which results in dielectric confinement. Due to this dielectric contrast, the mirror-charge effect is enhanced and the charges are pushed away from the surface. This leads to a positive value for the self-energy which should impact the predicted energy spectrum, however the latter is almost perfectly balanced by the binding energy (negative correction to the energy spectrum) of the exciton. For QDs, the binding energy is typically of a few meV for lead chalcogenides QDs (due to their very large dielectric constant) and of few tens of meV for cadmium chalcogenides. In the case of 2D nanoplates, this value is typically ten times larger. On PbS nanosheets,[382] it was recently estimated to be around 50meV while for CdSe, its value can be as large as 200-300 meV.[383,384] Due to this cancelation, the effective mass model solved for an infinite well leads to surprisingly good prediction of the energy spectrum of the colloidal nanosheets.[13] Nevertheless the large dielectric contrast and large binding energy of the exciton keeps impacting optical and transport properties of the NPLs as discussed in the following part of this section.

7.2. Application for light emission

NPLs, with their extremely narrow PL linewidth are obvious candidates as next generation phosphor for display. Over the last three years, colloidal QDs have started to replace rare earth based phosphor to produce white light for displays.[385] Indeed, the PL signal coming from lanthanide based compound is broad (80-100nm) which presents two main drawbacks: (*i*) a limited gamut (*ie* how many colors can a display reproduce) which is especially limiting in the green. And (*ii*) near infrared emission which corresponds to light emission in an eye-insensitive range of wavelengths. The latter can alternatively be seen as loss of plug efficiency. Colloidal QDs present narrower PL signal (30-40nm FWHM for core/shell nanocrystals) and are now used for gamut enhanced display. Compared to OLEDs, they are cheaper because they are compatible with LCD technology while producing similarly high quality of color. NPLs with FWHM down to 20 nm can become the next generation of nanocrystal-based phosphors for display as long as they are able to sustain the operating conditions (high flux: 100 $mW.cm^{-2}$ and high temperature: 100°C) requested for such applications. This will request the development of encapsulation methods suited for NPL surface chemistry.

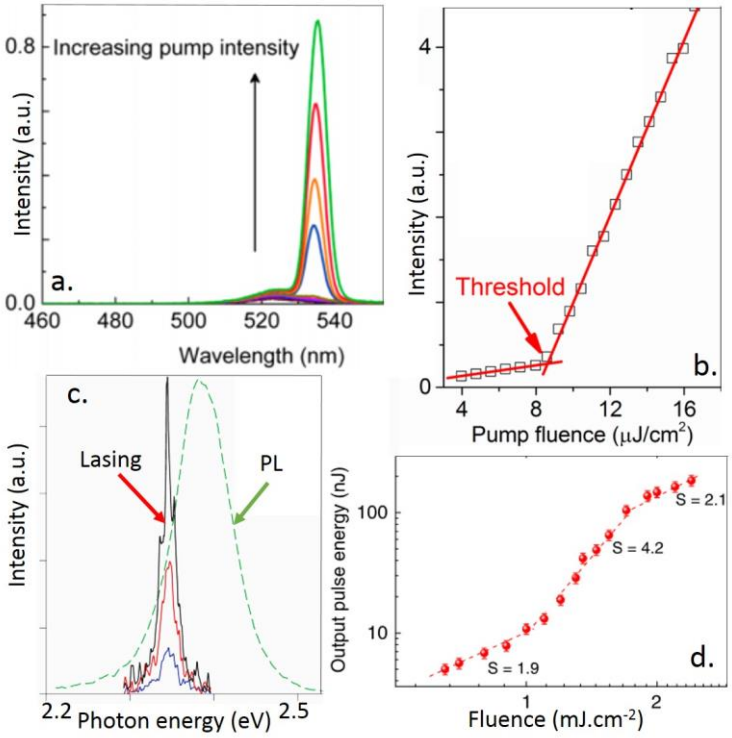

Figure 43: a. Amplified stimulated emission spectra of CdSe NPLs for different intensities of the pump, Adapted with permission from reference [386]*. Copyright (2014) American Chemical Society. b. Integrated intensity of the luminescence as a function of the pump intensity for CdSe-CdS core shell NPLs, Adapted with permission from reference* [387]*. Copyright (2014) American Chemical Society. c. PL and lasing of CdSe NPLs under different pump powers. Reprinted with permission from Macmillan Publishers Ltd: Natutre Nanotechnology from ref. 12, copyright (2014). d. Two photon (λ≈800nm) pumped cadmium chalcogenides nanoplates stimulated emission intensity as a function of the pump power, adapted from reference* [388]*.*

Lasing is also an obvious application of NPLs, because it also takes advantage of the short PL lifetime (few ns at room temperature) of the NPLs. Colloidal quantum dots have started being used as gain medium[389] to build random laser in the beginning of the 2000's. In spite of huge progress, the threshold irradiance to reach the stimulated regime remains high[390] (several $mJ.cm^{-2}$). NPLs have really been a breakthrough in this sense, since the threshold level has been lowered[386] by three decades (see Figure 43 a and b). With NPLs, the threshold[387] can be below 10 $\mu J.cm^{-2}$ with gain around 600 cm^{-1}. Insertion of the NPLs in an optical cavity has led to lasing signal[12,386,391] (see Figure 43 c). The lasing linewidth is typically 2 nm.[386] This performance also stands while the device is pumped in a multiphoton regime.[388] Two[386] and three[388] photon pumping have been demonstrated. In a two-photon pumped (λ≈800nm) configuration, the stimulated emission threshold remains low (1-10 $mJ.cm^{-2}$). The exact origin of this improvement of the lasing performance remains mostly ununderstood, however we can speculate that the reduced Auger and larger density of states of the NPLs are key elements.

7.3. Application for photodetection

Thanks to the fine control of the band edge energy, NPLs appear as interesting candidates for photodetection with sharp control of the cut-off wavelength. The phototransport in nanoplatelets arrays have been first reported by Pedetti *et al*.[142] With CdTe NPLs, the current under illumination is two to three times larger than under dark condition. With CdSe or CdSe/CdS NPLs this modulation is even larger[392] and can be as high as 10^4. However the overall photoresponse of the film remains low (tens of $\mu A.W^{-1}$) which corresponds to weak internal efficiency (<<1%).

To improve the performance, it was proposed to switch from a photoconductive device to a phototransistor, to take advantage of the non-linear dependence of the current with the gate bias. Moreover, gating of the film allows a fine control of the carrier density and is able to tune the filling of the trap states. Electrolyte gating of cadmium chalcogenides NPLs has been proposed.[153] The method relies on the use of ion gel electrolyte ($LiClO_4$ in polyethylene glycol: PEG). This method combines several advantages compared to conventional gating based on liquid electrolyte. First, the size of the device can be shrinked since no bulky and leaky electrochemical cell are necessary. Secondly, the device can be operated in air. Finally, since PEG is a solvent for $LiClO_4$, no solvent needs to be added and this prevents the exposition of the NPLs to an annealing step necessary to remove the electrolyte solvent. This gating allows a large tuning of the conductance[393] with on/off ratio above 10^8, while keeping the voltage range low (<3V).

This gating method can be used not only to tune the dark conductivity but also the photoconductivity of the system. Indeed, electrolyte gating allows a large tuning of the Fermi level of the system which can be used to control the filling of the trap states. In non-gated semiconductors, a photogenerated electron has a limited lifetime because of the possible trapping of the photocarriers by shallow traps. Once the system is gated, the Fermi level can be pushed toward the band presenting trap states, and fill these traps. As a result, the photogenerated carriers can no longer be trapped and their lifetime in the band is extended, leading to gain effect. This method has been applied to NPL films (see the inset of Figure 44 a for a scheme of the device). The idea is to prepare the system close to the current turn on point in the transistor subthreshold regime. Here the current dependence with the carrier density is exponential. Thus the photogenerated carrier density leads to an enhanced current modulation as shown in Figure 44 a, where the photocurrent rises by more than two decades thanks to the gate. The gate bias cannot be pushed too far otherwise (i) dark current also rises and (ii) the absorption of the carriers gets bleached once the Fermi level is pushed into one of the band. Another interesting use of this electrolyte gating of NPL film is the development of

bicolor detectors.[392] By combining in parallel a film of CdSe/CdS NPLs with some HgTe nanocrystals,[394,395] one can use the gate as a switch to selectively obtain photoresponse in the visible and near infrared[396] using mercury chalcogenide[381,397,398] nanocrystals or in the visible only when the photoresponse of the NPLs prevails.

In spite of the progress resulting from the filling of the trap states, the overall responsivity of the gated NPL film remains low (10 $mA.W^{-1}$). However, the NPLs have so far been treated as conventional (*i.e.* 0D) nanocrystals and the device geometry does not consider their 2D nature. As stated earlier, 2D nanosheets present a large binding energy (50-250 meV >> k_bT). The latter needs to be overcome to achieve an efficient electron-hole dissociation. As a result, a fairly large electric field have to be applied over each NPL. To do so, an interesting way is to shrink the device size. Indeed, such modification of the device not only leads to larger electric fields but also to a lower sensitivity of the device to the presence of defects within the film. Indeed, to ensure a strong local coupling, ligand exchanges are generally conducted, however they lead to a decrease of the volume of the film due to the shortening of the ligands and this tends to form cracks at the µm scale. These cracks make the percolation path of the carrier up to the electrodes even more complex. Smaller devices are thus expected to lead to larger conductivity.[399] The size of the device can be reduced down to a single NPL. To do so nanofabrication is necessary. Nanogap and nanotrench electrodes have been obtained through a variety of methods such as e-beam lithography,[400] electromigration[401,402] or shadowing[403] methods. Nanocrystal based photodetectors using nm-spaced electrodes have been proposed by Prins *et al*[404] and Willis *et al*[405], however the device keeps operating in the hopping regime since the nanocrystal are not larger that the electrode-spacing. On the other hand, NPLs, thanks to their large lateral extension can be more easily connected to the electrodes and this releases the constrain on the electrodes fabrication which “only” have to be spaced by tens of nm (see Figure 44 b). Such geometry of device has led to the best photodetection performance for colloidal based cadmium chalcogenides nanocrystals with extremely large photoresponse[10] ($kA.W^{-1}$). The device is able to conciliate large gain (3000 electrons are generated per absorbed photon) with high bandwidth (>kHz). This performance corresponds to an improvement[10] by a factor 10^7 compared to the same material connected with µm spaced electrodes operated in the hopping regime (see Figure 44 b). The only limitation to this approach is the decrease of the optical area which tends to limit the photon absorption.

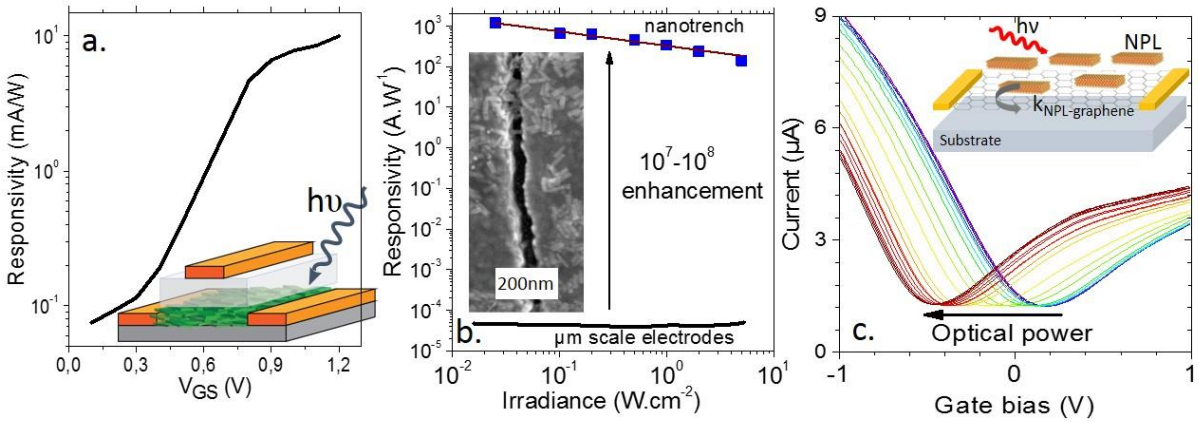

Figure 44 : a. Photoresponsivity, of a CdSe-CdS NPL film gated with an ion-gel electrolyte, as a function of the applied gate bias. The inset is a scheme of the device. Adapted with permission from reference [392]*. Copyright (2014) American Chemical Society b. Photoresponsivity of a CdSe/CdS-nanoplates film bridging a nanotrench as a function of the incident light power. The inset is a SEM image of the device. The data associated with the same film connected to 20 µm spaced electrodes are also plotted for comparison. Adapted with permission from reference 10. Copyright (2015) American Chemical Society. c. Current as a function of the applied gate bias for an epitaxially grown graphene layer functionnalized with CdSe/CdS nanoplates under different level of incident light power. The inset is a scheme of the device.*

Finally, other alternative paths have been tested to overcome the hopping transport limitation. In this sense, a hybrid system with graphene has been proposed. In such a device, QDs are used for their optical absorption and graphene for its high mobility. The device relies on the selective transfer of one carrier of the electron-hole pair towards the graphene. Indeed, if both carriers were transferred to graphene they would quickly recombine without leading to a current. The selectivity of the transfer of the carrier results from the higher proximity of one band of the semiconductor with the Dirac cones of the graphene. The charge remaining in the semiconductor is used to photogate the graphene.[406] The living time of this carrier in the semiconductor is generally longer than the transit time of the other carrier within graphene, thanks to its high mobility, which results in gain. With PbS quantum dots[407,408] exceptional device performances have been reported with record responsivity (10^7A.W^{-1}), even if the bandwidth is generally limited. Lead sulphide QDs strongly differ from the NPLs in the sense that the photocarriers almost behave as free charges due to the high dielectric constant of the material, while excitons within the NPLs are more strongly bound. As a result, the charge dissociation needs to be assisted at the nanocrystal scale. Robin *et al*[409] demonstrated that a possible way to split the electron-hole pair is to use heterostructured NPLs. They monitor the charge transfer using an electrolytic transistor configuration, as shown in Figure 44 c. They evidence that quasi-type-II and type-II band alignment allow a fine control of the nanocrystal-to-graphene charge transfer. Heterostructure NPLs present a lower binding

energy due to their lower overlap of the electron-hole wavefunction. This property is further used to control the sign and intensity of the transfer rate.

7.4. Applications for biology and chemistry

Metal nanoparticles are widely used in applications for chemical or biological sensing. These properties are mainly based on their strong surface plasmon resonance (SPR) which depends on the size and the shape of the NP.[410,411] For Au nanoplates for example, the spectral range of their SPR extends from the visible to the infrared window, covering the biological optical window for tissue.[56] By coupling the optical properties of Au nanoplates to a matched laser excitation, gold nanoplates show an efficient photothermal conversion for thermal damage on HeLa cells.[412]

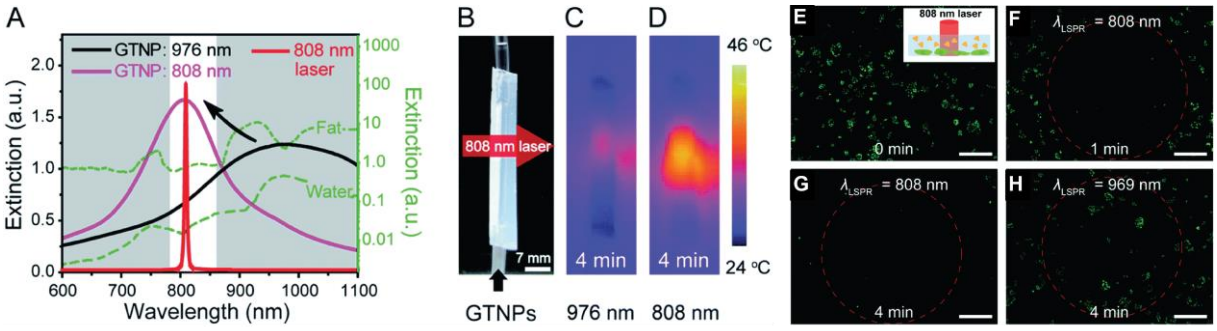

Figure 45: Precisely tuning the plasmon mode of GTNPs to the bio-window of tissue for the demonstration of photothermal conversion. (A) In pink, the extinction spectra of Au nanoplates with a plasmon resonance at 808 nm, in black the extinction spectra of Au nanoplates with a plasmon resonance at 976 nm, and in red, the emission spectrum of an NIR laser used in these experiments with a central wavelength at 808 nm. In green, extinction spectra of fat and water in this region as well as their relatively low extinction region (the white area); (B) photo of a agarose–fat channel as a simulated tissue. (C and D) The infrared images of the channel loaded with the Au nanoplates suspensions with plasmon modes at (C) 976 nm and (D) 808nm and then irradiated by the 808 nm NIR laser for 4 min. The temperatures at the center of the chip were up to 30 and 43°C for (C) and (D), respectively. Reproduced from Ref.[412] *with permission from The Royal Society of Chemistry.*

The strong SPR can be used for chemical sensing through Surface Enhanced Raman Spectroscopy (SERS) which is strongly dependent of the scattering properties of the metal NPs. Non-spherical metallic particles are of particular interest in this field as calculations have shown that the electromagnetic field is increased at sharp vertices such as tips of nanoplates, increasing the sensitivity of the SERS method.[413]

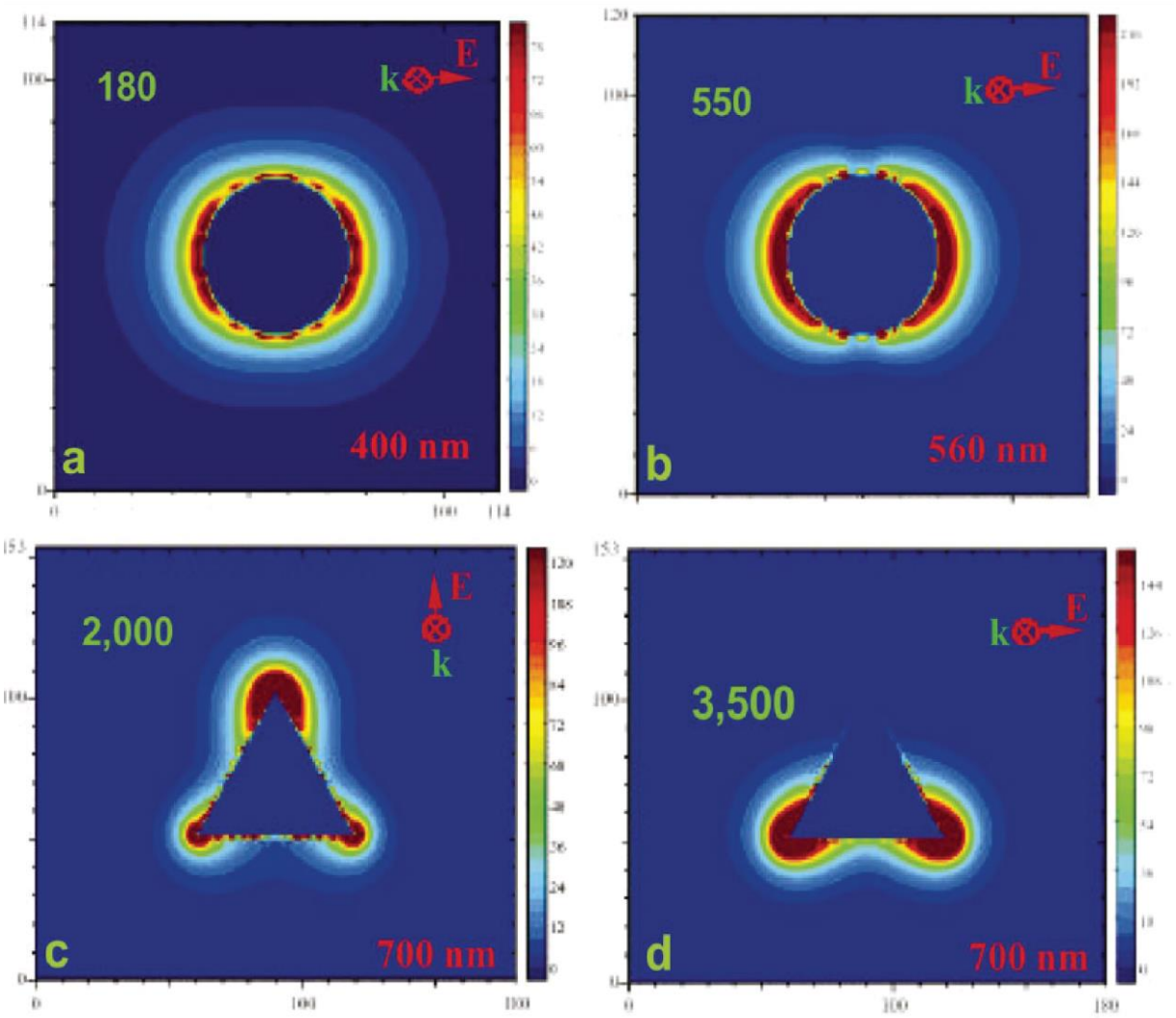

Figure 46: Electromagnetic field enhancement around Ag nanoparticles with different shapes: (a) Ag nanospheres (radius 19 nm); (b) Ag nanodisks (size=40 nm, thickness=9 nm) ; (c) and (d) Ag triangular nanoprisms (size=60 nm, thickness= 12 nm). The number in green indicates the maximal enhancement of the electromagnetic field at the wavelength indicated in red. Adapted from ref.[413]*. With permission from Springer Science+Business Media.*

Also used for their catalytic properties, Au NPs show a facet-dependent selectivity; the exposed facet is itself dependent on the shape of the NPs.[6] Moreover, the catalytic activity changes on different regions of gold nanoplates, increasing form flat facets to edges to corners. The specific activity of reduction of resazurin to resorufin by NH_2OH is ~8% higher at the edges than on the flat facets, and ~80% higher on the corners than of the edges of the Au NPs.[414] This again shows the dependence on the shape of the nanoparticle, and the advantages of a 2D structure over a spherical, 3D structure.

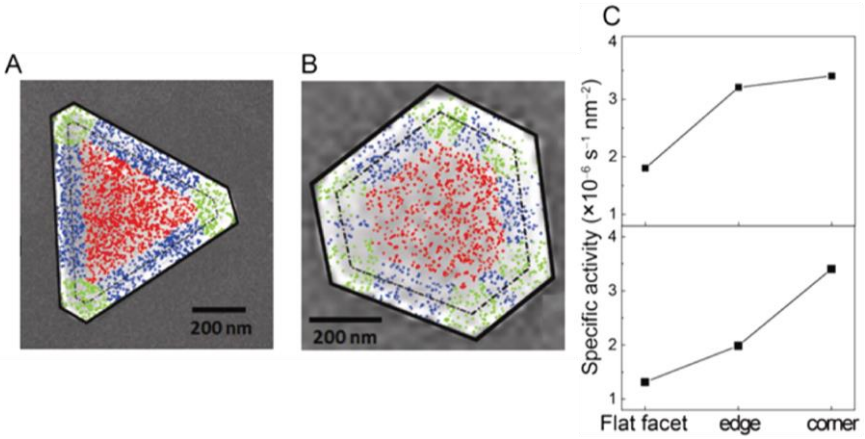

Figure 47: Spatially resolved activity quantitation on single silica-coated Au nanoplates. (A) Locations of 2325 product molecules overlaid on top of the SEM image of a silica-coated Au nanoplate. Each dot is the location of one product molecule. The locations are color coded according to their respective regions on the nanoplate: flat facet (red), edges (blue), and corners (green). The solid black line outlines the outer contour of the silica shell. The dashed black line outlines the perimeter of the Au nanoplate core. (B) Same as (A) but for a different silica-coated Au nanoplate with 1579 products detected. (C) Specific activities of the different regions of the nanoplates from (A, top) and (B, bottom). Adapted with permission from ref.[414]*. Copyright (2013) American Chemical Society.*

Semiconductor nanoplatelets, due to their exceptional optical properties presented previously (see part 3), are excellent candidates for biological probes. Their molar extinction coefficient is three orders of magnitude higher than the one of green fluorescent protein (GFP), and their narrow emission band could help perform multicolor imaging with limited bleed-through in the other imaging channels. However, their synthesis is performed in organic solvents and their stabilization in aqueous media is even more challenging that for 0D QDs as NPLs exhibit more surface atoms: the ligand exchange step to make them water-soluble strongly affects the surface atoms reducing their photoluminescence efficiency. A recent work by Sung Jun Lim and co-workers[415] shows that encapsulation of NPLs in lipoproteins makes them efficient probes for *in cellulo* imaging (see Figure 48). Not only that, but when compared to 0D QDs, only the NPLs showed efficient uptake in live human epidermoid carcinoma cells. The authors explain this uptake selectivity not by the surface chemistry (as other compounds with the same chemistry did not show any uptake), but by the large surface area of NPLs and their low curvature, facilitating multivalent interaction with the cell membrane.

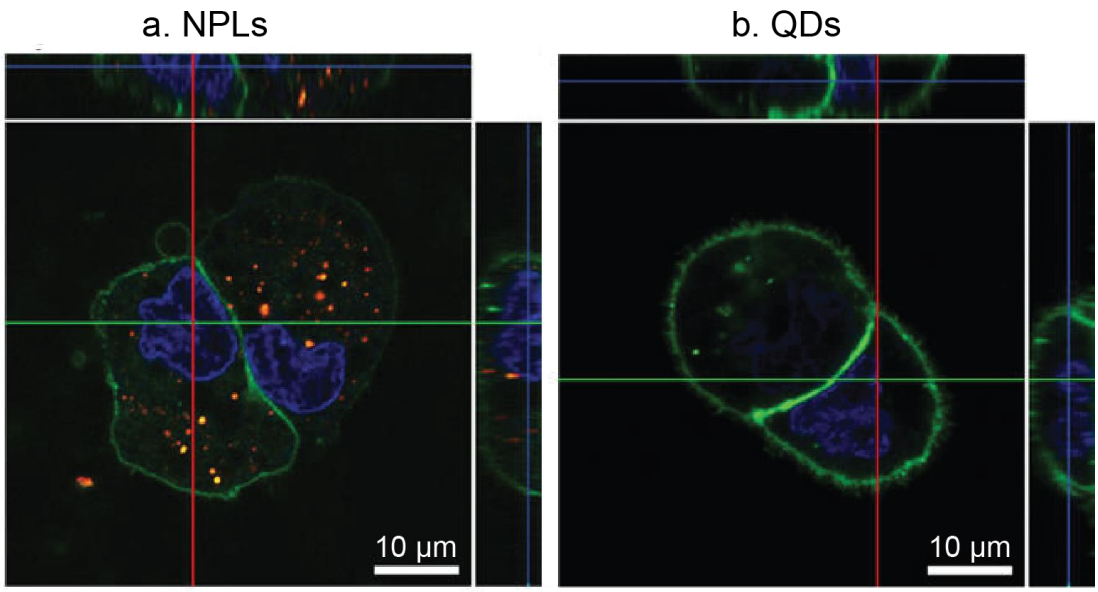

*Figure 48: Fluorescence confocal microscopy images of A431 human cells after 24h of exposure to (a) NPLs or (b) QDs. The top boxes correspond to the 3D z-stack along the green line, while the side boxes correspond to the 3D z-stack along the red line. Adapted with permission from ref.*415*. Copyright (2016) American Chemical Society.*

8. Conclusion

We discuss the growth of 2D colloidal nanocrystals. We have identified four main mechanisms which lead to the growth of such sheet-shaped objects which are:

- Defect induced anisotropy which is a very common mechanism to grow 2D metallic nanoparticles;
- Ligand engineering which includes the formation of lamellar phases but also ligand-tunable accessibility to the nanocrystal surface. This process leads to extremely high control of the thickness down to the atomic scale;
- Self-assembly of pre-formed nanocrystals into a 2D mesostructured;
- Anisotropic growth resulting from an anisotropic atomic lattice; this process is particularly common to grow transition metal dichalcogenides material.

In addition to these four main processes, alternative mechanisms relying on light activated growth and cation exchanges also extend the tool-box of chemists to grow 2D colloidal objects with a broader range of available materials.

In the final section, of the review we discuss in what ways the physical properties of 2D object differ from their 0D analog. In particular, the mirror charges and the large exciton binding energy strongly affect their optoelectronic properties. Their short PL lifetime have

attracted a lot of interest for their use as light emitter for down conversion and lasing. Moreover, they are also very promising for photodetection as long as the device geometry addresses their2D aspect by taking advantage of their anisotropy and by addressing how the exciton can be splitted. Finally, the use of 2D colloidal objects for chemistry and biology offers new possibilities for nanoparticle functionalization or for stronger selectivity.

Acknowledgments

BD and SI thanks Agence Nationale de la recherche (ANR) for funding through the grant SNAP H2DH and Nanodose. This work has been supported by the Region Ile-de-France in the framework of DIM Nano-K. This work was also supported by French state funds managed by the ANR within the Investissements d'Avenir programme under reference ANR-11-IDEX-0004-02, and more specifically within the framework of the Cluster of Excellence MATISSE led by Sorbonne Universités

References

(1) Yin, Y.; Alivisatos, a P. Colloidal Nanocrystal Synthesis and the Organic–inorganic Interface. *Nature* **2005**, *437* (7059), 664–670.

(2) Xia, Y.; Xiong, Y.; Lim, B.; Skrabalak, S. E. Shape-Controlled Synthesis of Metal Nanocrystals: Simple Chemistry Meets Complex Physics? *Angew. Chemie Int. Ed.* **2009**, *48* (1), 60–103.

(3) Valden, M.; Nagahara, H.; Fukuoka, Y.; Nagahara, H.; Konishi, M.; Ishii, Y.; Ura, T.; Ishii, Y.; Ogawa, M.; Venturello, C.; et al. Onset of Catalytic Activity of Gold Clusters on Titania with the Appearance of Nonmetallic Properties. *Science (80-.).* **1998**, *281* (5383), 1647–1650.

(4) Zecchina, A.; Groppo, E.; Bordiga, S. Selective Catalysis and Nanoscience: An Inseparable Pair. *Chem. - A Eur. J.* **2007**, *13* (9), 2440–2460.

(5) Shi, A.-C.; Masel, R. I. The Effects of Gas Adsorption on Particle Shapes in Supported Platinum Catalysts. *J. Catal.* **1989**, *120* (2), 421–431.

(6) Narayanan, R.; El-sayed, M. a. Catalysis with Transition Metal Nanoparticles in Colloidal Solution: Nanoparticle Shape Dependence and Stability. *J. Phys. Chem. B* **2005**, *109* (26), 12663–12676.

(7) Kelly, K. L.; Coronado, E.; Zhao, L. L.; Schatz, G. C. The Optical Properties of Metal Nanoparticles: The Influence of Size, Shape, and Dielectric Environment. *J. Phys. Chem. B* **2003**, *107* (3), 668–677.

(8) Chithrani, B. D.; Ghazani, A. a.; Chan, W. C. W. Determining the Size and Shape Dependence of Gold Nanoparticle Uptake into Mammalian Cells. *Nano Lett.* **2006**, *6* (4), 662–668.

(9) Chithrani, B. D.; Chan, W. C. W. Elucidating the Mechanism of Cellular Uptake and Removal of Protein-Coated Gold Nanoparticles of Different Sizes and Shapes. *Nano Lett.* **2007**, *7* (6), 1542–1550.

(10) Lhuillier, E.; Dayen, J.-F.; Thomas, D. O.; Robin, A.; Doudin, B.; Dubertret, B. Nanoplatelets Bridging a Nanotrench: A New Architecture for Photodetectors with Increased Sensitivity. *Nano Lett.* **2015**, *15* (3), 150210101529008.

(11) Deng, Z.; Cao, D.; He, J.; Lin, S.; Lindsay, S. M.; Liu, Y. Solution Synthesis of Ultrathin Single-Crystalline SNS Nanoribbons for Photodetectors via Phase Transition and Surface Processing. *ACS Nano* **2012**, *6* (7), 6197–6207.

(12) Grim, J. Q.; Christodoulou, S.; Di Stasio, F.; Krahne, R.; Cingolani, R.; Manna, L.; Moreels, I. Continuous-Wave Biexciton Lasing at Room Temperature Using Solution-Processed Quantum Wells. *Nat. Nanotechnol.* **2014**, *9* (11), 891–895.

(13) Ithurria, S.; Dubertret, B. Quasi 2D Colloidal CdSe Platelets with Thicknesses Controlled at the Atomic Level. *J. Am. Chem. Soc.* **2008**, *130* (49), 16504–16505.

(14) Joo, J.; Son, J. S.; Kwon, S. G.; Yu, J. H.; Hyeon, T. Low-Temperature Solution-Phase Synthesis of Quantum Well Structured CdSe Nanoribbons. *J. Am. Chem. Soc.* **2006**, *128*

(17), 5632–5633.

(15) Chen, Z.; Nadal, B.; Mahler, B.; Aubin, H.; Dubertret, B. Quasi-2D Colloidal Semiconductor Nanoplatelets for Narrow Electroluminescence. *Adv. Funct. Mater.* **2014**, *24* (3), 295–302.

(16) Takami, S.; Hayakawa, R.; Wakayama, Y.; Chikyow, T. Continuous Hydrothermal Synthesis of Nickel Oxide Nanoplates and Their Use as Nanoinks for P-Type Channel Material in a Bottom-Gate Field-Effect Transistor. *Nanotechnology* **2010**, *21* (13), 134009.

(17) Cha, J. J.; Koski, K. J.; Huang, K. C. Y.; Wang, K. X.; Luo, W.; Kong, D.; Yu, Z.; Fan, S.; Brongersma, M. L.; Cui, Y. Two-Dimensional Chalcogenide Nanoplates as Tunable Metamaterials via Chemical Intercalation. *Nano Lett.* **2013**, *13* (12), 5913–5918.

(18) Wang, Y.; Xiu, F.; Cheng, L.; He, L.; Lang, M.; Tang, J.; Kou, X.; Yu, X.; Jiang, X.; Chen, Z.; et al. Gate-Controlled Surface Conduction in Na-Doped Bi 2 Te 3 Topological Insulator Nanoplates. *Nano Lett.* **2012**, *12* (3), 1170–1175.

(19) Somorjai, G. a.; Park, J. Y. Colloid Science of Metal Nanoparticle Catalysts in 2D and 3D Structures. Challenges of Nucleation, Growth, Composition, Particle Shape, Size Control and Their Influence on Activity and Selectivity. *Top. Catal.* **2008**, *49* (3-4), 126–135.

(20) Gao, C.; Lu, Z.; Liu, Y.; Zhang, Q.; Chi, M.; Cheng, Q.; Yin, Y. Highly Stable Silver Nanoplates for Surface Plasmon Resonance Biosensing. *Angew. Chemie Int. Ed.* **2012**, *51* (23), 5629–5633.

(21) Homan, K. a.; Souza, M.; Truby, R.; Luke, G. P.; Green, C.; Vreeland, E.; Emelianov, S. Silver Nanoplate Contrast Agents for in Vivo Molecular Photoacoustic Imaging. *ACS Nano* **2012**, *6* (1), 641–650.

(22) Li, J.; Jiang, F.; Yang, B.; Song, X.-R.; Liu, Y.; Yang, H.-H.; Cao, D.-R.; Shi, W.-R.; Chen, G.-N. Topological Insulator Bismuth Selenide as a Theranostic Platform for Simultaneous Cancer Imaging and Therapy. *Sci. Rep.* **2013**, *3*, 1998.

(23) Li, H.; Wu, J.; Yin, Z.; Zhang, H. Preparation and Applications of Mechanically Exfoliated Single-Layer and Multilayer MoS 2 and WSe 2 Nanosheets. *Acc. Chem. Res.* **2014**, *47* (4), 1067–1075.

(24) Eda, G.; Yamaguchi, H.; Voiry, D.; Fujita, T.; Chen, M.; Chhowalla, M. Photoluminescence from Chemically Exfoliated MoS 2. *Nano Lett.* **2011**, *11* (12), 5111–5116.

(25) Chen, Y.; Tan, C.; Zhang, H.; Wang, L. Two-Dimensional Graphene Analogues for Biomedical Applications. *Chem. Soc. Rev.* **2015**, *44* (9), 2681–2701.

(26) Novoselov, K. S.; Jiang, D.; Schedin, F.; Booth, T. J.; Khotkevich, V. V; Morozov, S. V; Geim, a K. Two-Dimensional Atomic Crystals. *Proc. Natl. Acad. Sci.* **2005**, *102* (30), 10451–10453.

(27) Nicolosi, V.; Chhowalla, M.; Kanatzidis, M. G.; Strano, M. S.; Coleman, J. N. Liquid Exfoliation of Layered Materials. *Science (80-.).* **2013**, *340* (6139), 1226419–1226419.

(28) Jariwala, D.; Sangwan, V. K.; Lauhon, L. J.; Marks, T. J.; Hersam, M. C. Emerging Device Applications for Semiconducting Two-Dimensional Transition Metal Dichalcogenides. *ACS Nano* **2014**, *8* (2), 1102–1120.

(29) Shi, Y.; Li, H.; Li, L. Recent Advances in Controlled Synthesis of Two-Dimensional Transition Metal Dichalcogenides via Vapour Deposition Techniques. *Chem. Soc. Rev.* **2015**, *44* (9), 2744–2756.

(30) Mata, M. de la; Zhou, X.; Furtmayr, F.; Teubert, J.; Gradečak, S.; Eickhoff, M.; Fontcuberta i Morral, A.; Arbiol, J. A Review of MBE Grown 0D, 1D and 2D Quantum Structures in a Nanowire. *J. Mater. Chem. C* **2013**, *1* (28), 4300.

(31) Haynes, C. L.; Van Duyne, R. P. Nanosphere Lithography: A Versatile Nanofabrication Tool for Studies of Size-Dependent Nanoparticle Optics. *J. Phys. Chem. B* **2001**, *105* (24), 5599–5611.

(32) Tabor, C.; Qian, W.; El-Sayed, M. A. Dependence of the Threshold Energy of Femtosecond Laser Ejection of Gold Nanoprisms from Quartz Substrates on the Nanoparticle Environment. *J. Phys. Chem. C* **2007**, *111* (25), 8934–8941.

(33) Acharya, S.; Sarma, D. D.; Golan, Y.; Sengupta, S.; Ariga, K. Shape-Dependent Confinement in Ultrasmall Zero-, One-, and Two-Dimensional PbS Nanostructures. *J. Am. Chem. Soc.* **2009**, *131* (32), 11282–11283.

(34) Ostwald, W. Über Die Vermeintliche Isomerie Des Roten Und Gelben Quecksilberoxyds Und Die Oberflächenspannung Fester Körper. *Z. phys. Chem* **1900**, *34*, 495–503.

(35) Mer, V. K. La. Nucleation in Phase Transitions. *Ind. Eng. Chem.* **1952**, *44* (6), 1270–1277.

(36) Becker, R.; Döring, W. Kinetische Behandlung Der Keimbildung in Übersättigten Dämpfen. *Ann. Phys.* **1935**, *416* (8), 719–752.

(37) Polte, J. Fundamental Growth Principles of Colloidal Metal Nanoparticles – a New Perspective. *CrystEngComm* **2015**, *17* (36), 6809–6830.

(38) Gibbs, J. W. On the Equilibrium of Heterogeneous Substances. **1879**.

(39) Turner, S.; Lebedev, O. I.; Shenderova, O.; Vlasov, I. I.; Verbeeck, J.; Van Tendeloo, G. Determination of Size, Morphology, and Nitrogen Impurity Location in Treated Detonation Nanodiamond by Transmission Electron Microscopy. *Adv. Funct. Mater.* **2009**, *19* (13), 2116–2124.

(40) Barmparis, G. D.; Lodziana, Z.; Lopez, N.; Remediakis, I. N. Nanoparticle Shapes by Using Wulff Constructions and First-Principles Calculations. *Beilstein J. Nanotechnol.* **2015**, *6*, 361–368.

(41) Wulff, G. XXV. Zur Frage Der Geschwindigkeit Des Wachsthums Und Der Auflösung Der Krystallflächen. *Zeitschrift für Krist. - Cryst. Mater.* **1901**, *34* (1-6).

(42) Wulff, G. On the Question of Speed of Growth and Dissolution of Crystal Surfaces. *Z. Krist.* **1901**, *34*, 449–530.

(43) Viswanath, B.; Kundu, P.; Halder, A.; Ravishankar, N. Mechanistic Aspects of Shape Selection and Symmetry Breaking during Nanostructure Growth by Wet Chemical Methods. *J. Phys. Chem. C* **2009**, *113* (39), 16866–16883.

(44) de Leeuw, N. H.; Parker, S. C. Surface Structure and Morphology of Calcium Carbonate Polymorphs Calcite, Aragonite, and Vaterite: An Atomistic Approach. *J. Phys. Chem. B* **1998**, *102* (16), 2914–2922.

(45) JONES, B.; RENAUT, R. Morphology and Growth of Aragonite Crystals in Hot-Spring Travertines at Lake Bogoria, Kenya Rift Valley. *Sedimentology* **1996**, *43* (2), 323–340.

(46) Viswanath, B.; Kundu, P.; Mukherjee, B.; Ravishankar, N. Predicting the Growth of Two-Dimensional Nanostructures. *Nanotechnology* **2008**, *19* (19), 195603.

(47) Kang, Y. S.; Risbud, S.; Rabolt, J. F.; Stroeve, P. Synthesis and Characterization of Nanometer-Size Fe 3 O 4 and γ-Fe 2 O 3 Particles. *Chem. Mater.* **1996**, *8* (9), 2209–2211.

(48) Zhang, Q.; Li, N.; Goebl, J.; Lu, Z.; Yin, Y. A Systematic Study of the Synthesis of Silver Nanoplates: Is Citrate a "Magic" Reagent? *J. Am. Chem. Soc.* **2011**, *133* (46), 18931–18939.

(49) Elechiguerra, J. L.; Reyes-Gasga, J.; Yacaman, M. J. The Role of Twinning in Shape Evolution of Anisotropic Noble Metal Nanostructures. *J. Mater. Chem.* **2006**, *16* (40), 3906.

(50) Min, Y.; Moon, G. D.; Kim, C.-E.; Lee, J.-H.; Yang, H.; Soon, A.; Jeong, U. Solution-Based Synthesis of Anisotropic Metal Chalcogenide Nanocrystals and Their Applications. *J. Mater. Chem. C* **2014**, *2* (31), 6222.

(51) Kirkeminde, A.; Ruzicka, B. a; Wang, R.; Puna, S.; Zhao, H.; Ren, S. Synthesis and Optoelectronic Properties of Two-Dimensional FeS 2 Nanoplates. *ACS Appl. Mater. Interfaces* **2012**, *4* (3), 1174–1177.

(52) Li, B.; Huang, L.; Zhong, M.; Wei, Z.; Li, J. Electrical and Magnetic Properties of FeS 2 and CuFeS 2 Nanoplates. *RSC Adv.* **2015**, *5* (111), 91103–91107.

(53) Alloyeau, D.; Dachraoui, W.; Javed, Y.; Belkahla, H.; Wang, G.; Lecoq, H.; Ammar, S.; Ersen, O.; Wisnet, A.; Gazeau, F.; et al. Unravelling Kinetic and Thermodynamic Effects on the Growth of Gold Nanoplates by Liquid Transmission Electron Microscopy. *Nano Lett.* **2015**, *15* (4), 2574–2581.

(54) Lukman, A. I.; Gong, B.; Marjo, C. E.; Roessner, U.; Harris, A. T. Facile Synthesis, Stabilization, and Anti-Bacterial Performance of Discrete Ag Nanoparticles Using Medicago Sativa Seed Exudates. *J. Colloid Interface Sci.* **2011**, *353* (2), 433–444.

(55) Zeng, J.; Xia, X.; Rycenga, M.; Henneghan, P.; Li, Q.; Xia, Y. Successive Deposition of Silver on Silver Nanoplates: Lateral versus Vertical Growth. *Angew. Chemie Int. Ed.* **2011**, *50* (1), 244–249.

(56) Cutler, J. I.; Millstone, J. E.; Hurst, S. J.; Me, G. S.; Mirkin, C. a.; Métraux, G. S.; Cutler, J. I.; Mirkin, C. a. Colloidal Gold and Silver Triangular Nanoprisms. *Small* **2009**, *5* (6), 646–664.

(57) Ah, C. S.; Yun, Y. J.; Park, H. J.; Kim, W.-J.; Ha, D. H.; Yun, W. S. Size-Controlled Synthesis of Machinable Single Crystalline Gold Nanoplates. *Chem. Mater.* **2005**, *17* (22), 5558–5561.

(58) Baletto, F.; Ferrando, R. Structural Properties of Nanoclusters: Energetic, Thermodynamic, and Kinetic Effects. *Rev. Mod. Phys.* **2005**, *77* (1), 371–423.

(59) Personick, M. L.; Mirkin, C. a. Making Sense of the Mayhem behind Shape Control in the Synthesis of Gold Nanoparticles. *J. Am. Chem. Soc.* **2013**, *135* (49), 18238–18247.

(60) Langille, M. R.; Personick, M. L.; Zhang, J.; Mirkin, C. A. Defining Rules for the Shape Evolution of Gold Nanoparticles. *J. Am. Chem. Soc.* **2012**, *134* (35), 14542–14554.

(61) Son, J. S.; Yu, J. H.; Kwon, S. G.; Lee, J.; Joo, J.; Hyeon, T. Colloidal Synthesis of Ultrathin Two-Dimensional Semiconductor Nanocrystals. *Adv. Mater.* **2011**, *23* (28), 3214–3219.

(62) Personick, M. L.; Langille, M. R.; Zhang, J.; Mirkin, C. a. Shape Control of Gold Nanoparticles by Silver Underpotential Deposition. *Nano Lett.* **2011**, *11* (8), 3394–3398.

(63) Son, J. S.; Wen, X.-D.; Joo, J.; Chae, J.; Baek, S.; Park, K.; Kim, J. H.; An, K.; Yu, J. H.; Kwon, S. G.; et al. Large-Scale Soft Colloidal Template Synthesis of 1.4 Nm Thick CdSe Nanosheets. *Angew. Chemie Int. Ed.* **2009**, *48* (37), 6861–6864.

(64) Li, Z.; Peng, X. Size/Shape-Controlled Synthesis of Colloidal CdSe Quantum Disks: Ligand and Temperature Effects. *J. Am. Chem. Soc.* **2011**, *133* (17), 6578–6586.

(65) Yu, W. W.; Wang, Y. A.; Peng, X. Formation and Stability of Size-, Shape-, and Structure-Controlled CdTe Nanocrystals: Ligand Effects on Monomers and Nanocrystals. *Chem. Mater.* **2003**, *15* (22), 4300–4308.

(66) Peng, X.; Manna, L.; Yang, W.; Wickham, J.; Scher, E.; Kadavanich, A.; Alivisatos, A. Shape Control of CdSe Nanocrystals. *Nature* **2000**, *404* (6773), 59–61.

(67) Milliron, D. J.; Hughes, S. M.; Cui, Y.; Manna, L.; Li, J.; Wang, L. W.; Alivisatos, A. P. Colloidal Nanocrystal Heterostructures with Linear and Branched Topology. *Nature* **2004**, *430* (6996), 190–195.

(68) Cheng, Y.; Wang, Y.; Bao, F.; Chen, D. Shape Control of Monodisperse CdS Nanocrystals: Hexagon and Pyramid. *J. Phys. Chem. B* **2006**, *110* (19), 9448–9451.

(69) Cassette, E.; Mahler, B.; Guigner, J.-M.; Patriarche, G.; Dubertret, B.; Pons, T. Colloidal CdSe/CdS Dot-in-Plate Nanocrystals with 2D-Polarized Emission. *ACS Nano* **2012**, *6* (8), 6741–6750.

(70) Chen, C.-C.; Lin, J.-J. Controlled Growth of Cubic Cadmium Sulfide Nanoparticles Using Patterned Self-Assembled Monolayers as a Template. *Adv. Mater.* **2001**, *13* (2), 136–139.

(71) Pileni, M.-P. The Role of Soft Colloidal Templates in Controlling the Size and Shape of Inorganic Nanocrystals. *Nat. Mater.* **2003**, *2* (3), 145–150.

(72) Barman, S.; Vasudevan, S. Contrasting Melting Behavior of Zinc Stearate and Zinc Oleate. *J. Phys. Chem. B* **2006**, *110* (2), 651–654.

(73) Bakshi, M. S.; Possmayer, F.; Petersen, N. O. Aqueous-Phase Room-Temperature Synthesis of Gold Nanoribbons: Soft Template Effect of a Gemini Surfactant. *J. Phys. Chem. C* **2008**, *112* (22), 8259–8265.

(74) Penn, R. L. Imperfect Oriented Attachment: Dislocation Generation in Defect-Free Nanocrystals. *Science (80-.).* **1998**, *281* (5379), 969–971.

(75) Zhang, J.; Lin, Z.; Lan, Y.; Ren, G.; Chen, D.; Huang, F.; Hong, M. A Multistep Oriented Attachment Kinetics: Coarsening of ZnS Nanoparticle in Concentrated NaOH. *J. Am. Chem. Soc.* **2006**, *128* (39), 12981–12987.

(76) Penn, R. L.; Banfield, J. F. Oriented Attachment and Growth, Twinning, Polytypism, and

Formation of Metastable Phases: Insights from Nanocrystalline TiO2. *Am. Miner.* **1998**, *83* (9-10), 1077–1082.

(77) Zhang, J.; Huang, F.; Lin, Z. Progress of Nanocrystalline Growth Kinetics Based on Oriented Attachment. *Nanoscale* **2010**, *2* (1), 18–34.

(78) Li, D.; Nielsen, M. H.; Lee, J. R. I.; Frandsen, C.; Banfield, J. F.; De Yoreo, J. J. Direction-Specific Interactions Control Crystal Growth by Oriented Attachment. *Science (80-.).* **2012**, *336* (6084), 1014–1018.

(79) Han, J. H.; Lee, S.; Cheon, J. Synthesis and Structural Transformations of Colloidal 2D Layered Metal Chalcogenide Nanocrystals. *Chem. Soc. Rev.* **2013**, *42* (7), 2581–2591.

(80) Wilson, J. A.; Yoffe, A. D. The Transition Metal Dichalcogenides Discussion and Interpretation of the Observed Optical, Electrical and Structural Properties. *Adv. Phys.* **1969**, *18* (73), 193–335.

(81) Hulliger, F. *Structural Chemistry of Layer-Type Phases*; Springer Science & Business Media, 2012; Vol. 5.

(82) Xu, F.; Guo, C.; Sun, Y.; Liu, Z.; Zhang, Y.; Li, Z. Facile Fabrication of Single Crystal Gold Nanoplates with Micrometer Lateral Size. *Colloids Surfaces A Physicochem. Eng. Asp.* **2010**, *353* (2-3), 125–131.

(83) Mottet, C.; Goniakowski, J.; Baletto, F.; Ferrando, R.; Treglia, G. Modeling Free and Supported Metallic Nanoclusters: Structure and Dynamics. *Phase Transitions* **2004**, *77* (1-2), 101–113.

(84) Swaminarayan, S.; Najafabadi, R.; Srolovitz, D. J. Polycrystalline Surface Properties from Spherical Crystallites: Ag, Au, Cu and Pt. *Surf. Sci.* **1994**, *306* (3), 367–380.

(85) Sau, T. K.; Rogach, A. L. Nonspherical Noble Metal Nanoparticles: Colloid-Chemical Synthesis and Morphology Control. *Adv. Mater.* **2010**, *22* (16), 1781–1804.

(86) Sansoz, F.; Huang, H.; Warner, D. H. An Atomistic Perspective on Twinning Phenomena in Nano-Enhanced Fcc Metals. *JOM* **2008**, *60* (9), 79–84.

(87) Zhan, G.; Ke, L.; Li, Q.; Huang, J.; Hua, D.; Ibrahim, A.-R.; Sun, D. Synthesis of Gold Nanoplates with Bioreducing Agent Using Syringe Pumps: A Kinetic Control. *Ind. Eng. Chem. Res.* **2012**, *51* (48), 15753–15762.

(88) Lofton, C.; Sigmund, W. Mechanisms Controlling Crystal Habits of Gold and Silver Colloids. *Adv. Funct. Mater.* **2005**, *15* (7), 1197–1208.

(89) Evans, J. S.; Beier, C. N.; Smalyukh, I. I. Alignment of High-Aspect Ratio Colloidal Gold Nanoplatelets in Nematic Liquid Crystals. *J. Appl. Phys.* **2011**, *110* (3), 033535.

(90) Baletto, F.; Mottet, C.; Ferrando, R. Microscopic Mechanisms of the Growth of Metastable Silver Icosahedra. *Phys. Rev. B* **2001**, *63* (15), 155408.

(91) José-Yacaman, M.; Pérez-Tijerina, E.; Mejia-Rosales, S.; Jose, M. Defect Structure in Nanoalloys. *J. Mater. Chem.* **2007**, *17* (11), 1035.

(92) Baletto, F.; Mottet, C.; Ferrando, R. Reentrant Morphology Transition in the Growth of Free Silver Nanoclusters. *Phys. Rev. Lett.* **2000**, *84* (24), 5544–5547.

(93) Reinhard, D.; Hall, B. D.; Berthoud, P.; Valkealahti, S.; Monot, R. Size-Dependent Icosahedral-to-Fcc Structure Change Confirmed in Unsupported Nanometer-Sized Copper Clusters. *Phys. Rev. Lett.* **1997**, *79* (8), 1459–1462.

(94) Baletto, F.; Mottet, C.; Ferrando, R. Freezing of Silver Nanodroplets. *Chem. Phys. Lett.* **2002**, *354* (1-2), 82–87.

(95) Sun, J.; Guan, M.; Shang, T.; Gao, C.; Xu, Z.; Zhu, J. Selective Synthesis of Gold Cuboid and Decahedral Nanoparticles Regulated and Controlled by Cu 2+ Ions. *Cryst. Growth Des.* **2008**, *8* (3), 906–910.

(96) Chen, L.; Ji, F.; Xu, Y.; He, L.; Mi, Y.; Bao, F.; Sun, B.; Zhang, X.; Zhang, Q. High-Yield Seedless Synthesis of Triangular Gold Nanoplates through Oxidative Etching. *Nano Lett.* **2014**, *14* (12), 7201–7206.

(97) Lee, C.-L.; Syu, C.-M.; Chiou, H.-P.; Chen, C.-H.; Yang, H.-L. High-Yield, Size-Controlled Synthesis of Silver Nanoplates and Their Applications as Methanol-Tolerant Electrocatalysts in Oxygen Reduction Reaction. *Int. J. Hydrogen Energy* **2011**, *36* (17), 10502–10512.

(98) Millstone, J. E.; Wei, W.; Jones, M. R.; Yoo, H.; Mirkin, C. a. Iodide Ions Control Seed-Mediated Growth of Anisotropic Gold Nanoparticles. *Nano Lett.* **2008**, *8* (8), 2526–2529.

(99) Métraux, G. S.; Mirkin, C. a. Rapid Thermal Synthesis of Silver Nanoprisms with Chemically Tailorable Thickness. *Adv. Mater.* **2005**, *17* (4), 412–415.

(100) Weiss, J. The Catalytic Decomposition of Hydrogen Peroxide on Different Metals. *Trans. Faraday Soc.* **1935**, *31* (C), 1547.

(101) Yu, H.; Zhang, Q.; Liu, H.; Dahl, M.; Joo, J. B.; Li, N.; Wang, L.; Yin, Y. Thermal Synthesis of Silver Nanoplates Revisited : A Modified Photochemical Process. *ACS Nano* **2014**, *8* (10), 10252–10261.

(102) Wiley, B.; Herricks, T.; Sun, Y.; Xia, Y. Polyol Synthesis of Silver Nanoparticles: Use of Chloride and Oxygen to Promote the Formation of Single-Crystal, Truncated Cubes and Tetrahedrons. *Nano Lett.* **2004**, *4* (9), 1733–1739.

(103) Wiley, B. J.; Xiong, Y.; Li, Z.-Y.; Yin, Y.; Xia, Y. Right Bipyramids of Silver: A New Shape Derived from Single Twinned Seeds. *Nano Lett.* **2006**, *6* (4), 765–768.

(104) Wiley, B. J.; Chen, Y.; McLellan, J. M.; Xiong, Y.; Li, Z.-Y.; Ginger, D.; Xia, Y. Synthesis and Optical Properties of Silver Nanobars and Nanorice. *Nano Lett.* **2007**, *7* (4), 1032–1036.

(105) Wiley, B.; Sun, Y.; Xia, Y. Polyol Synthesis of Silver Nanostructures: Control of Product Morphology with Fe(II) or Fe(III) Species. *Langmuir* **2005**, *21* (18), 8077–8080.

(106) Xiong, Y.; Chen, J.; Wiley, B.; Xia, Y.; Aloni, S.; Yin, Y. Understanding the Role of Oxidative Etching in the Polyol Synthesis of Pd Nanoparticles with Uniform Shape and Size. *J. Am. Chem. Soc.* **2005**, *127* (20), 7332–7333.

(107) Xiong, Y.; McLellan, J. M.; Yin, Y.; Xia, Y. Synthesis of Palladium Icosahedra with Twinned Structure by Blocking Oxidative Etching with Citric Acid or Citrate Ions. *Angew. Chemie Int. Ed.* **2007**, *46* (5), 790–794.

(108) Ha, T. H.; Koo, H.; Chung, B. H. Shape-Controlled Syntheses of Gold Nanoprisms and

Nanorods Influenced by Specific Adsorption of Halide Ions. *J. Phys. Chem. C* **2007**, *111* (3), 1123–1130.

(109) Magnussen, O. M. Ordered Anion Adlayers on Metal Electrode Surfaces. *Chem. Rev.* **2002**, *102* (3), 679–726.

(110) Bard, A. J.; Parsons, R.; Jordan, J. *Standard Potentials in Aqueous Solution*; CRC press, 1985; Vol. 6.

(111) Jana, N. R.; Gearheart, L.; Murphy, C. J. Seed-Mediated Growth Approach for Shape-Controlled Synthesis of Spheroidal and Rod-like Gold Nanoparticles Using a Surfactant Template. *Adv. Mater.* **2001**, *13* (18), 1389–1393.

(112) Liu; Guyot-Sionnest, P. Mechanism of Silver(I)-Assisted Growth of Gold Nanorods and Bipyramids. *J. Phys. Chem. B* **2005**, *109* (47), 22192–22200.

(113) Ling, T.; Wang, J.-J.; Zhang, H.; Song, S.-T.; Zhou, Y.-Z.; Zhao, J.; Du, X.-W. Freestanding Ultrathin Metallic Nanosheets: Materials, Synthesis, and Applications. *Adv. Mater.* **2015**, *27* (36), 5396–5402.

(114) Huang, X.; Tang, S.; Mu, X.; Dai, Y.; Chen, G.; Zhou, Z.; Ruan, F.; Yang, Z.; Zheng, N. Freestanding Palladium Nanosheets with Plasmonic and Catalytic Properties. *Nat. Nanotechnol.* **2011**, *6* (1), 28–32.

(115) Peng, Z. A.; Peng, X. Nearly Monodisperse and Shape-Controlled CdSe Nanocrystals via Alternative Routes: Nucleation and Growth. *J. Am. Chem. Soc.* **2002**, *124* (13), 3343–3353.

(116) Kumar, S.; Nann, T. Shape Control of II–VI Semiconductor Nanomaterials. *Small* **2006**, *2* (3), 316–329.

(117) Liu, Y.-H.; Wayman, V. L.; Gibbons, P. C.; Loomis, R. a.; Buhro, W. E. Origin of High Photoluminescence Efficiencies in CdSe Quantum Belts. *Nano Lett.* **2010**, *10* (1), 352–357.

(118) Liu, Y.-H. H.; Wang, F.; Wang, Y.; Gibbons, P. C.; Buhro, W. E. Lamellar Assembly of Cadmium Selenide Nanoclusters into Quantum Belts. *J. Am. Chem. Soc.* **2011**, *133* (42), 17005–17013.

(119) Son, J. S.; Park, K.; Kwon, S. G.; Yang, J.; Choi, M. K.; Kim, J.; Yu, J. H.; Joo, J.; Hyeon, T. Dimension-Controlled Synthesis of CdS Nanocrystals: From 0D Quantum Dots to 2D Nanoplates. *Small* **2012**, *8* (15), 2394–2402.

(120) Wang, Y.; Zhou, Y.; Zhang, Y.; Buhro, W. E. Magic-Size II–VI Nanoclusters as Synthons for Flat Colloidal Nanocrystals. *Inorg. Chem.* **2015**, *54* (3), 1165–1177.

(121) Buffard, A.; Nadal, B.; Heuclin, H.; Patriarche, G.; Dubertret, B. ZnS Anisotropic Nanocrystals Using a One-Pot Low Temperature Synthesis. *New J. Chem.* **2015**, *39* (1), 90–93.

(122) Du, Y.; Yin, Z.; Zhu, J.; Huang, X.; Wu, X.-J.; Zeng, Z.; Yan, Q.; Zhang, H. A General Method for the Large-Scale Synthesis of Uniform Ultrathin Metal Sulphide Nanocrystals. *Nat. Commun.* **2012**, *3*, 1177.

(123) Wang, Y.; Liu, Y.-H.; Zhang, Y.; Kowalski, P. J.; Rohrs, H. W.; Buhro, W. E. Preparation of

Primary Amine Derivatives of the Magic-Size Nanocluster (CdSe) 13. *Inorg. Chem.* **2013**, *52* (6), 2933–2938.

(124) Wang, Y.; Zhang, Y.; Wang, F.; Giblin, D. E.; Hoy, J.; Rohrs, H. W.; Loomis, R. a; Buhro, W. E. The Magic-Size Nanocluster (CdSe) 34 as a Low-Temperature Nucleant for Cadmium Selenide Nanocrystals; Room-Temperature Growth of Crystalline Quantum Platelets. *Chem. Mater.* **2014**, *26* (7), 2233–2243.

(125) Wang, F.; Wang, Y.; Liu, Y.; Morrison, P. J.; Loomis, R. a.; Buhro, W. E. Two-Dimensional Semiconductor Nanocrystals: Properties, Templated Formation, and Magic-Size Nanocluster Intermediates. *Acc. Chem. Res.* **2015**, *48* (1), 13–21.

(126) Yu, T.; Moon, J.; Park, J.; Park, Y. Il; Na, H. Bin; Kim, B. H.; Song, I. C.; Moon, W. K.; Hyeon, T. Various-Shaped Uniform Mn 3 O 4 Nanocrystals Synthesized at Low Temperature in Air Atmosphere. *Chem. Mater.* **2009**, *21* (11), 2272–2279.

(127) Yang, J.; Son, J. S.; Yu, J. H.; Joo, J.; Hyeon, T. Advances in the Colloidal Synthesis of Two-Dimensional Semiconductor Nanoribbons. *Chem. Mater.* **2013**, *25* (8), 1190–1198.

(128) Yu, J. H.; Liu, X.; Kweon, K. E.; Joo, J.; Park, J.; Ko, K.-T.; Lee, D. W.; Shen, S.; Tivakornsasithorn, K.; Son, J. S.; et al. Giant Zeeman Splitting in Nucleation-Controlled Doped CdSe:Mn2+ Quantum Nanoribbons. *Nat. Mater.* **2010**, *9* (1), 47–53.

(129) Zhang, J.; Rowland, C.; Liu, Y.; Xiong, H.; Kwon, S.; Shevchenko, E.; Schaller, R. D.; Prakapenka, V. B.; Tkachev, S.; Rajh, T. Evolution of Self-Assembled ZnTe Magic-Sized Nanoclusters. *J. Am. Chem. Soc.* **2015**, *137* (2), 742–749.

(130) Ithurria, S.; Bousquet, G.; Dubertret, B. Continuous Transition from 3D to 1D Confinement Observed during the Formation of CdSe Nanoplatelets. *J. Am. Chem. Soc.* **2011**, *133* (9), 3070–3077.

(131) Lhuillier, E.; Pedetti, S.; Ithurria, S.; Nadal, B.; Heuclin, H.; Dubertret, B. Two-Dimensional Colloidal Metal Chalcogenides Semiconductors: Synthesis, Spectroscopy, and Applications. *Acc. Chem. Res.* **2015**, *48* (1), 22–30.

(132) Bouet, C.; Mahler, B.; Nadal, B.; Abecassis, B.; Tessier, M. D.; Ithurria, S.; Xu, X.; Dubertret, B. Two-Dimensional Growth of CdSe Nanocrystals, from Nanoplatelets to Nanosheets. *Chem. Mater.* **2013**, *25* (4), 639–645.

(133) Sokolikova, M. S.; Vasiliev, R. B.; Gaskov, a. M. Synthesis of Quasi-Two-Dimensional Colloidal Cadmium Selenide Nanoparticles and Formation of Sulfide Monolayer on Their Surfaces. *Russ. J. Inorg. Chem.* **2014**, *59* (5), 413–418.

(134) Tessier, M. D.; Biadala, L.; Bouet, C.; Ithurria, S.; Abecassis, B.; Dubertret, B. Phonon Line Emission Revealed by Self-Assembly of Colloidal Nanoplatelets. *ACS Nano* **2013**, *7* (4), 3332–3340.

(135) Jana, S.; Phan, T. N. T.; Bouet, C.; Tessier, M. D.; Davidson, P.; Dubertret, B.; Abécassis, B. Stacking and Colloidal Stability of CdSe Nanoplatelets. *Langmuir* **2015**, *31* (38), 10532–10539.

(136) Abécassis, B.; Tessier, M. D.; Davidson, P.; Dubertret, B. Self-Assembly of CdSe Nanoplatelets into Giant Micrometer-Scale Needles Emitting Polarized Light. *Nano Lett.* **2014**, *14* (2), 710–715.

(137) Hutter, E. M.; Bladt, E.; Goris, B.; Pietra, F.; van der Bok, J. C.; Boneschanscher, M. P.; de Mello Donegá, C.; Bals, S.; Vanmaekelbergh, D. Conformal and Atomic Characterization of Ultrathin CdSe Platelets with a Helical Shape. *Nano Lett.* **2014**, *14* (11), 6257–6262.

(138) Lhuillier, E.; Hease, P.; Ithurria, S.; Dubertret, B. Selective Electrophoretic Deposition of CdSe Nanoplatelets. *Chem. Mater.* **2014**, *26* (15), 4514–4520.

(139) Tessier, M. D.; Javaux, C.; Maksimovic, I.; Loriette, V.; Dubertret, B. Spectroscopy of Single CdSe Nanoplatelets. *ACS Nano* **2012**, *6* (8), 6751–6758.

(140) Ithurria, S.; Tessier, M. D.; Mahler, B.; Lobo, R. P. S. M.; Dubertret, B.; Efros, A. L. Colloidal Nanoplatelets with Two-Dimensional Electronic Structure. *Nat. Mater.* **2011**, *10* (12), 936–941.

(141) Yeltik, A.; Delikanli, S.; Olutas, M.; Kelestemur, Y.; Guzelturk, B.; Demir, H. V. Experimental Determination of the Absorption Cross-Section and Molar Extinction Coefficient of Colloidal CdSe Nanoplatelets. *J. Phys. Chem. C* **2015**, acs.jpcc.5b09275.

(142) Pedetti, S.; Nadal, B.; Lhuillier, E.; Mahler, B.; Bouet, C.; Abécassis, B.; Xu, X.; Dubertret, B. Optimized Synthesis of CdTe Nanoplatelets and Photoresponse of CdTe Nanoplatelets Films. *Chem. Mater.* **2013**, *25* (12), 2455–2462.

(143) Lyashchova, A.; Dmytruk, A.; Dmitruk, I.; Klimusheva, G.; Mirnaya, T.; Asaula, V. Optical Absorption, Induced Bleaching, and Photoluminescence of CdSe Nanoplatelets Grown in Cadmium Octanoate Matrix. *Nanoscale Res. Lett.* **2014**, *9* (1), 88.

(144) Li, Z.; Qin, H.; Guzun, D.; Benamara, M.; Salamo, G.; Peng, X. Uniform Thickness and Colloidal-Stable CdS Quantum Disks with Tunable Thickness: Synthesis and Properties. *Nano Res.* **2012**, *5* (5), 337–351.

(145) Liu, L.; Zhuang, Z.; Xie, T.; Wang, Y.; Li, J.; Peng, Q.; Li, Y. Shape Control of CdSe Nanocrystals with Zinc Blende Structure. *J. Am. Chem. Soc.* **2009**, *131* (45), 16423–16429.

(146) Hines, M. a.; Guyot-Sionnest, P. Synthesis and Characterization of Strongly Luminescing ZnS-Capped CdSe Nanocrystals. *J. Phys. Chem.* **1996**, *100* (2), 468–471.

(147) Mahler, B.; Nadal, B.; Bouet, C.; Patriarche, G.; Dubertret, B. Core/Shell Colloidal Semiconductor Nanoplatelets. *J. Am. Chem. Soc.* **2012**, *134* (45), 18591–18598.

(148) Tessier, M. D.; Mahler, B.; Nadal, B.; Heuclin, H.; Pedetti, S.; Dubertret, B. Spectroscopy of Colloidal Semiconductor Core/shell Nanoplatelets with High Quantum Yield. *Nano Lett.* **2013**, *13* (7), 3321–3328.

(149) Li, J. J.; Wang, Y. A.; Guo, W.; Keay, J. C.; Mishima, T. D.; Johnson, M. B.; Peng, X. Large-Scale Synthesis of Nearly Monodisperse CdSe/CdS Core/shell Nanocrystals Using Air-Stable Reagents via Successive Ion Layer Adsorption and Reaction. *J. Am. Chem. Soc.* **2003**, *125* (41), 12567–12575.

(150) Ithurria, S.; Talapin, D. V. Colloidal Atomic Layer Deposition (c-ALD) Using Self-Limiting Reactions at Nanocrystal Surface Coupled to Phase Transfer between Polar and Nonpolar Media. *J. Am. Chem. Soc.* **2012**, *134* (45), 18585–18590.

(151) Jeong, K. S.; Deng, Z.; Keuleyan, S.; Liu, H.; Guyot-Sionnest, P. Air-Stable N-Doped

Colloidal HgS Quantum Dots. *J. Phys. Chem. Lett.* **2014**, *5* (7), 1139–1143.

(152) Oh, S. J.; Berry, N. E.; Choi, J. H.; Gaulding, E. A.; Paik, T.; Hong, S. H.; Murray, C. B.; Kagan, C. R. Stoichiometric Control of Lead Chalcogenide Nanocrystal Solids to Enhance Their Electronic and Optoelectronic Device Performance. *ACS Nano* **2013**, *7* (3), 2413–2421.

(153) Lhuillier, E.; Pedetti, S.; Ithurria, S.; Heuclin, H.; Nadal, B.; Robin, A.; Patriarche, G.; Lequeux, N.; Dubertret, B. Electrolyte-Gated Field Effect Transistor to Probe the Surface Defects and Morphology in Films of Thick CdSe Colloidal Nanoplatelets. *ACS Nano* **2014**, *8* (4), 3813–3820.

(154) Tessier, M. D.; Spinicelli, P.; Dupont, D.; Patriarche, G.; Ithurria, S.; Dubertret, B. Efficient Exciton Concentrators Built from Colloidal Core/crown CdSe/CdS Semiconductor Nanoplatelets. *Nano Lett.* **2014**, *14* (1), 207–213.

(155) Pedetti, S.; Ithurria, S.; Heuclin, H.; Patriarche, G.; Dubertret, B. Type-II CdSe/CdTe Core/Crown Semiconductor Nanoplatelets. *J. Am. Chem. Soc.* **2014**, *136* (46), 16430–16438.

(156) Prudnikau, A.; Chuvilin, A.; Artemyev, M. CdSe-CdS Nanoheteroplatelets with Efficient Photoexcitation of Central CdSe Region through Epitaxially Grown CdS Wings. *J. Am. Chem. Soc.* **2013**, *135* (39), 14476–14479.

(157) Kelestemur, Y.; Olutas, M.; Delikanli, S.; Guzelturk, B.; Akgul, M. Z.; Demir, H. V. Type-II Colloidal Quantum Wells: CdSe/CdTe Core/Crown Heteronanoplatelets. *J. Phys. Chem. C* **2015**, 150105110413000.

(158) Maiti, P. S.; Houben, L.; Bar-Sadan, M. Growth Schemes of Tunable Ultrathin CdS X Se 1– X Alloyed Nanostructures at Low Temperatures. *J. Phys. Chem. C* **2015**, *119* (19), 10734–10739.

(159) Fan, F.; Kanjanaboos, P.; Saravanapavanantham, M.; Beauregard, E.; Ingram, G.; Yassitepe, E.; Adachi, M. M.; Voznyy, O.; Johnston, A. K.; Walters, G.; et al. Colloidal CdSe 1– X S X Nanoplatelets with Narrow and Continuously-Tunable Electroluminescence. *Nano Lett.* **2015**, *15* (7), 4611–4615.

(160) Sokolikova, M. S.; Shlenskaya, N. N.; Kozlovskii, V. F.; Vasiliev, R. B.; Gaskov, A. M. Synthesis and Optical Properties of Quasi-2D CdS X Se1 − X Nanoparticles. *Russ. J. Inorg. Chem.* **2014**, *59* (10), 1069–1072.

(161) Tenne, R.; Pedetti, S.; Kazes, M.; Ithurria, S.; Houben, L.; Nadal, B.; Oron, D.; Dubertret, B. Submitted. *Submitted*.

(162) Hutter, E. M.; Pietra, F.; Van Dijk - Moes, R. J. a; Mitoraj, D.; Meeldijk, J. D.; De Mello Donegá, C.; Vanmaekelbergh, D. Method to Incorporate Anisotropic Semiconductor Nanocrystals of All Shapes in an Ultrathin and Uniform Silica Shell. *Chem. Mater.* **2014**, *26*, 1905–1911.

(163) Ji, B.; Giovanelli, E.; Habert, B.; Spinicelli, P.; Nasilowski, M.; Xu, X.; Lequeux, N.; Hugonin, J.-P.; Marquier, F.; Greffet, J.-J.; et al. Non-Blinking Quantum Dot with a Plasmonic Nanoshell Resonator. *Nat. Nanotechnol.* **2015**, *10* (January), 1–6.

(164) Naskar, S.; Schlosser, A.; Miethe, J. F.; Steinbach, F.; Feldho, A.; Bigall, N. C.; Feldhoff,

A.; Bigall, N. C. Site-Selective Noble Metal Growth on CdSe Nanoplatelets. *Chem. Mater.* **2015**, 150416150344005.

(165) Sheldon, M. T.; Trudeau, P. E.; Mokari, T.; Wang, L. W.; Paul Alivisatos, a. Enhanced Semiconductor Nanocrystal Conductance via Solution Grown Contacts. *Nano Lett.* **2009**, *9* (11), 3676–3682.

(166) Steiner, D.; Mokari, T.; Banin, U.; Millo, O. Electronic Structure of Metal-Semiconductor Nanojunctions in Gold CdSe Nanodumbbells. *Phys. Rev. Lett.* **2005**, *95* (5), 2–5.

(167) Zhukovskyi, M.; Tongying, P.; Yashan, H.; Wang, Y.; Kuno, M. Efficient Photocatalytic Hydrogen Generation from Ni Nanoparticle Decorated CdS Nanosheets. *ACS Catal.* **2015**, 6615–6623.

(168) Mokari, T.; Sztrum, C. G.; Salant, A.; Rabani, E.; Banin, U. Formation of Asymmetric One-Sided Metal-Tipped Semiconductor Nanocrystal Dots and Rods. *Nat. Mater.* **2005**, *4* (11), 855–863.

(169) Mokari, T.; Rothenberg, E.; Popov, I.; Costi, R. Onto Semiconductor Quantum Rods and Tetrapods. **2004**, *304* (June), 1787–1790.

(170) Kotov, N. A.; Weiss, P. S. Self-Assembly of Nanoparticles: A Snapshot. *ACS Nano* **2014**, *8* (4), 3101–3103.

(171) Acharya, S.; Das, B.; Thupakula, U.; Ariga, K.; Sarma, D. D.; Israelachvili, J.; Golan, Y. A Bottom-Up Approach toward Fabrication of Ultrathin PbS Sheets. *Nano Lett.* **2013**, *13* (2), 409–415.

(172) Nagel, M.; Hickey, S. G.; Frömsdorf, a.; Kornowski, a.; Weller, H. Synthesis of Monodisperse PbS Nanoparticles and Their Assembly into Highly Ordered 3D Colloidal Crystals. *Zeitschrift für Phys. Chemie* **2007**, *221* (3), 427–437.

(173) Abécassis, B. Three-Dimensional Self Assembly of Semiconducting Colloidal Nanocrystals: From Fundamental Forces to Collective Optical Properties. *ChemPhysChem* **2015**, n/a – n/a.

(174) Murray, C. B.; Kagan, C. R.; Bawendi, M. G. Self-Organization of CdSe Nanocrystallites into Three-Dimensional Quantum Dot Superlattices. *Science (80-.).* **1995**, *270* (5240), 1335–1338.

(175) Bielewicz, T.; Ramin Moayed, M. M.; Lebedeva, V.; Strelow, C.; Rieckmann, A.; Klinke, C. From Dots to Stripes to Sheets: Shape Control of Lead Sulfide Nanostructures. *Chem. Mater.* **2015**, acs.chemmater.5b03088.

(176) Wang, Z.; Schliehe, C.; Bian, K.; Dale, D.; Bassett, W. a.; Hanrath, T.; Klinke, C.; Weller, H. Correlating Superlattice Polymorphs to Internanoparticle Distance, Packing Density, and Surface Lattice in Assemblies of PbS Nanoparticles. *Nano Lett.* **2013**, *13* (3), 1303–1311.

(177) Koh, W.; Saudari, S. R.; Fafarman, A. T.; Kagan, C. R.; Murray, C. B. Thiocyanate-Capped PbS Nanocubes: Ambipolar Transport Enables Quantum Dot Based Circuits on a Flexible Substrate. *Nano Lett.* **2011**, *11* (11), 4764–4767.

(178) Cho, K. S.; Talapin, D. V.; Gaschler, W.; Murray, C. B. Designing PbSe Nanowires and Nanorings through Oriented Attachment of Nanoparticles. *J. Am. Chem. Soc.* **2005**, *127*

(19), 7140–7147.

(179) Gerdes, F.; Volkmann, M.; Schliehe, C.; Bielewicz, T.; Klinke, C. Sculpting of Lead Sulfide Nanoparticles by Means of Acetic Acid and Dichloroethane. *Zeitschrift für Phys. Chemie* **2015**, *229* (1-2), 139–151.

(180) Schliehe, C.; Juarez, B. H.; Pelletier, M.; Jander, S.; Greshnykh, D.; Nagel, M.; Meyer, A.; Foerster, S.; Kornowski, A.; Klinke, C.; et al. Ultrathin PbS Sheets by Two-Dimensional Oriented Attachment. *Science (80-.).* **2010**, *329* (5991), 550–553.

(181) Loc, W. S.; Quan, Z.; Lin, C.; Pan, J.; Wang, Y.; Yang, K.; Jian, W.-B.; Zhao, B.; Wang, H.; Fang, J. Facet-Controlled Facilitation of PbS Nanoarchitectures by Understanding Nanocrystal Growth. *Nanoscale* **2015**, *7* (45), 19047–19052.

(182) Bielewicz, T.; Dogan, S.; Klinke, C. Tailoring the Height of Ultrathin PbS Nanosheets and Their Application as Field-Effect Transistors. *Small* **2015**, *11* (7), 826–833.

(183) Lohse, S. E.; Burrows, N. D.; Scarabelli, L.; Liz-Marzán, L. M.; Murphy, C. J. Anisotropic Noble Metal Nanocrystal Growth: The Role of Halides. *Chem. Mater.* **2014**, *26* (1), 34–43.

(184) Dogan, S.; Bielewicz, T.; Cai, Y.; Klinke, C. Field–effect Transistors Made of Individual Colloidal PbS Nanosheets. *Appl. Phys. Lett.* **2012**, *101* (7), 073102.

(185) Fang, Z.; Wang, Q.; Wang, X.; Zhu, B.; Fan, F.; Wang, C.; Liu, X. Ethylenediamine Inducing Growth of {100} Facets Exposed PbS Nanosheets. *Cryst. Res. Technol.* **2012**, *47* (6), 635–642.

(186) Jiang, Z.; Bhandari, G. B.; Prematilaka, S. M.; Khan, S.; Dimick, D. M.; Stombaugh, C.; Mandell, A.; He, Y.; Peter Lu, H.; Sun, L. Growth of Colloidal PbS Nanosheets and the Enhancement of Their Photoluminescence. *Phys. Chem. Chem. Phys.* **2015**, *17* (36), 23303–23307.

(187) Zhang, H.; Savitzky, B. H.; Yang, J.; Newman, J. T.; Perez, K. A.; Hyun, B.-R.; Kourkoutis, L. F.; Hanrath, T.; Wise, F. W. Colloidal Synthesis of PbS and PbS/CdS Nanosheets Using Acetate-Free Precursors. *Chem. Mater.* **2015**, acs.chemmater.5b03348.

(188) Dogan, S.; Bielewicz, T.; Lebedeva, V.; Klinke, C. Photovoltaic Effect in Individual Asymmetrically Contacted Lead Sulfide Nanosheets. *Nanoscale* **2015**, *7* (11), 4875–4883.

(189) Aerts, M.; Bielewicz, T.; Klinke, C.; Grozema, F. C.; Houtepen, A. J.; Schins, J. M.; Siebbeles, L. D. a. Highly Efficient Carrier Multiplication in PbS Nanosheets. *Nat. Commun.* **2014**, *5*, 3789.

(190) Evers, W. H.; Goris, B.; Bals, S.; Casavola, M.; de Graaf, J.; Roij, R. Van; Dijkstra, M.; Vanmaekelbergh, D. Low-Dimensional Semiconductor Superlattices Formed by Geometric Control over Nanocrystal Attachment. *Nano Lett.* **2013**, *13* (6), 2317–2323.

(191) Baumgardner, W. J.; Whitham, K.; Hanrath, T. Confined-but-Connected Quantum Solids via Controlled Ligand Displacement. *Nano Lett.* **2013**, *13* (7), 3225–3231.

(192) Delerue, C. From Semiconductor Nanocrystals to Artificial Solids with Dimensionality below Two. *Phys. Chem. Chem. Phys.* **2014**, *16* (47), 25734–25740.

(193) Nag, A.; Kovalenko, M. V; Lee, J. S.; Liu, W.; Spokoyny, B.; Talapin, D. V. Metal-Free Inorganic Ligands for Colloidal Nanocrystals: S2-, HS-, Se2-, HSe-, Te2-, HTe -, TeS3 2-, OH-, and NH 2 - as Surface Ligands. *J. Am. Chem. Soc.* **2011**, *133* (27), 10612–10620.

(194) Kovalenko, M. V.; Scheele, M.; Talapin, D. V. Colloidal Nanocrystals with Molecular Metal Chalcogenide Surface Ligands. *Science (80-.).* **2009**, *324* (5933), 1417–1420.

(195) Choi, J. J.; Bian, K.; Baumgardner, W. J.; Smilgies, D.-M.; Hanrath, T. Interface-Induced Nucleation, Orientational Alignment and Symmetry Transformations in Nanocube Superlattices. *Nano Lett.* **2012**, *12* (9), 4791–4798.

(196) Boneschanscher, M. P.; Evers, W. H.; Geuchies, J. J.; Altantzis, T.; Goris, B.; Rabouw, F. T.; van Rossum, S. A. P.; van der Zant, H. S. J.; Siebbeles, L. D. A.; Van Tendeloo, G.; et al. Long-Range Orientation and Atomic Attachment of Nanocrystals in 2D Honeycomb Superlattices. *Science (80-.).* **2014**, *344* (6190), 1377–1380.

(197) Evers, W. H.; Schins, J. M.; Aerts, M.; Kulkarni, A.; Capiod, P.; Berthe, M.; Grandidier, B.; Delerue, C.; van der Zant, H. S. J.; van Overbeek, C.; et al. High Charge Mobility in Two-Dimensional Percolative Networks of PbSe Quantum Dots Connected by Atomic Bonds. *Nat. Commun.* **2015**, *6*, 8195.

(198) Beugeling, W.; Kalesaki, E.; Delerue, C.; Niquet, Y.-M.; Vanmaekelbergh, D.; Smith, C. M. Topological States in Multi-Orbital HgTe Honeycomb Lattices. *Nat. Commun.* **2015**, *6* (May 2014), 6316.

(199) Kalesaki, E.; Evers, W. H.; Allan, G.; Vanmaekelbergh, D.; Delerue, C. Electronic Structure of Atomically Coherent Square Semiconductor Superlattices with Dimensionality below Two. *Phys. Rev. B* **2013**, *88* (11), 115431.

(200) Kalesaki, E.; Delerue, C.; Morais Smith, C.; Beugeling, W.; Allan, G.; Vanmaekelbergh, D. Dirac Cones, Topological Edge States, and Nontrivial Flat Bands in Two-Dimensional Semiconductors with a Honeycomb Nanogeometry. *Phys. Rev. X* **2014**, *4* (1), 011010.

(201) Lee, J.-S.; Kovalenko, M. V.; Huang, J.; Chung, D. S.; Talapin, D. V. Band-like Transport, High Electron Mobility and High Photoconductivity in All-Inorganic Nanocrystal Arrays. *Nat. Nanotechnol.* **2011**, *6* (6), 348–352.

(202) Talgorn, E.; Gao, Y.; Aerts, M.; Kunneman, L. T.; Schins, J. M.; Savenije, T. J.; van Huis, M. a.; van der Zant, H. S. J.; Houtepen, A. J.; Siebbeles, L. D. a. Unity Quantum Yield of Photogenerated Charges and Band-like Transport in Quantum-Dot Solids. *Nat. Nanotechnol.* **2011**, *6* (11), 733–739.

(203) Guyot-Sionnest, P. Electrical Transport in Colloidal Quantum Dot Films. *J. Phys. Chem. Lett.* **2012**, *3* (9), 1169–1175.

(204) Boneschanscher, M. P.; Evers, W. H.; Geuchies, J. J.; Altantzis, T.; Goris, B.; Rabouw, F. T.; van Rossum, S. A. P.; van der Zant, H. S. J.; Siebbeles, L. D. A.; Van Tendeloo, G.; et al. Long-Range Orientation and Atomic Attachment of Nanocrystals in 2D Honeycomb Superlattices. *Science (80-.).* **2014**, *344* (6190), 1377–1380.

(205) Lhuillier, E.; Keuleyan, S.; Guyot-Sionnest, P. Optical Properties of HgTe Colloidal Quantum Dots. *Nanotechnology* **2012**, *23* (17), 175705.

(206) Cheng, L.; Liu, J.; Gu, X.; Gong, H.; Shi, X.; Liu, T.; Wang, C.; Wang, X.; Liu, G.; Xing, H.; et

al. PEGylated WS2 Nanosheets as a Multifunctional Theranostic Agent for in Vivo Dual-Modal CT/photoacoustic Imaging Guided Photothermal Therapy. *Adv. Mater.* **2014**, *26* (12), 1886–1893.

(207) Radisavljevic, B.; Radenovic, a; Brivio, J.; Giacometti, V.; Kis, a. Single-Layer MoS2 Transistors. *Nat. Nanotechnol.* **2011**, *6* (3), 147–150.

(208) Ye, Y.; Wong, Z. J.; Lu, X.; Ni, X.; Zhu, H.; Chen, X.; Wang, Y.; Zhang, X. Monolayer Excitonic Laser. *Nat. Photonics* **2015**, No. October, 1–5.

(209) Yin, Z.; Li, H.; Li, H.; Jiang, L.; Shi, Y.; Sun, Y.; Lu, G.; Zhang, Q.; Chen, X.; Zhang, H. Single-Layer MoS2 Phototransistors. *ACS Nano* **2012**, *6* (1), 74–80.

(210) Tan, C.; Liu, Z.; Huang, W.; Zhang, H. Non-Volatile Resistive Memory Devices Based on Solution-Processed Ultrathin Two-Dimensional Nanomaterials. *Chem. Soc. Rev.* **2015**, *44* (9), 2615–2628.

(211) Wang, Q. H.; Kalantar-Zadeh, K.; Kis, A.; Coleman, J. N.; Strano, M. S. Electronics and Optoelectronics of Two-Dimensional Transition Metal Dichalcogenides. *Nat. Nanotechnol.* **2012**, *7* (11), 699–712.

(212) Voiry, D.; Yamaguchi, H.; Li, J.; Silva, R.; Alves, D. C. B.; Fujita, T.; Chen, M.; Asefa, T.; Shenoy, V. B.; Eda, G.; et al. Enhanced Catalytic Activity in Strained Chemically Exfoliated WS_2 Nanosheets for Hydrogen Evolution. *Nat. Mater.* **2013**, *12* (9), 850–855.

(213) Lukowski, M. a.; Daniel, A. S.; Meng, F.; Forticaux, A.; Li, L.; Jin, S. Enhanced Hydrogen Evolution Catalysis from Chemically Exfoliated Metallic MoS2 Nanosheets. *J. Am. Chem. Soc.* **2013**, *135* (28), 10274–10277.

(214) Gu, X.; Cui, W.; Li, H.; Wu, Z.; Zeng, Z.; Lee, S.-T.; Zhang, H.; Sun, B. A Solution-Processed Hole Extraction Layer Made from Ultrathin MoS 2 Nanosheets for Efficient Organic Solar Cells. *Adv. Energy Mater.* **2013**, *3* (10), 1262–1268.

(215) Cunningham, G.; Lotya, M.; Cucinotta, C. S.; Sanvito, S.; Bergin, S. D.; Menzel, R.; Shaffer, M. S. P.; Coleman, J. N. Solvent Exfoliation of Transition Metal Dichalcogenides: Dispersibility of Exfoliated Nanosheets Varies Only Weakly between Compounds. *ACS Nano* **2012**, *6* (4), 3468–3480.

(216) Coleman, J. N.; Lotya, M.; O'Neill, A.; Bergin, S. D.; King, P. J.; Khan, U.; Young, K.; Gaucher, A.; De, S.; Smith, R. J.; et al. Two-Dimensional Nanosheets Produced by Liquid Exfoliation of Layered Materials. *Science* **2011**, *331* (6017), 568–571.

(217) Shen, J.; He, Y.; Wu, J.; Gao, C.; Keyshar, K.; Zhang, X.; Yang, Y.; Ye, M.; Vajtai, R.; Lou, J.; et al. Liquid Phase Exfoliation of Two-Dimensional Materials by Directly Probing and Matching Surface Tension Components. *Nano Lett.* **2015**, 150724081634000.

(218) Harvey, A.; Backes, C.; Gholamvand, Z.; Hanlon, D.; McAteer, D.; Nerl, H. C.; McGuire, E.; Seral-Ascaso, A.; Ramasse, Q. M.; McEvoy, N.; et al. Preparation of Gallium Sulfide Nanosheets by Liquid Exfoliation and Their Application As Hydrogen Evolution Catalysts. *Chem. Mater.* **2015**, *27* (9), 3483–3493.

(219) Hernandez, Y.; Nicolosi, V.; Lotya, M.; Blighe, F. M.; Sun, Z.; De, S.; McGovern, I. T.; Holland, B.; Byrne, M.; Gun'Ko, Y. K.; et al. High-Yield Production of Graphene by Liquid-Phase Exfoliation of Graphite. *Nat. Nanotechnol.* **2008**, *3* (9), 563–568.

(220) Paton, K. R.; Varrla, E.; Backes, C.; Smith, R. J.; Khan, U.; O'Neill, A.; Boland, C.; Lotya, M.; Istrate, O. M.; King, P.; et al. Scalable Production of Large Quantities of Defect-Free Few-Layer Graphene by Shear Exfoliation in Liquids. *Nat. Mater.* **2014**, *13* (6), 624–630.

(221) Varrla, E.; Backes, C.; Paton, K. R.; Harvey, A.; Gholamvand, Z.; McCauley, J.; Coleman, J. N. Large-Scale Production of Size-Controlled MoS 2 Nanosheets by Shear Exfoliation. *Chem. Mater.* **2015**, *27*, 1129–1139.

(222) Kim, J.; Kwon, S.; Cho, D.-H.; Kang, B.; Kwon, H.; Kim, Y.; Park, S. O.; Jung, G. Y.; Shin, E.; Kim, W.-G.; et al. Direct Exfoliation and Dispersion of Two-Dimensional Materials in Pure Water via Temperature Control. *Nat. Commun.* **2015**, *6*, 8294.

(223) Zhang, X.; Lai, Z.; Liu, Z.; Tan, C.; Huang, Y.; Li, B.; Zhao, M.; Xie, L.; Huang, W.; Zhang, H. A Facile and Universal Top-Down Method for Preparation of Monodisperse Transition-Metal Dichalcogenide Nanodots. *Angew. Chemie-International Ed.* **2015**, *54* (18), 5425–5428.

(224) Joensen, P.; Frindt, R. F.; Morrison, S. R. Single-Layer MoS2. *Mater. Res. Bull.* **1986**, *21* (4), 457–461.

(225) Zheng, J.; Zhang, H.; Dong, S.; Liu, Y.; Nai, C. T.; Shin, H. S.; Jeong, H. Y.; Liu, B.; Loh, K. P. High Yield Exfoliation of Two-Dimensional Chalcogenides Using Sodium Naphthalenide. *Nat. Commun.* **2014**, *5*, 2995.

(226) Zeng, Z.; Sun, T.; Zhu, J.; Huang, X.; Yin, Z.; Lu, G.; Fan, Z.; Yan, Q.; Hng, H. H.; Zhang, H. An Effective Method for the Fabrication of Few-Layer-Thick Inorganic Nanosheets. *Angew. Chem. Int. Ed. Engl.* **2012**, *51* (36), 9052–9056.

(227) Eda, G.; Yamaguchi, H.; Voiry, D.; Fujita, T.; Chen, M.; Chhowalla, M. Photoluminescence from Chemically Exfoliated MoS2. *Nano Lett.* **2011**, *11* (12), 5111–5116.

(228) Jeong, S.; Yoo, D.; Ahn, M.; Miró, P.; Heine, T.; Cheon, J. Tandem Intercalation Strategy for Single-Layer Nanosheets as an Effective Alternative to Conventional Exfoliation Processes. *Nat. Commun.* **2015**, *6*, 5763.

(229) Wilcoxon, J.; Samara, G. Strong Quantum-Size Effects in a Layered Semiconductor: MoS2 Nanoclusters. *Phys. Rev. B* **1995**, *51* (11), 7299–7302.

(230) Parsapour, F.; Kelley, D. F.; Craft, S.; Wilcoxon, J. P. Electron Transfer Dynamics in MoS2 Nanoclusters: Normal and Inverted Behavior. *J. Chem. Phys.* **1996**, *104* (13), 4978.

(231) Doolen, R.; Laitinen, R.; Parsapour, F.; Kelley, D. F. Trap State Dynamics in MoS 2 Nanoclusters. *J. Phys. Chem. B* **1998**, *102* (20), 3906–3911.

(232) Huang, J.; Laitinen, R.; Kelley, D. F. Spectroscopy and Trapping Dynamics in WS2 Nanoclusters. *Phys. Rev. B* **2000**, *62* (16), 10995–11005.

(233) Huang, J. M.; Kelley, D. F. Synthesis and Characterization of MoSe2 and WSe2 Nanoclusters. *Chem. Mater.* **2000**, *12* (10), 2825–2828.

(234) Chikan, V.; Kelley, D. F. Size-Dependent Spectroscopy of MoS2 Nanoclusters. *J. Phys. Chem. B* **2002**, 3794–3804.

(235) Mainwaring, D. E.; Let, A. L.; Rix, C.; Murugaraj, P. Titanium Sulphide Nanoclusters Formed within Inverse Micelles. *Solid State Commun.* **2006**, *140* (7-8), 355–358.

(236) Peng, Y.; Meng, Z.; Zhong, C.; Lu, J.; Yu, W.; Jia, Y.; Qian, Y. Hydrothermal Synthesis and Characterization of Single-Molecular-Layer MoS 2 and MoSe 2. **2001**.

(237) Duphil, D.; Bastide, S.; Rouchaud, J. C.; Pastol, J. L.; Legendre, B.; Lévy-Clément, C. The Chemical Synthesis in Solution and Characterization of Transition Metal Dichalcogenide MX 2 (M = Mo, W; X = S, Se) Nanoparticles. *Nanotechnology* **2004**, *15* (7), 828–832.

(238) Chen, X.; Fan, R. Low-Temperature Hydrothermal Synthesis of Transition Metal Dichalcogenides. *Chem. Mater.* **2001**, *13* (3), 802–805.

(239) Tang, G.; Sun, J.; Wei, C.; Wu, K.; Ji, X.; Liu, S.; Tang, H.; Li, C. Synthesis and Characterization of Flowerlike MoS2 Nanostructures through CTAB-Assisted Hydrothermal Process. *Mater. Lett.* **2012**, *86*, 9–12.

(240) Park, K. H.; Choi, J.; Kim, H. J.; Oh, D.-H.; Ahn, J. R.; Son, S. U. Unstable Single-Layered Colloidal TiS2 Nanodisks. *Small* **2008**, *4* (7), 945–950.

(241) Plashnitsa, V. V.; Vietmeyer, F.; Petchsang, N.; Tongying, P.; Kosel, T. H.; Kuno, M. Synthetic Strategy and Structural and Optical Characterization of Thin Highly Crystalline Titanium Disulfide Nanosheets. *J. Phys. Chem. Lett.* **2012**, *3* (11), 1554–1558.

(242) Jeong, S.; Han, J. H.; Jang, J.; Seo, J.; Kim, J.-G.; Cheon, J. Transformative Two-Dimensional Layered Nanocrystals. *J. Am. Chem. Soc.* **2011**, *133* (37), 14500–14503.

(243) Prabakar, S.; Bumby, C. W.; Tilley, R. D. Liquid-Phase Synthesis of Flower-like and Flake-like Titanium Disulfide Nanostructures. *Chem. Mater.* **2009**, *21* (8), 1725–1730.

(244) Yoo, D.; Kim, M.; Jeong, S.; Han, J.; Cheon, J. Chemical Synthetic Strategy for Single-Layer Transition-Metal Chalcogenides. *J. Am. Chem. Soc.* **2014**, *136* (42), 14670–14673.

(245) Jeong, S.; Yoo, D.; Jang, J.-T.; Kim, M.; Cheon, J. Well-Defined Colloidal 2-D Layered Transition-Metal Chalcogenide Nanocrystals via Generalized Synthetic Protocols. *J. Am. Chem. Soc.* **2012**, *134* (44), 18233–18236.

(246) Jang, J.; Jeong, S.; Seo, J.; Kim, M.-C.; Sim, E.; Oh, Y.; Nam, S.; Park, B.; Cheon, J. Ultrathin Zirconium Disulfide Nanodiscs. *J. Am. Chem. Soc.* **2011**, *133* (20), 7636–7639.

(247) Seo, J.-W.; Jun, Y.-W.; Park, S.-W.; Nah, H.; Moon, T.; Park, B.; Kim, J.-G.; Kim, Y. J.; Cheon, J. Two-Dimensional Nanosheet Crystals. *Angew. Chem. Int. Ed. Engl.* **2007**, *46* (46), 8828–8831.

(248) Altavilla, C.; Sarno, M.; Ciambelli, P. A Novel Wet Chemistry Approach for the Synthesis of Hybrid 2D Free-Floating Single or Multilayer Nanosheets of MS2 @oleylamine (M═Mo, W). *Chem. Mater.* **2011**, *23* (17), 3879–3885.

(249) Antunez, P. D. P.; Webber, D. D. H.; Brutchey, R. R. L. Solution-Phase Synthesis of Highly Conductive Tungsten Diselenide Nanosheets. *Chem. Mater.* **2013**, *25* (12), 2385–2387.

(250) Mahler, B.; Hoepfner, V.; Liao, K.; Ozin, G. a. Colloidal Synthesis of 1T-WS2 and 2H-WS2 Nanosheets: Applications for Photocatalytic Hydrogen Evolution. *J. Am. Chem. Soc.* **2014**, *136* (40), 14121–14127.

(251) Jung, W.; Lee, S.; Yoo, D.; Jeong, S.; Miró, P.; Kuc, A.; Heine, T.; Cheon, J. Colloidal Synthesis of Single-Layer MSe 2 (M = Mo, W) Nanosheets via Anisotropic Solution-Phase Growth Approach. *J. Am. Chem. Soc.* **2015**, *137* (23), 7266–7269.

(252) Zhou, X.; Jiang, J.; Ding, T.; Zhang, J.; Pan, B.; Zuo, J.; Yang, Q. Fast Colloidal Synthesis of Scalable Mo-Rich Hierarchical Ultrathin MoSe 2−x Nanosheets for High-Performance Hydrogen Evolution. *Nanoscale* **2014**, *6* (c), 11046–11051.

(253) Wilson, J.; Yoffe, A. The Transition Metal Dichalcogenides Discussion and Interpretation of the Observed Optical, Electrical and Structural Properties. *Adv. Phys.* **1969**, *18* (73), 193–335.

(254) Chen, Y.; Xi, J.; Dumcenco, D. O.; Liu, Z.; Suenaga, K.; Wang, D.; Shuai, Z.; Huang, Y.-S.; Xie, L. Tunable Band Gap Photoluminescence from Atomically Thin Transition-Metal Dichalcogenide Alloys. *ACS Nano* **2013**, No. Xx.

(255) Zhang, K.; Feng, S.; Wang, J.; Azcatl, A.; Lu, N.; Addou, R.; Wang, N.; Zhou, C.; Lerach, J.; Bojan, V.; et al. Manganese Doping of Monolayer MoS_2 : The Substrate Is Critical. *Nano Lett.* **2015**, 150916105118005.

(256) Duan, X.; Wang, C.; Shaw, J. C.; Cheng, R.; Chen, Y.; Li, H.; Wu, X.; Tang, Y.; Zhang, Q.; Pan, A.; et al. Lateral Epitaxial Growth of Two-Dimensional Layered Semiconductor Heterojunctions. *Nat. Nanotechnol.* **2014**, No. September, 1–7.

(257) Han, J. H.; Lee, S.; Yoo, D.; Lee, J.-H.; Jeong, S.; Kim, J.-G.; Cheon, J. Unveiling Chemical Reactivity and Structural Transformation of Two-Dimensional Layered Nanocrystals. *J. Am. Chem. Soc.* **2013**, *135* (10), 3736–3739.

(258) Govinda Rao, B.; Matte, H. S. S. R.; Rao, C. N. R. Decoration of Few-Layer Graphene-Like MoS2 and MoSe2 by Noble Metal Nanoparticles. *J. Clust. Sci.* **2012**, *23* (3), 929–937.

(259) Sreeprasad, T. S.; Nguyen, P.; Kim, N.; Berry, V. Controlled, Defect-Guided, Metal-Nanoparticle Incorporation onto MoS2 via Chemical and Microwave Routes: Electrical, Thermal, and Structural Properties. *Nano Lett.* **2013**, *13* (9), 4434–4441.

(260) Huang, X.; Zeng, Z.; Bao, S.; Wang, M.; Qi, X.; Fan, Z.; Zhang, H. Solution-Phase Epitaxial Growth of Noble Metal Nanostructures on Dispersible Single-Layer Molybdenum Disulfide Nanosheets. *Nat. Commun.* **2013**, *4*, 1444.

(261) Kim, J.; Byun, S.; Smith, A. J.; Yu, J.; Huang, J. Enhanced Electrocatalytic Properties of Transition-Metal Dichalcogenides Sheets by Spontaneous Gold Nanoparticle Decoration. *J. Phys. Chem. Lett.* **2013**, *4*, 1227–1232.

(262) Shi, Y.; Huang, J.-K.; Jin, L.; Hsu, Y.-T.; Yu, S. F.; Li, L.-J.; Yang, H. Y. Selective Decoration of Au Nanoparticles on Monolayer MoS2 Single Crystals. *Sci. Rep.* **2013**, *3*, 1839.

(263) Polyakov, A. Y.; Yadgarov, L.; Popovitz-Biro, R.; Lebedev, V. A.; Pinkas, I.; Rosentsveig, R.; Feldman, Y.; Goldt, A. E.; Goodilin, E. A.; Tenne, R. Decoration of WS 2 Nanotubes and Fullerene-Like MoS 2 with Gold Nanoparticles. *J. Phys. Chem. C* **2014**, 140117130029003.

(264) Kiriya, D.; Zhou, Y.; Nelson, C.; Hettick, M.; Madhvapathy, S. R.; Chen, K.; Zhao, P.; Tosun, M.; Minor, A. M.; Chrzan, D. C.; et al. Oriented Growth of Gold Nanowires on MoS 2. *Adv. Funct. Mater.* **2015**, *25* (39), 6257–6264.

(265) Hong, X.; Liu, J.; Zheng, B.; Huang, X.; Zhang, X.; Tan, C.; Chen, J.; Fan, Z.; Zhang, H. A Universal Method for Preparation of Noble Metal Nanoparticle-Decorated Transition Metal Dichalcogenide Nanobelts. *Adv. Mater.* **2014**, No. 103, 1–5.

(266) Lampeka, Y. D.; Tsymbal, L. V. Nanocomposites of Two-Dimensional Molybdenum and Tungsten Dichalcogenides with Metal Particles: Preparation and Prospects for Application. *Theor. Exp. Chem.* **2015**, *51* (3), 141–162.

(267) Tan, C.; Zhang, H. Two-Dimensional Transition Metal Dichalcogenide Nanosheet-Based Composites. *Chem. Soc. Rev.* **2015**, *44* (9), 2713–2731.

(268) Huang, X.; Tan, C.; Yin, Z.; Zhang, H. 25th Anniversary Article: Hybrid Nanostructures Based on Two-Dimensional Nanomaterials. *Adv. Mater.* **2014**, *26* (14), 2185–2204.

(269) Chen, J.; Wu, X.-J.; Yin, L.; Li, B.; Hong, X.; Fan, Z.; Chen, B.; Xue, C.; Zhang, H. One-Pot Synthesis of CdS Nanocrystals Hybridized with Single-Layer Transition-Metal Dichalcogenide Nanosheets for Efficient Photocatalytic Hydrogen Evolution. *Angew. Chemie Int. Ed.* **2015**, *54* (4), 1210–1214.

(270) Rossi, D.; Han, J. H.; Yoo, D.; Dong, Y.; Park, Y.; Cheon, J.; Son, D. H. Photoinduced Separation of Strongly Interacting 2-D Layered TiS 2 Nanodiscs in Solution. *J. Phys. Chem. C* **2014**, 140530091518000.

(271) Rossi, D.; Han, J. H.; Jung, W.; Cheon, J.; Son, D. H. Orientational Control of Colloidal 2D-Layered Transition Metal Dichalcogenide Nanodiscs via Unusual Electrokinetic Response. *ACS Nano* **2015**, *9* (8), 8037–8043.

(272) Tan, C.; Qi, X.; Liu, Z.; Zhao, F.; Li, H.; Huang, X.; Shi, L.; Zheng, B.; Zhang, X.; Xie, L.; et al. Self-Assembled Chiral Nanofibers from Ultrathin Low-Dimensional Nanomaterials. *J. Am. Chem. Soc.* **2015**, *137* (4), 1565–1571.

(273) Joo, P.; Jo, K.; Ahn, G.; Voiry, D.; Jeong, H. Y.; Ryu, S.; Chhowalla, M.; Kim, B.-S. Functional Polyelectrolyte Nanospaced MoS2 Multilayers for Enhanced Photoluminescence. *Nano Lett.* **2014**.

(274) Withers, F.; Yang, H.; Britnell, L.; Rooney, A.; Lewis, E.; Felten, A.; Woods, C.; Sanchez Romaguera, V.; Georgiou, T.; Eckmann, A.; et al. Heterostructures Produced from Nanosheet-Based Inks. *Nano Lett.* **2014**.

(275) Green, M. The Nature of Quantum Dot Capping Ligands. *J. Mater. Chem.* **2010**, *20* (28), 5797.

(276) Presolski, S.; Pumera, M. Covalent Functionalization of MoS2. *Mater. Today* **2015**, *00* (00), 4–9.

(277) Chou, S. S.; De, M.; Kim, J.; Byun, S.; Dykstra, C.; Yu, J.; Huang, J.; Dravid, V. P. Ligand Conjugation of Chemically Exfoliated MoS2. *J. Am. Chem. Soc.* **2013**, *135* (12), 4584–4587.

(278) Liu, T.; Wang, C.; Gu, X.; Gong, H.; Cheng, L.; Shi, X.; Feng, L.; Sun, B.; Liu, Z. Drug Delivery with PEGylated MoS2 Nano-Sheets for Combined Photothermal and Chemotherapy of Cancer. *Adv. Mater.* **2014**, *26* (21), 3433–3440.

(279) Voiry, D.; Goswami, A.; Kappera, R.; Silva, C. D. C. C. E.; Kaplan, D.; Fujita, T.; Chen, M.; Asefa, T.; Chhowalla, M.; Carvalho Castro e Silva, C. De; et al. Covalent Functionalization of Monolayered Transition Metal Dichalcogenides by Phase Engineering. *Nat. Chem.* **2014**, No. November, 6–10.

(280) Tang, Q.; Jiang, D. Stabilization and Band-Gap Tuning of the 1T-MoS 2 Monolayer by

Covalent Functionalization. *Chem. Mater.* **2015**, 150514080102009.

(281) Backes, C.; Berner, N. C.; Chen, X.; Lafargue, P.; LaPlace, P.; Freeley, M.; Duesberg, G. S.; Coleman, J. N.; McDonald, A. R. Functionalization of Liquid-Exfoliated Two-Dimensional 2H-MoS2. *Angew. Chemie Int. Ed.* **2015**, *54* (9), 2638–2642.

(282) Tahir, M. N.; Zink, N.; Eberhardt, M.; Therese, H. a.; Kolb, U.; Theato, P.; Tremel, W. Overcoming the Insolubility of Molybdenum Disulfide Nanoparticles through a High Degree of Sidewall Functionalization Using Polymeric Chelating Ligands. *Angew. Chemie - Int. Ed.* **2006**, *45* (29), 4809–4815.

(283) Chou, S. S.; Kaehr, B.; Kim, J.; Foley, B. M.; De, M.; Hopkins, P. E.; Huang, J.; Brinker, C. J.; Dravid, V. P. Chemically Exfoliated MoS2 as near-Infrared Photothermal Agents. *Angew. Chemie - Int. Ed.* **2013**, *52*, 4160–4164.

(284) Feng, W.; Chen, L.; Qin, M.; Zhou, X.; Zhang, Q.; Miao, Y.; Qiu, K.; Zhang, Y.; He, C. Flower-like PEGylated MoS2 Nanoflakes for near-Infrared Photothermal Cancer Therapy. *Sci. Rep.* **2015**, *5*, 17422.

(285) Yin, W.; Yan, L.; Yu, J.; Tian, G.; Zhou, L.; Zheng, X.; Zhang, X.; Yong, Y.; Li, J.; Gu, Z.; et al. High-Throughput Synthesis of Single-Layer MoS2 Nanosheets as a Near-Infrared Photothermal-Triggered Drug Delivery for Effective Cancer Therapy. *ACS Nano* **2014**.

(286) Yong, Y.; Zhou, L.; Gu, Z.; Yan, L.; Tian, G.; Zheng, X.; Liu, X.; Zhang, X.; Shi, J.; Cong, W.; et al. WS2 Nanosheet as a New Photosensitizer Carrier for Combined Photodynamic and Photothermal Therapy of Cancer Cells. *Nanoscale* **2014**, *00* (17), 10394–10403.

(287) Cheng, L.; Yuan, C.; Shen, S.; Yi, X.; Gong, H.; Yang, K.; Liu, Z. Bottom-Up Synthesis of Metal-Ion-Doped WS 2 Nanoflakes for Cancer Theranostics. *ACS Nano* **2015**, No. Xx, 151009141427009.

(288) Zhu, C.; Zeng, Z.; Li, H.; Li, F.; Fan, C.; Zhang, H. Single-Layer MoS2-Based Nanoprobes for Homogeneous Detection of Biomolecules. *J. Am. Chem. Soc.* **2013**, *135* (16), 5998–6001.

(289) Tan, C.; Yu, P.; Hu, Y.; Chen, J.; Huang, Y.; Cai, Y.; Luo, Z.; Li, B.; Lu, Q.; Wang, L.; et al. High-Yield Exfoliation of Ultrathin Two-Dimensional Ternary Chalcogenide Nanosheets for Highly Sensitive and Selective Fluorescence DNA Sensors. *J. Am. Chem. Soc.* **2015**, *137* (32), 10430–10436.

(290) Zhang, Y.; Zheng, B.; Zhu, C.; Zhang, X.; Tan, C.; Li, H.; Chen, B.; Yang, J.; Chen, J.; Huang, Y.; et al. Single-Layer Transition Metal Dichalcogenide Nanosheet-Based Nanosensors for Rapid, Sensitive, and Multiplexed Detection of DNA. *Adv. Mater.* **2015**, *27* (5), 935–939.

(291) Kalantar-zadeh, K.; Ou, J. Z.; Daeneke, T.; Strano, M. S.; Pumera, M.; Gras, S. L. Two-Dimensional Transition Metal Dichalcogenides in Biosystems. *Adv. Funct. Mater.* **2015**, *25* (32), 5086–5099.

(292) Jaramillo, T. F.; Jørgensen, K. P.; Bonde, J.; Nielsen, J. H.; Horch, S.; Chorkendorff, I. Identification of Active Edge Sites for Electrochemical H2 Evolution from MoS2 Nanocatalysts. *Science* **2007**, *317* (5834), 100–102.

(293) Xie, J.; Zhang, J.; Li, S.; Grote, F.; Zhang, X.; Zhang, H.; Wang, R.; Lei, Y.; Pan, B.; Xie, Y.

Controllable Disorder Engineering in Oxygen-Incorporated MoS2 Ultrathin Nanosheets for Efficient Hydrogen Evolution. *J. Am. Chem. Soc.* **2013**, 1–9.

(294) Lu, Q.; Yu, Y.; Ma, Q.; Chen, B.; Zhang, H. 2D Transition-Metal-Dichalcogenide-Nanosheet-Based Composites for Photocatalytic and Electrocatalytic Hydrogen Evolution Reactions. *Advanced Materials*. December 2015, p n/a – n/a.

(295) Peng, B.; Ang, P. K.; Loh, K. P. Two-Dimensional Dichalcogenides for Light-Harvesting Applications. *Nano Today* **2015**, 1–10.

(296) Muller, G. A.; Cook, J.; Kim, H. S.; Tolbert, S. H.; Dunn, B. High Performance Pseudocapacitor Based on 2D Layered Metal Chalcogenide Nanocrystals. *Nano Lett.* **2015**, 150205114116003.

(297) Acerce, M.; Voiry, D.; Chhowalla, M. Metallic 1T Phase MoS2 Nanosheets as Supercapacitor Electrode Materials. *Nat. Nanotechnol.* **2015**, *10* (4), 313–318.

(298) Peng, X.; Peng, L.; Wu, C.; Xie, Y. Two Dimensional Nanomaterials for Flexible Supercapacitors. *Chem. Soc. Rev.* **2014**, *43* (10), 3303.

(299) Bonaccorso, F.; Colombo, L.; Yu, G.; Stoller, M.; Tozzini, V.; Ferrari, a C.; Ruoff, R. S.; Pellegrini, V. 2D Materials. Graphene, Related Two-Dimensional Crystals, and Hybrid Systems for Energy Conversion and Storage. *Science (80-.).* **2015**, *347* (6217), 1246501.

(300) Sun, Y.; Cheng, H.; Gao, S.; Sun, Z.; Liu, Q.; Liu, Q.; Lei, F.; Yao, T.; He, J.; Wei, S.; et al. Freestanding Tin Disulfide Single-Layers Realizing Efficient Visible-Light Water Splitting. *Angew. Chemie Int. Ed.* **2012**, *51* (35), 8727–8731.

(301) Seo, J. W.; Jang, J. T.; Park, S. W.; Kim, C.; Park, B.; Cheon, J. Two-Dimensional SnS2 Nanoplates with Extraordinary High Discharge Capacity for Lithium Ion Batteries. *Adv. Mater.* **2008**, *20* (22), 4269–4273.

(302) Zhai, C.; Du, N.; Yang, H. Z. D. Large-Scale Synthesis of Ultrathin Hexagonal Tin Disulfide Nanosheets with Highly Reversible Lithium Storage. *Chem. Commun. (Camb).* **2011**, *47* (4), 1270–1272.

(303) Yu, J.; Xu, C.; Ma, F.; Hu, S.; Zhang, Y.; Zhen, L. Monodisperse SnS 2 Nanosheets for High-Performance Photocatalytic Hydrogen Generation. *ACS Appl. Mater. Interfaces* **2014**, *6* (24), 22370–22377.

(304) Fang, Z.; Hao, S.; Long, L.; Fang, H.; Qiang, T.; Song, Y. The Enhanced Photoelectrochemical Response of SnSe2 Nanosheets. *CrystEngComm* **2014**, *16* (12), 2404.

(305) Zhang, C.; Yin, H.; Han, M.; Dai, Z.; Pang, H.; Zheng, Y.; Lan, Y.-Q.; Bao, J.; Zhu, J. Two-Dimensional Tin Selenide Nanostructures for Flexible All-Solid-State Supercapacitors. *ACS Nano* **2014**, *8* (4), 3761–3770.

(306) Vaughn, D. D.; In, S.-I.; Schaak, R. E. A Precursor-Limited Nanoparticle Coalescence Pathway for Tuning the Thickness of Laterally-Uniform Colloidal Nanosheets: The Case of SnSe. *ACS Nano* **2011**, *5* (11), 8852–8860.

(307) Li, L.; Chen, Z.; Hu, Y.; Wang, X.; Zhang, T.; Chen, W.; Wang, Q. Single-Layer Single-Crystalline SnSe Nanosheets. *J. Am. Chem. Soc.* **2013**, *135* (4), 1213–1216.

(308) Vaughn II, D. D.; Patel, R. J.; Hickner, M. a.; Schaak, R. E. Single-Crystal Colloidal Nanosheets of GeS and GeSe. *J. Am. Chem. Soc.* **2010**, *132* (43), 15170–15172.

(309) Zhang, Y.; Lu, J.; Shen, S.; Xu, H.; Wang, Q. Ultralarge Single Crystal SnS Rectangular Nanosheets. *Chem. Commun.* **2011**, *47* (18), 5226.

(310) de Kergommeaux, A.; Lopez-Haro, M.; Pouget, S.; Zuo, J.-M.; Lebrun, C.; Chandezon, F.; Aldakov, D.; Reiss, P. Synthesis, Internal Structure, and Formation Mechanism of Monodisperse Tin Sulfide Nanoplatelets. *J. Am. Chem. Soc.* **2015**, *137* (31), 9943–9952.

(311) Brent, J. R.; Lewis, D. J.; Lorenz, T.; Lewis, E. A.; Savjani, N.; Haigh, S. J.; Seifert, G.; Derby, B.; O'Brien, P. Tin(II) Sulfide (SnS) Nanosheets by Liquid-Phase Exfoliation of Herzenbergite: IV–VI Main Group Two-Dimensional Atomic Crystals. *J. Am. Chem. Soc.* **2015**, *137* (39), 12689–12696.

(312) Poudel, B.; Hao, Q.; Ma, Y.; Lan, Y.; Minnich, A.; Yu, B.; Yan, X.; Wang, D.; Muto, A.; Vashaee, D.; et al. High-Thermoelectric Performance of Nanostructured Bismuth Antimony Telluride Bulk Alloys. *Science* **2008**, *320* (5876), 634–638.

(313) Talapin, D. V.; Lee, J.-S.; Kovalenko, M. V.; Shevchenko, E. V. Prospects of Colloidal Nanocrystals for Electronic and Optoelectronic Applications. *Chem. Rev.* **2010**, *110* (1), 389–458.

(314) Ando, Y. Topological Insulator Materials. *J. Phys. Soc. Japan* **2013**, *82* (10), 102001.

(315) Fei, F.; Wei, Z.; Wang, Q.; Lu, P.; Wang, S.; Qin, Y.; Pan, D.; Zhao, B.; Wang, X.; Sun, J.; et al. Solvothermal Synthesis of Lateral Heterojunction Sb_2Te_3/Bi_2Te_3 Nanoplates. *Nano Lett.* **2015**, *15* (9), 5905–5911.

(316) Scheele, M.; Oeschler, N.; Meier, K.; Kornowski, A.; Klinke, C.; Weller, H. Synthesis and Thermoelectric Characterization of Bi_2Te_3 Nanoparticles. *Adv. Funct. Mater.* **2009**, *19* (21), 3476–3483.

(317) Wang, W.; Poudel, B.; Yang, J.; Wang, D. Z.; Ren, Z. F. High-Yield Synthesis of Single-Crystalline Antimony Telluride Hexagonal Nanoplates Using a Solvothermal Approach. *J. Am. Chem. Soc.* **2005**, *127* (40), 13792–13793.

(318) Shi, W.; Zhou, L.; Song, S.; Yang, J.; Zhang, H. Hydrothermal Synthesis and Thermoelectric Transport Properties of Impurity-Free Antimony Telluride Hexagonal Nanoplates. *Adv. Mater.* **2008**, *20* (10), 1892–1897.

(319) Shi, W.; Yu, J.; Wang, H.; Zhang, H. Hydrothermal Synthesis of Single-Crystalline Antimony Telluride Nanobelts. *J. Am. Chem. Soc.* **2006**, *128* (51), 16490–16491.

(320) Zhou, N.; Chen, G.; Zhang, X.-S.; Xu, Y.-C.; Xu, B.-R.; Li, M.-Q. Size-Controlled Synthesis and Transport Properties of Sb_2Te_3 Nanoplates. *RSC Adv.* **2014**, *4* (5), 2427–2432.

(321) Zhou, B.; Ji, Y.; Yang, Y.-F.; Li, X.-H.; Zhu, J.-J. Rapid Microwave-Assisted Synthesis of Single-Crystalline Sb 2 Te 3 Hexagonal Nanoplates. *Cryst. Growth Des.* **2008**, *8* (12), 4394–4397.

(322) Yang, H. Q.; Miao, L.; Liu, C. Y.; Li, C.; Honda, S.; Iwamoto, Y.; Huang, R.; Tanemura, S. A Facile Surfactant-Assisted Reflux Method for the Synthesis of Single-Crystalline Sb_2Te_3 Nanostructures with Enhanced Thermoelectric Performance. *ACS Appl. Mater. Interfaces* **2015**, *7* (26), 14263–14271.

(323) Lhuillier, E.; Keuleyan, S.; Robin, A.; Izquierdo, E.; Xu, X. Z.; Lequeux, N.; Descamps Mandine, A.; Patriarche, G.; Lacaze, E.; Aubin, H.; et al. Submitted. *Submitted*.

(324) Miller, G. R.; Li, C.-Y. Evidence for the Existence of Antistructure Defects in Bismuth Telluride by Density Measurements. *J. Phys. Chem. Solids* **1965**, *26* (1), 173–177.

(325) Horák, J.; Čermák, K.; Koudelka, L. Energy Formation of Antisite Defects in Doped Sb2Te3 and Bi2Te3 Crystals. *J. Phys. Chem. Solids* **1986**, *47* (8), 805–809.

(326) Drasar, C.; Lostak, P.; Uher, C. Doping and Defect Structure of Tetradymite-Type Crystals. *J. Electron. Mater.* **2010**, *39* (9), 2162–2164.

(327) Horak, J.; Drasar, C.; Novotny, R.; Karamazov, S.; Lostak, P. Non-Stoichiometry of the Crystal Lattice of Antimony Telluride. *Phys. Status Solidi* **1995**, *149*, 549–556.

(328) Lee, S.-W.; Chang, S.-H.; Lai, Y.-S.; Lin, C.-C.; Tsai, C.-M.; Lee, Y.-C.; Chen, J.-C.; Huang, C.-L. Effect of Temperature on the Growth of Silver Nanoparticles Using Plasmon-Mediated Method under the Irradiation of Green LEDs. *Materials (Basel).* **2014**, *7* (12), 7781–7798.

(329) Maillard, M.; Huang, P.; Brus, L. Silver Nanodisk Growth by Surface Plasmon Enhanced Photoreduction of Adsorbed [Ag +]. *Nano Lett.* **2003**, *3* (11), 1611–1615.

(330) Bastys, V.; Pastoriza-Santos, I.; Rodríguez-González, B.; Vaisnoras, R.; Liz-Marzán, L. M. Formation of Silver Nanoprisms with Surface Plasmons at Communication Wavelengths. *Adv. Funct. Mater.* **2006**, *16* (6), 766–773.

(331) Rocha, T. C. R.; Zanchet, D. Growth Aspects of Photochemically Synthesized Silver Triangular Nanoplates. *J. Nanosci. Nanotechnol.* **2007**, *7* (2), 618–625.

(332) Pastoriza-Santos, I.; Alvarez-Puebla, R. a.; Liz-Marzán, L. M. Synthetic Routes and Plasmonic Properties of Noble Metal Nanoplates. *Eur. J. Inorg. Chem.* **2010**, *2010* (27), 4288–4297.

(333) Rocha, T. C. R.; Winnischofer, H.; Westphal, E.; Zanchet, D. Formation Kinetics of Silver Triangular Nanoplates. *J. Phys. Chem. C* **2007**, *111* (7), 2885–2891.

(334) Rocha, T. C. R.; Zanchet, D. Structural Defects and Their Role in the Growth of Ag Triangular Nanoplates. *J. Phys. Chem. C* **2007**, *111* (19), 6989–6993.

(335) Machulek Junior, A.; Paulo Moiss de Oliveira, H.; Henrique Gehlen, M. Preparation of Silver Nanoprisms Using poly(N-Vinyl-2-Pyrrolidone) as a Colloid-Stabilizing Agent and the Effect of Silver Nanoparticles on the Photophysical Properties of Cationic Dyes. *Photochem. Photobiol. Sci.* **2003**, *2* (9), 921.

(336) Jin, R. Photoinduced Conversion of Silver Nanospheres to Nanoprisms. *Science (80-.).* **2001**, *294* (5548), 1901–1903.

(337) Jin, R.; Cao, Y. C.; Hao, E.; Me, G. S.; Schatz, G. C.; Mirkin, C. A.; Charles Cao, Y.; Hao, E.; Métraux, G. S.; Schatz, G. C.; et al. Controlling Anisotropic Nanoparticle Growth through Plasmon Excitation. *Nature* **2003**, *425* (6957), 487–490.

(338) Sun, Y.; Xia, Y. Triangular Nanoplates of Silver: Synthesis, Characterization, and Use as Sacrificial Templates For Generating Triangular Nanorings of Gold. *Adv. Mater.* **2003**, *15* (9), 695–699.

(339) Xue, C.; Mirkin, C. pH-Switchable Silver Nanoprism Growth Pathways. *Angew. Chemie Int. Ed.* **2007**, *46* (12), 2036–2038.

(340) Beberwyck, B. J.; Surendranath, Y.; Alivisatos, A. P. Cation Exchange: A Versatile Tool for Nanomaterials Synthesis. *J. Phys. Chem. C* **2013**, *117* (39), 19759–19770.

(341) Son, D. H. Cation Exchange Reactions in Ionic Nanocrystals. *Science (80-.).* **2004**, *306* (5698), 1009–1012.

(342) Wang, Y.; Zhukovskyi, M.; Tongying, P.; Tian, Y.; Kuno, M. Synthesis of Ultrathin and Thickness-Controlled Cu 2– X Se Nanosheets via Cation Exchange. *J. Phys. Chem. Lett.* **2014**, *5* (21), 3608–3613.

(343) Bouet, C.; Laufer, D.; Mahler, B.; Nadal, B.; Heuclin, H.; Pedetti, S.; Patriarche, G.; Dubertret, B. Synthesis of Zinc and Lead Chalcogenide Core and Core/Shell Nanoplatelets Using Sequential Cation Exchange Reactions. *Chem. Mater.* **2014**, *26* (9), 3002–3008.

(344) Kojima, A.; Teshima, K.; Shirai, Y.; Miyasaka, T. Organometal Halide Perovskites as Visible-Light Sensitizers for Photovoltaic Cells. *J. Am. Chem. Soc.* **2009**, *131* (17), 6050–6051.

(345) Meng, L.; You, J.; Guo, T.-F.; Yang, Y. Recent Advances in the Inverted Planar Structure of Perovskite Solar Cells. *Acc. Chem. Res.* **2016**, *49* (1), 155–165.

(346) Ziang, X.; Shifeng, L.; Laixiang, Q.; Shuping, P.; Wei, W.; Yu, Y.; Li, Y.; Zhijian, C.; Shufeng, W.; Honglin, D.; et al. Refractive Index and Extinction Coefficient of CH_3NH_3PbI_3 Studied by Spectroscopic Ellipsometry. *Opt. Mater. Express* **2014**, *5* (1), 29.

(347) Vybornyi, O.; Yakunin, S.; Kovalenko, M. V. Polar-Solvent-Free Colloidal Synthesis of Highly Luminescent Alkylammonium Lead Halide Perovskite Nanocrystals. *Nanoscale* **2016**, 2–7.

(348) Protesescu, L.; Yakunin, S.; Bodnarchuk, M. I.; Krieg, F.; Caputo, R.; Hendon, C. H.; Yang, R. X.; Walsh, A.; Kovalenko, M. V. Nanocrystals of Cesium Lead Halide Perovskites (CsPbX 3 , X = Cl, Br, and I): Novel Optoelectronic Materials Showing Bright Emission with Wide Color Gamut. *Nano Lett.* **2015**, *15* (6), 3692–3696.

(349) Dong, Q.; Fang, Y.; Shao, Y.; Mulligan, P.; Qiu, J.; Cao, L.; Huang, J. Solar Cells. Electron-Hole Diffusion Lengths > 175 Mm in Solution-Grown CH3NH3PbI3 Single Crystals. *Science* **2015**, *347* (6225), 967–970.

(350) Stranks, S. D.; Snaith, H. J. Metal-Halide Perovskites for Photovoltaic and Light-Emitting Devices. *Nat. Nanotechnol.* **2015**, *10* (5), 391–402.

(351) Dou, L.; Yang, Y. M.; You, J.; Hong, Z.; Chang, W.-H.; Li, G.; Yang, Y. Solution-Processed Hybrid Perovskite Photodetectors with High Detectivity. *Nat. Commun.* **2014**, *5*, 5404.

(352) Tan, Z.-K.; Moghaddam, R. S.; Lai, M. L.; Docampo, P.; Higler, R.; Deschler, F.; Price, M.; Sadhanala, A.; Pazos, L. M.; Credgington, D.; et al. Bright Light-Emitting Diodes Based on Organometal Halide Perovskite. *Nat. Nanotechnol.* **2014**, *9* (9), 687–692.

(353) Li, G.; Tan, Z.-K.; Di, D.; Lai, M. L.; Jiang, L.; Lim, J. H.; Friend, R. H.; Greenham, N. C. Efficient Light-Emitting Diodes Based on Nano-Crystalline Perovskite in a Dielectric Polymer Matrix. *Nano Lett.* **2015**, 150224102034001.

(354) Stoumpos, C. C.; Malliakas, C. D.; Kanatzidis, M. G. Semiconducting Tin and Lead Iodide Perovskites with Organic Cations: Phase Transitions, High Mobilities, and Near-Infrared Photoluminescent Properties. *Inorg. Chem.* **2013**, *52* (15), 9019–9038.

(355) Stoumpos, C. C.; Kanatzidis, M. G. The Renaissance of Halide Perovskites and Their Evolution as Emerging Semiconductors. *Acc. Chem. Res.* **2015**, *48* (10), 2791–2802.

(356) Papavassiliou, G. C. Synthetic Three-and Lower-Dimensional Semiconductors Based on Inorganic Units. *Mol. Cryst. Liq. Cryst. Sci. Technol. Sect. A. Mol. Cryst. Liq. Cryst.* **1996**, *286* (1), 231–238.

(357) Ishihara, T. Optical Properties of PbI-Based Perovskite Structures. *J. Lumin.* **1994**, *61*.

(358) Cao, D. H.; Stoumpos, C. C.; Farha, O. K.; Hupp, J. T.; Kanatzidis, M. G. 2D Homologous Perovskites as Light-Absorbing Materials for Solar Cell Applications. *J. Am. Chem. Soc.* **2015**, *137* (24), 7843–7850.

(359) Yaffe, O.; Chernikov, A.; Norman, Z. M.; Zhong, Y.; Velauthapillai, A.; van der Zande, A.; Owen, J. S.; Heinz, T. F. Excitons in Ultrathin Organic-Inorganic Perovskite Crystals. *Phys. Rev. B* **2015**, *92* (4), 045414.

(360) Huang, X.; Li, J.; Fu, H. The First Covalent Organic−Inorganic Networks of Hybrid Chalcogenides: Structures That May Lead to a New Type of Quantum Wells. *Journal of the American Chemical Society*. September 2000, pp 8789–8790.

(361) Huang, X.; Le, V.; Li, J. Inorganic−Organic Hybrid Composites Containing MQ (II−VI) Slabs: A New Class of Nanostructures with Strong Quantum Confinement and Periodic Arrangement. *Chemistry of Materials*. October 2001, pp 3754–3759.

(362) Huang, X.; Li, J.; Zhang, Y.; Mascarenhas, A. From 1D Chain to 3D Network: Tuning Hybrid II-VI Nanostructures and Their Optical Properties. *J. Am. Chem. Soc.* **2003**, *125* (23), 7049–7055.

(363) Huang, X.; Li, J. From Single to Multiple Atomic Layers: A Unique Approach to the Systematic Tuning of Structures and Properties of Inorganic-Organic Hybrid Nanostructured Semiconductors. *J. Am. Chem. Soc.* **2007**, *129* (11), 3157–3162.

(364) Niu, W.; Eiden, A.; Vijaya Prakash, G.; Baumberg, J. J. Exfoliation of Self-Assembled 2D Organic-Inorganic Perovskite Semiconductors. *Appl. Phys. Lett.* **2014**, *104*, 171111.

(365) Dou, L.; Wong, A. B.; Yu, Y. Y.; Lai, M.; Kornienko, N.; Eaton, S. W.; Fu, A.; Bischak, C. G.; Ma, J.; Ding, T.; et al. Atomically Thin Two-Dimensional Organic-Inorganic Hybrid Perovskites. *Science (80-.).* **2015**, *349* (6255), 1518–1521.

(366) Bai, S.; Yuan, Z.; Gao, F. Colloidal Metal Halide Perovskite Nanocrystals: Synthesis, Characterization, and Applications. *J. Mater. Chem. C* **2016**.

(367) Schmidt, L. C.; Pertegás, A.; González-Carrero, S.; Malinkiewicz, O.; Agouram, S.; Mínguez Espallargas, G.; Bolink, H. J.; Galian, R. E.; Pérez-Prieto, J. Nontemplate Synthesis of CH3NH3PbBr3 Perovskite Nanoparticles. *J. Am. Chem. Soc.* **2014**, *136* (3), 850–853.

(368) Tyagi, P.; Arveson, S. M.; Tisdale, W. A. Colloidal Organohalide Perovskite Nanoplatelets Exhibiting Quantum Confinement. *J. Phys. Chem. Lett.* **2015**, *6* (10), 1911–1916.

(369) Sichert, J. A.; Tong, Y.; Mutz, N.; Vollmer, M.; Fischer, S.; Milowska, K. Z.; García Cortadella, R.; Nickel, B.; Cardenas-Daw, C.; Stolarczyk, J. K.; et al. Quantum Size Effect in Organometal Halide Perovskite Nanoplatelets. *Nano Lett.* **2015**, *15* (10), 6521–6527.

(370) Hassan, Y.; Song, Y.; Pensack, R. D.; Abdelrahman, A. I.; Kobayashi, Y.; Winnik, M. A.; Scholes, G. D. Structure-Tuned Lead Halide Perovskite Nanocrystals. *Adv. Mater.* **2016**, *28* (3), 566–573.

(371) Bekenstein, Y.; Koscher, B. A.; Eaton, S. W.; Yang, P.; Alivisatos, A. P. Highly Luminescent Colloidal Nanoplates of Perovskite Cesium Lead Halide and Their Oriented Assemblies. *J. Am. Chem. Soc.* **2015**, *137* (51), 16008–16011.

(372) Akkerman, Q. A.; Motti, S. G.; Srimath Kandada, A. R.; Mosconi, E.; D'Innocenzo, V.; Bertoni, G.; Marras, S.; Kamino, B. A.; Miranda, L.; De Angelis, F.; et al. Colloidal Cesium Lead Halide Perovskite Nanoplatelets with Monolayer-Level Thickness Control by a Solution Synthesis Approach. *J. Am. Chem. Soc.* **2016**, jacs.5b12124.

(373) Ling, Y.; Yuan, Z.; Tian, Y.; Wang, X.; Wang, J. C.; Xin, Y.; Hanson, K.; Ma, B.; Gao, H. Bright Light-Emitting Diodes Based on Organometal Halide Perovskite Nanoplatelets. *Adv. Mater.* **2016**, *28* (2), 305–311.

(374) Sharma, V.; Park, K.; Srinivasarao, M. Shape Separation of Gold Nanorods Using Centrifugation. *Proc. Natl. Acad. Sci.* **2009**, *106* (13), 4981–4985.

(375) Svedberg, T.; Pedersen, K. O.; Bauer, J. H. *The Ultracentrifuge*; International series of monographs on physics; The Clarendon Press, 1940.

(376) Murray, C. B.; Norris, D. J.; Bawendi, M. G. Synthesis and Characterization of Nearly Monodisperse CdE (E = Sulfur, Selenium, Tellurium) Semiconductor Nanocrystallites. *J. Am. Chem. Soc.* **1993**, *115* (19), 8706–8715.

(377) Liu, F.-K.; Ko, F.-H.; Huang, P.-W.; Wu, C.-H.; Chu, T.-C. Studying the Size/shape Separation and Optical Properties of Silver Nanoparticles by Capillary Electrophoresis. *J. Chromatogr. A* **2005**, *1062* (1), 139–145.

(378) Wei, G.; Liu, F.; Wang, C. R. C. Shape Separation of Nanometer Gold Particles by Size-Exclusion Chromatography. *Anal. Chem.* **1999**, *71* (11), 2085–2091.

(379) Park, K.; Koerner, H.; Vaia, R. A. Depletion-Induced Shape and Size Selection of Gold Nanoparticles. *Nano Lett.* **2010**, *10* (4), 1433–1439.

(380) Tang, J.; Kemp, K. W.; Hoogland, S.; Jeong, K. S.; Liu, H.; Levina, L.; Furukawa, M.; Wang, X.; Debnath, R.; Cha, D.; et al. Colloidal-Quantum-Dot Photovoltaics Using Atomic-Ligand Passivation. *Nature Materials*. Nature Publishing Group 2011, pp 765–771.

(381) Lhuillier, E.; Keuleyan, S.; Zolotavin, P.; Guyot-Sionnest, P. Mid-Infrared HgTe/As 2 S 3 Field Effect Transistors and Photodetectors. *Adv. Mater.* **2013**, *25* (1), 137–141.

(382) Yang, J.; Wise, F. W. Electronic States of Lead-Salt Nanosheets. *J. Phys. Chem. C* **2015**, acs.jpcc.5b08207.

(383) Benchamekh, R.; Gippius, N. A.; Even, J.; Nestoklon, M. O.; Jancu, J. M.; Ithurria, S.; Dubertret, B.; Efros, A. L.; Voisin, P. Tight-Binding Calculations of Image-Charge Effects in Colloidal Nanoscale Platelets of CdSe. *Phys. Rev. B* **2014**, *89* (3), 035307.

(384) Achtstein, A. W.; Schliwa, A.; Prudnikau, A.; Hardzei, M.; Artemyev, M. V.; Thomsen, C.; Woggon, U. Electronic Structure and Exciton-Phonon Interaction in Two-Dimensional Colloidal Cdse Nanosheets. *Nano Lett.* **2012**, *12* (6), 3151–3157.

(385) Shirasaki, Y.; Supran, G. J.; Bawendi, M. G.; Bulović, V. Emergence of Colloidal Quantum-Dot Light-Emitting Technologies. *Nat. Photonics* **2013**, *7* (12), 933–933.

(386) Guzelturk, B.; Kelestemur, Y.; Olutas, M.; Delikanli, S.; Demir, H. V. Amplified Spontaneous Emission and Lasing in Colloidal Nanoplatelets. *ACS Nano* **2014**, *8* (7), 6599–6605.

(387) Schaller, R. D.; She, C.; Fedin, I.; Dolzhnikov, D. S.; Demortière, A.; Schaller, R. D.; Pelton, M.; Talapin, D. V. Low-Threshold Stimulated Emission Using Colloidal Quantum Wells. *Nano Lett.* **2014**, *14* (5), 2772–2777.

(388) Li, M.; Zhi, M.; Zhu, H.; Wu, W.-Y.; Xu, Q.-H.; Jhon, M. H.; Chan, Y. Ultralow-Threshold Multiphoton-Pumped Lasing from Colloidal Nanoplatelets in Solution. *Nat. Commun.* **2015**, *6*.

(389) Klimov, V. I. V.; Mikhailovsky, A.; Xu, S.; Malko, A.; Hollingsworth, J.; Leatherdale, C. A.; Eisler, H.; Bawendi, M. G. Optical Gain and Stimulated Emission in Nanocrystal Quantum Dots. *Science (80-.).* **2000**, *290* (5490), 314–317.

(390) Konstantatos, G.; Sargent, E. H. *Colloidal Quantum Dot Optoelectronics and Photovoltaics*; Cambridge University Press, 2013.

(391) She, C.; Fedin, I.; Dolzhnikov, D. S.; Dahlberg, P. D.; Engel, G. S.; Schaller, R. D.; Talapin, D. V. Red , Yellow , Green , and Blue Ampli Fi Ed Spontaneous Emission and Lasing Using Colloidal CdSe Nanoplatelets. **2015**, No. Xx, 9475–9485.

(392) Lhuillier, E.; Robin, A.; Ithurria, S.; Aubin, H.; Dubertret, B. Electrolyte-Gated Colloidal Nanoplatelets-Based Phototransistor and Its Use for Bicolor Detection. *Nano Lett.* **2014**, *14* (5), 2715–2719.

(393) Lhuillier, E.; Ithurria, S.; Descamps-Mandine, A.; Douillard, T.; Castaing, R.; Xu, X. Z.; Taberna, P.-L.; Simon, P.; Aubin, H.; Dubertret, B. Investigating the N- and P-Type Electrolytic Charging of Colloidal Nanoplatelets. *J. Phys. Chem. C* **2015**, *119* (38), 21795–21799.

(394) Kovalenko, M. V.; Kaufmann, E.; Pachinger, D.; Roither, J.; Huber, M.; Stangl, J.; Hesser, G.; Schäffler, F.; Heiss, W. Colloidal HgTe Nanocrystals with Widely Tunable Narrow Band Gap Energies: From Telecommunications to Molecular Vibrations. *J. Am. Chem. Soc.* **2006**, *128* (11), 3516–3517.

(395) Keuleyan, S.; Lhuillier, E.; Brajuskovic, V.; Guyot-Sionnest, P. Mid-Infrared HgTe Colloidal Quantum Dot Photodetectors. *Nat. Photonics* **2011**, *5* (8), 489–493.

(396) Lhuillier, E.; Keuleyan, S.; Rekemeyer, P.; Guyot-Sionnest, P. Thermal Properties of Mid-Infrared Colloidal Quantum Dot Detectors. *J. Appl. Phys.* **2011**, *110* (3), 33110.

(397) Lhuillier, E.; Keuleyan, S.; Liu, H.; Guyot-Sionnest, P. Mid-IR Colloidal Nanocrystals. *Chem. Mater.* **2013**, *25* (8), 1272–1282.

(398) Lhuillier, E.; Scarafagio, M.; Hease, P.; Nadal, B.; Aubin, H.; Xu, X.; Lequeux, N.; Patriarche, G.; Ithurria, S.; Dubertret, B. Infrared Photo-Detection Based on Colloidal

Quantum-Dot Films with High Mobility and Optical Absorption up to the THz. *Nano Lett.* **2016**, acs.nanolett.5b04616.

(399) Mentzel, T. S.; Wanger, D. D.; Ray, N.; Walker, B. J.; Strasfeld, D.; Bawendi, M. G.; Kastner, M. a. Nanopatterned Electrically Conductive Films of Semiconductor Nanocrystals. **2012**, 4404–4408.

(400) Wang, H.; Lhuillier, E.; Yu, Q.; Mottaghizadeh, a.; Ulysse, C.; Zimmers, a.; Descamps-Mandine, a.; Dubertret, B.; Aubin, H. Effects of Electron-Phonon Interactions on the Electron Tunneling Spectrum of PbS Quantum Dots. *Phys. Rev. B* **2015**, *92* (4), 041403.

(401) Dorn, A.; Huang, H.; Bawendi, M. G. Electroluminescence from Nanocrystals in an Electromigrated Gap Composed of Two Different Metals. *Nano Lett.* **2008**, *8*, 1347–1351.

(402) Xing, W.; Kung, S. C.; Van Der Veer, W. E.; Yan, W.; Ayvazian, T.; Kim, J. Y.; Penner, R. M. High-Throughput Fabrication of Photoconductors with High Detectivity, Photosensitivity, and Bandwidth. *ACS Nano* **2012**, *6* (6), 5627–5634.

(403) Dayen, J.-F.; Faramarzi, V.; Pauly, M.; Kemp, N. T.; Barbero, M.; Pichon, B. P.; Majjad, H.; Begin-Colin, S.; Doudin, B. Nanotrench for Nano and Microparticle Electrical Interconnects. *Nanotechnology* **2010**, *21* (33), 335303.

(404) Prins, F.; Buscema, M.; Seldenthuis, J. S.; Etaki, S.; Buchs, G.; Barkelid, M.; Zwiller, V.; Gao, Y.; Houtepen, A. J.; Siebbeles, L. D. a; et al. Fast and Efficient Photodetection in Nanoscale Quantum-Dot Junctions. *Nano Lett.* **2012**, *12*, 5740–5743.

(405) Willis, L. J.; Fairfield, J. a; Dadosh, T.; Fischbein, M. D.; Drndic, M. Controlling Nanogap Quantum Dot Photoconductivity through Optoelectronic Trap Manipulation. *Nano Lett.* **2009**, *9* (12), 4191–4197.

(406) Buscema, M.; Island, J. O.; Groenendijk, D. J.; Blanter, S. I.; Steele, G. A.; van der Zant, H. S.; Castellanos-Gomez, A. Photocurrent Generation with Two-Dimensional van Der Waals Semiconductors. *Chem Soc Rev* **2015**, *44* (11), 3691–3718.

(407) Konstantatos, G.; Badioli, M.; Gaudreau, L.; Osmond, J.; Bernechea, M.; de Arquer, F. P. G.; Gatti, F.; Koppens, F. H. L. Hybrid Graphene-Quantum Dot Phototransistors with Ultrahigh Gain. *Nat. Nanotechnol.* **2012**, *7* (6), 363–368.

(408) Sun, Z.; Liu, Z.; Li, J.; Tai, G.; Lau, S.-P.; Yan, F. Infrared Photodetectors Based on CVD-Grown Graphene and PbS Quantum Dots with Ultrahigh Responsivity. *Adv. Mater.* **2012**, *24* (43), 5878–5883.

(409) Robin, A.; Lhuillier, E.; Xu, X. Z.; Ithurria, S.; Aubin, H.; Ouerghi, A.; Dubertret, B. Submitted. *Submitted*.

(410) Wiley, B. J.; Im, S. H.; Li, Z.-Y.; McLellan, J.; Siekkinen, A.; Xia, Y. Maneuvering the Surface Plasmon Resonance of Silver Nanostructures through Shape-Controlled Synthesis. *J. Phys. Chem. B* **2006**, *110* (32), 15666–15675.

(411) Sosa, I. O.; Noguez, C.; Barrera, R. G. Optical Properties of Metal Nanoparticles with Arbitrary Shapes. *J. Phys. Chem. B* **2003**, *107* (26), 6269–6275.

(412) Jiang, X.; Liu, R.; Tang, P.; Li, W.; Zhong, H.; Zhou, Z.; Zhou, J. Controllably Tuning the near-Infrared Plasmonic Modes of Gold Nanoplates for Enhanced Optical Coherence

Imaging and Photothermal Therapy. *RSC Adv.* **2015**, *5* (98), 80709–80718.

(413) Hao, E.; Schatz, G. C.; Hupp, J. T. Synthesis and Optical Properties of Anisotropic Metal Nanoparticles. *J. Fluoresc.* **2004**, *14* (4), 331–341.

(414) Andoy, N. M.; Zhou, X.; Choudhary, E.; Shen, H.; Liu, G.; Chen, P. Single-Molecule Catalysis Mapping Quantifies Site-Specific Activity and Uncovers Radial Activity Gradient on Single 2D Nanocrystals. *J. Am. Chem. Soc.* **2013**, *135* (5), 1845–1852.

(415) Lim, S. J.; McDougle, D. R.; Zahid, M. U.; Ma, L.; Das, A.; Smith, A. M. Lipoprotein Nanoplatelets: Brightly Fluorescent, Zwitterionic Probes with Rapid Cellular Entry. *J. Am. Chem. Soc.* **2016**, *138* (1), 64–67.